



**HAL**  
open science

# Measurement of local magnetic properties of devices with transmission electron microscopy

Xiaoxiao Fu

► **To cite this version:**

Xiaoxiao Fu. Measurement of local magnetic properties of devices with transmission electron microscopy. Materials Science [cond-mat.mtrl-sci]. Université Paul Sabatier - Toulouse III, 2016. English. NNT: 2016TOU30061 . tel-01532253

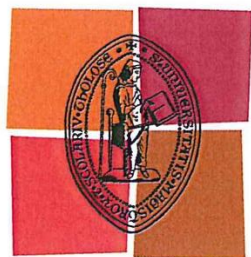
**HAL Id: tel-01532253**

**<https://theses.hal.science/tel-01532253>**

Submitted on 2 Jun 2017

**HAL** is a multi-disciplinary open access archive for the deposit and dissemination of scientific research documents, whether they are published or not. The documents may come from teaching and research institutions in France or abroad, or from public or private research centers.

L'archive ouverte pluridisciplinaire **HAL**, est destinée au dépôt et à la diffusion de documents scientifiques de niveau recherche, publiés ou non, émanant des établissements d'enseignement et de recherche français ou étrangers, des laboratoires publics ou privés.



Université  
de Toulouse

# THÈSE

En vue de l'obtention du  
**DOCTORAT DE L'UNIVERSITÉ DE TOULOUSE**

**Délivré par :**  
Université Toulouse III Paul Sabatier (UT3 Paul Sabatier)

**Discipline ou spécialité :**  
Physique de la Matière

---

**Présentée et soutenue par :**  
Xiaoxiao Fu

**le :** vendredi 27 mai 2016

**Titre :**

Mesure de Propriétés Magnétiques Locales de Dispositifs par Microscopie  
Electronique à Transmission

---

**Ecole doctorale :**  
Sciences de la Matière (SDM)

**Unité de recherche :**  
CEMES-CNRS

**Directeur(s) de Thèse :**  
Virginie Serin, Bénédicte Warot-Fonrose

**Rapporteurs :**  
Peter Schattschneider  
Jean Juraszek

**Membre(s) du jury :**  
Peter Schattschneider  
Jean Juraszek  
Bertrand Raquet  
Salia Cherifi  
Virginie Serin  
Bénédicte Warot-Fonrose

# Measurement of Local Magnetic Properties of Devices by Transmission Electron Microscopy

Xiaoxiao Fu

Thesis Supervisors:  
Virginie Serin,  
Bénédicte Warot-Fonrose

## Acknowledgements

I am proud to say that undertaking this PhD has changed me a lot and made me a better person. During the past three years, I have read hundreds of papers, performed many experiments and met all kinds of people. At this moment, I have so many thanks to say.

First and foremost, I would like to thank my supervisors Virginie Serin and Bénédicte Warot-Fonrose. Before starting my PhD work, I dreamed to have a supervisor who is very nice and patient to me, and lead me to take a good first step toward my future scientific research career. The dream then came true. How lucky I am to be a student of Virginie and Bénédicte. They taught me hand by hand how to make better experiments, led me to think, patiently answered my questions, showed me how to organize the literature more efficiently, guided me to write a good paper, provided me chances to visit other labs, encouraged me to present myself in more academic activities, and even like families, helped me to solve tricky problems in my daily life. What I have learned from them is far more than how to be a good researcher, but also how to be a good person.

I really appreciate the help from Sebastien Joulie. He is the one who taught me how to use transmission electron microscope step by step from the beginning, and always solved the technical problems of the microscope. In the first year, around the microscope, I was like a child who knew little about the new world but was very curious. I could not remember how many times I have asked him “Sebastien, why it is like this?” “Sebastien, how to do that?” With his help, I started my happy journey of microscopy.

Thanks Christophe Gatel for the holography experiment and fruitful discussion with me about the results. Each talk with him inspired me, making me better understand how to do research. Thanks Robin Cours to teach me how to prepare the specimen for transmission electron microscopy. Thanks Dominique Demaille and Mahmoud Eddrief to provide me samples of high quality. Thanks Rémi Arras for the density functional theory calculations.

I also want to thank my family especially my husband Dr. Lefeng Shi. They are thousands miles away in China, while I can feel they are with me all the time. If without their support and encouragement, I am not sure I have had finish my thesis at this moment. At last, I will never forget the happy days in the three years spent with my dear Chinese friends in France!

## Abstract

EMCD (Energy-Loss Magnetic Chiral Dichroism) is an emerging technique based on energy-loss spectroscopy (EELS) in a transmission electron microscopy (TEM). It aims at measuring the element-specific local magnetic moment of solids at a nanometer scale, and hence improving our understanding of magnetic local magnetic phenomena. This thesis presents the exploring work on developing the EMCD technique and its applications.

We have applied EMCD to epitaxial MnAs thin films grown on a GaAs(001) substrate, extending the application of this technique to hexagonal structure with high magnetocrystalline anisotropy. The 3d orbital-to-spin moment ratio of Mn in hexagonal ferromagnetic MnAs along easy, hard and intermediate magnetic axes has been respectively estimated and then compared to DFT calculations. Moreover, a breaking of the ferromagnetic order in MnAs thin film, together with the crystallographic transition from hexagonal  $\alpha$ -MnAs to quasi-hexagonal  $\beta$ -MnAs, has been locally studied *in-situ* by modifying the temperature of the crystal inside the electron microscope.

EMCD has also been settled to probe 4f moment in rare earth compounds, by investigating Dy- $M_{4,5}$  edges in DyFe<sub>2</sub>/YFe<sub>2</sub> superlattices. We have derived sum rules which are specified for 4f moment and applied them to the obtained dichroic signal over Dy- $M_{4,5}$  edges. In addition, antiparallel coupling of Dy and Fe moments has been confirmed by comparing their dichroic signals, taking into account the dynamic diffraction effect.

The work in this thesis illustrates for the first time the feasibility of EMCD technique for quantitative study of magnetocrystalline anisotropy and magnetic transition, and also proves its potential as a tool to investigate 4f moment as well as moment coupling in magnetic materials.

## Résumé

L'EMCD, Energy Loss Magnetic Chiral Dichroism, est une technique récente, mise en œuvre dans le microscope électronique à transmission (TEM), qui utilise la spectroscopie de pertes d'énergie d'électrons (EELS). Elle a pour objectif la mesure du moment magnétique local d'un élément chimique donné. Son utilisation contribue à progresser dans la compréhension des phénomènes magnétiques à l'échelle nanométrique. Cette thèse propose d'élargir les domaines d'applications de l'EMCD.

Nous avons exploité l'EMCD pour l'étude de films minces de MnAs épitaxiés sur un substrat de GaAs(001). Ce travail montre l'utilité de cette technique dans le cas de structures hexagonales présentant une anisotropie magnéto-cristalline élevée. Le rapport des moments orbital et de spin du Mn dans les films de MnAs ferromagnétique de structure hexagonale a été mesuré par EMCD et comparé à des calculs DFT, ceci le long des axes magnétiques facile, difficile et intermédiaire. Une rupture de l'ordre ferromagnétique a par ailleurs été observée et mesurée *in situ* dans le microscope grâce à un porte-objet chauffant, lors de la transition cristallographique de  $\alpha$ -MnAs hexagonal à  $\beta$ -MnAs quasi-hexagonal.

La technique EMCD a également été mise en œuvre pour sonder le moment 4f de composés de terres rares à base de dysprosium. Il s'agissait d'étudier des super-réseaux DyFe<sub>2</sub>/YFe<sub>2</sub>. Les règles de somme ont été établies pour le seuil  $M_{4,5}$  du Dy. En outre, le couplage antiparallèle des moments Dy et Fe a été confirmé en comparant leurs signaux dichroïques et en prenant en compte la théorie dynamique de la diffraction.

Ce travail de thèse illustre pour la première fois d'une part la faisabilité de la technique EMCD pour l'étude quantitative de l'anisotropie et des transitions magnétiques, et d'autre part son potentiel pour étudier les terres rares et leur moment 4f, ainsi que le couplage avec des éléments de transition.



# Table of Contents

<b>INTRODUCTION .....</b>	<b>1</b>
<b>CHAPTER I. ENERGY-LOSS MAGNETIC CHIRAL DICHOISM.....</b>	<b>5</b>
<b>1. ELECTRON ENERGY-LOSS SPECTROSCOPY .....</b>	<b>5</b>
<b>1.1 Interaction of electrons with matter .....</b>	<b>6</b>
1.1.1 Classification of electron scattering .....	6
1.1.2 Physics of electron scattering .....	8
<b>1.2 Electron energy-loss spectrum .....</b>	<b>11</b>
1.2.1 General form of EELS spectrum .....	11
1.2.2 Ionization edges .....	12
<b>1.3 Chirality in EELS .....</b>	<b>14</b>
<b>2. EMCD TECHNIQUE .....</b>	<b>18</b>
<b>2.1 From XMCD to EMCD .....</b>	<b>18</b>
<b>2.2. EMCD sum rules .....</b>	<b>21</b>
<b>2.3 Experimental setup .....</b>	<b>22</b>
2.3.1 Detection of EELS spectrum .....	22
2.3.2 EMCD experimental methods .....	24
<b>2.4 EMCD: summary of literature outcome .....</b>	<b>28</b>
<b>BIBLIOGRAPHY .....</b>	<b>31</b>
<b>CHAPTER II. EPITAXIAL MNAS THIN FILMS ON GAAS SUBSTRATE.....</b>	<b>35</b>
<b>1. CRYSTALLOGRAPHIC STRUCTURE.....</b>	<b>35</b>
<b>2. MICROMAGNETIC STRUCTURE .....</b>	<b>38</b>
2.1 Domain structure observed with various techniques.....	39
2.2 Temperature-dependent domain structure .....	41
2.3 Thickness-dependent domain structure .....	43
<b>3. MAGNETIC ANISOTROPY .....</b>	<b>45</b>
3.1 In plane and out-of-plane anisotropy .....	46
3.2 Temperature-dependent magnetization .....	47
3.3 Thickness-dependent magnetization .....	48
<b>BIBLIOGRAPHY .....</b>	<b>50</b>
<b>CHAPTER III. DYFE<sub>2</sub>/YFE<sub>2</sub> LAVES PHASE SUPERLATTICES .....</b>	<b>53</b>
<b>1. CRYSTALLOGRAPHIC STRUCTURE .....</b>	<b>54</b>
<b>2. MAGNETIC PROPERTIES .....</b>	<b>56</b>

<b>2.1 The exchange coupling in DyFe<sub>2</sub>/YFe<sub>2</sub> system</b> .....	56
<b>2.2 Magnetic exchange springs and associated phenomena</b> .....	58
2.2.1 Three different reversal processes .....	58
2.2.2 Irreversible magnetic exchange-spring processes .....	61
2.2.3 Exchange bias and other phenomena.....	62
<b>BIBLIOGRAPHY</b> .....	65

## **CHAPTER IV. EXPERIMENTAL RESULTS OF MNAS/GAAS(001) EPITAXIAL LAYERS..... 69**

<b>1. SAMPLE PREPARATION</b> .....	69
<b>2. STRUCTURAL CHARACTERIZATION AT ROOM TEMPERATURE</b> .....	70
<b>2.1 X-ray diffraction (XRD)</b> .....	70
<b>2.2 Magnetic force microscopy (MFM)</b> .....	71
<b>2.3 Transmission electron microscopy (TEM)</b> .....	74
2.3.1 TEM imaging.....	74
2.3.2 Electron diffraction.....	76
<b>3. EMCD STUDY OF MAGNETOCRYSTALLINE ANISOTROPY OF A-MNAS</b> .....	84
<b>3.1 EMCD signal of <math>\alpha</math>-MnAs at RT</b> .....	84
3.1.1 Acquisition of EMCD signal .....	84
3.1.2 Application of EMCD sum rule.....	87
<b>3.2 Anisotropic EMCD signal</b> .....	90
3.2.1 Acquisition of EMCD signal .....	90
3.2.2 Comparison of EMCD results with XMCD and theoretical results .....	92
<b>4. IN-SITU OBSERVATION OF PHASE TRANSITION</b> .....	93
<b>4.1 In-situ observation of crystallographic Transition</b> .....	93
<b>4.2 Temperature dependent EMCD</b> .....	94
<b>4.3 Temperature dependent holography</b> .....	96
<b>5. CONCLUSION</b> .....	100
<b>BIBLIOGRAPHY</b> .....	101

## **CHAPTER V. EXPERIMENTAL RESULTS OF EPITAXIAL DYFE<sub>2</sub>/YFE<sub>2</sub> SUPERLATTICES..... 103**

<b>1. SAMPLE PREPARATION</b> .....	104
<b>2. STRUCTURE AND COMPOSITION INFORMATION</b> .....	104
<b>2.1. Composition information</b> .....	104
<b>2.2. Crystallographic structure information</b> .....	107
<b>3. EMCD STUDY OF EPITAXIAL DYFE<sub>2</sub>/YFE<sub>2</sub> SUPERLATTICES</b> .....	111
<b>3.1 Acquisition of EMCD signals on L<sub>2,3</sub> and M<sub>4,5</sub> edges</b> .....	111
<b>3.2 EMCD Sum rules for M<sub>4,5</sub> edges</b> .....	113
3.2.1 General XMCD sum rules .....	114
3.2.2. Derivation of general EMCD sum rules from XMCD ones.....	115
3.2.3. Sum rules for M <sub>4,5</sub> edges of 4f rare earth and its application .....	118
<b>3.3 Coupling Behavior of Fe and Dy moments</b> .....	120
<b>4. CONCLUSION</b> .....	122



<b>BIBLIOGRAPHY .....</b>	<b>124</b>
<b>CONCLUSION .....</b>	<b>127</b>
<b>APPENDIX I. TRANSMISSION ELECTRON MICROSCOPY .....</b>	<b>131</b>
<b>APPENDIX II. TEM SPECIMEN PREPARATION.....</b>	<b>136</b>
<b>APPENDIX III. MOLECULAR BEAM EPITAXY .....</b>	<b>139</b>
<b>APPENDIX IV. DENSITY FUNCTIONAL THEORY .....</b>	<b>144</b>
<b>LIST OF PUBLICATIONS .....</b>	<b>146</b>
<b>CURRICULUM VITAE .....</b>	<b>147</b>

## **Introduction**

Magnetic devices are widely applied in the field of computer science, information technology, electric power technology, automation technology, etc. The fundamental research on the local magnetic properties of devices is of significant value, since it may provide a deep insight into the mechanism of the magnetic properties, thus help to improve or design new magnetic devices. To study the magnetic material in a magnetic device, in particular the spintronic device, an adapted technique is needed to identify the contribution of the magnetism from each element and to separate the contribution of the spin and orbital moments. Moreover in recent decades, magnetic devices, for instance the memory devices, have been increasingly miniaturized. The dimension of magnetic structures in those devices can be at the sub-nanoscale. It requires a measurement technique which is able to reach a high spatial resolution. Thanks to the delicate and powerful transmission electron microscope (TEM), energy-loss magnetic chiral dichroism (EMCD) can be such a technique which is capable to measure the element-specific local magnetic moment of solids at a sub-nanometer scale.

EMCD, a TEM technique based on the analysis of the ionized edges in electron energy-loss spectra (EELS), was firstly proposed in 2003 and experimentally verified in 2006. Since then, it has been constantly improved in both theory and experimental configuration, while more efforts must be taken to make it a routine method to measure the local magnetic properties. Until now, EMCD experiments have been largely performed on the materials which crystalize in the cubic structure, and generally investigate the  $L_{2,3}$  edges of 3d transition metal. In this thesis, I will present the application of EMCD to epitaxial MnAs thin films on GaAs substrate and epitaxial  $DyFe_2/YFe_2$  superlattices, and try to answer four main questions: (i) Can EMCD be applied to the crystal in a hexagonal structure with high magnetocrystalline anisotropy? (ii) Can we take EMCD one step towards a dynamic measurement method? (iii) Is EMCD effective to investigate the  $M_{4,5}$  edges of the rare earth element? (iv) Can we investigate the magnetic coupling of magnetic moments with EMCD?

In the first chapter of this thesis, I give an overview of the EMCD technique, including its principle, experimental setup as well as its application. Since EMCD is based on EELS and inspired by XMCD, a part of this chapter introduces the background knowledge of EELS and XMCD. Why the magnetic circular dichroism in XMCD can be analogue to the magnetic chiral dichroism in EMCD and how the chirality can be achieved in EELS will be explained. The latter part of this chapter is more like a literature review about the development of EMCD technique in the last ten years. A table at the end summarizes the important works in EMCD.

The second and the third chapters respectively contain key information about the epitaxial MnAs thin films on GaAs substrate and the epitaxial DyFe<sub>2</sub>/YFe<sub>2</sub> superlattices. Detailed information of their epitaxial growth, crystallographic structures and magnetic properties is all summarized, providing necessary background knowledge to understand the experimental results in this thesis. In chapter II, three things are worth noticing in particular. The first one is the interesting phase coexistence during phase transition in MnAs thin films. The second one is the temperature- and thickness-dependent magnetization and magnetic domains of MnAs films. Third, the ferromagnetic MnAs crystalizes in a hexagonal structure and it has both in-plane and out-of-plane magnetocrystalline anisotropy. In chapter III, the magnetic coupling behavior of Fe, Dy Y magnetic moments in DyFe<sub>2</sub>/YFe<sub>2</sub> superlattices is the focus. The form of an exchange spring is highlighted.

The fourth chapter presents the experimental results of MnAs/GaAs(001) epitaxial layers. After a brief introduction of the sample preparation in section 1, structural properties of the sample obtained with several techniques is described in section 2. How the hexagonal  $\alpha$ -MnAs and quasi-hexagonal  $\beta$ -MnAs are distinguished by electron diffraction in a TEM is illustrated and several groups of simulated atomic structures and diffraction patterns along some specific zone axes are demonstrated for better explanation. In the following, the EMCD study on the distinguished hexagonal  $\alpha$ -MnAs crystal along the easy, hard and intermediate magnetic axes at RT is illustrated in detail and then compared to the XMCD and theoretical results. We will see if the influence of magnetocrystalline anisotropy can be demonstrated by EMCD. Then after an in-situ observation of the phase transition from  $\alpha$ -MnAs to  $\beta$ -MnAs by EMCD technique is also shown. Lots of details on this rather original work of EMCD will be displayed. In addition,

an observation of the phase transition by an electron holography technique will be added in the last section, as complementary information to the EMCD results.

The last chapter shows the experimental results of DyFe<sub>2</sub>/YFe<sub>2</sub> superlattices. Similar to the previous chapter, a brief introduction of the sample preparation and the investigation of its crystallographic structure are at first presented. In particular, the structure factor of Dy and Fe atoms in a DyFe<sub>2</sub> crystal is calculated to determine a specific three-beam condition in the EMCD experiment. Here in this chapter, not only the EMCD signal of Fe-L<sub>2,3</sub> edges but also that of Dy-M<sub>4,5</sub> edges will be shown. EMCD sum rules for M<sub>4,5</sub> edges are specially derived and applied to Dy-M<sub>4,5</sub> edges. It is the first time that the 3d and 4f moments are probed at the same time in a TEM by investigating the L<sub>2,3</sub> edges of a transition metal element and the M<sub>4,5</sub> edges of a rare earth element in the same area of a rare earth compound. In addition, a comparison made between the EMCD signals of Dy and Fe suggests a coupling relationship of Dy and Fe moments, while we have to carefully take into account the dynamical effect.

Moreover, four appendixes are attached, offering additional information of the TEM, TEM specimen preparation, epitaxial growth methods and the density functional theory, followed by my list of publications and curriculum vitae in the end.



## Chapter I

### Energy-loss Magnetic Chiral Dichroism

---

In this chapter, I will introduce the principle, the experimental setup and the application of energy-loss magnetic chiral dichroism (EMCD) technique. Since EMCD is based on the electron energy loss spectroscopy (EELS), some background knowledge of EELS will necessarily be introduced at first, which must help in understanding the principle of EMCD.

#### 1. Electron energy-loss spectroscopy

Electron energy loss spectroscopy (EELS) is a technique whereby a beam of monoenergetic electrons interacts with a specimen and the energy distribution of scattered electrons is analyzed to give an electron energy loss spectrum<sup>1</sup>. If the incident electrons come to sample surface at a glancing angle, they can only go through small depth from the surface and then be scattered out, as sketched in Fig. 1.0(a). This is reflection electron energy loss spectroscopy (REELS)<sup>2</sup>, an efficient surface characterization technique. Differently, if the incident electrons arrive perpendicularly to the surface and go through the thin specimen (at most 100 nm thickness required for 100 kV electrons) as seen in Fig. 1.0(b), they will be scattered elastically or inelastically. The transmitted electrons into a spectrometer, especially the inelastically scattered ones, are believed to carry rich information from the bulk of samples. Transmission EELS is usually conducted in a transmission electron microscope (TEM), helping to reveal the chemistry, bonding and electronic structures of materials<sup>3</sup>. Correlatively, the beam of transmitted electrons in the TEM within specific energy loss can form an energy-filtered image or diffraction pattern, which is energy-filtered transmission electron microscopy (EFTEM) technique<sup>3</sup>.

In this section, we focus on transmission EELS, first briefly discussing the interaction of electrons with matter, next presenting basic components of EELS spectrum and finally explaining the chirality in EELS as a precondition of the energy-loss magnetic chiral dichroism (EMCD) technique.

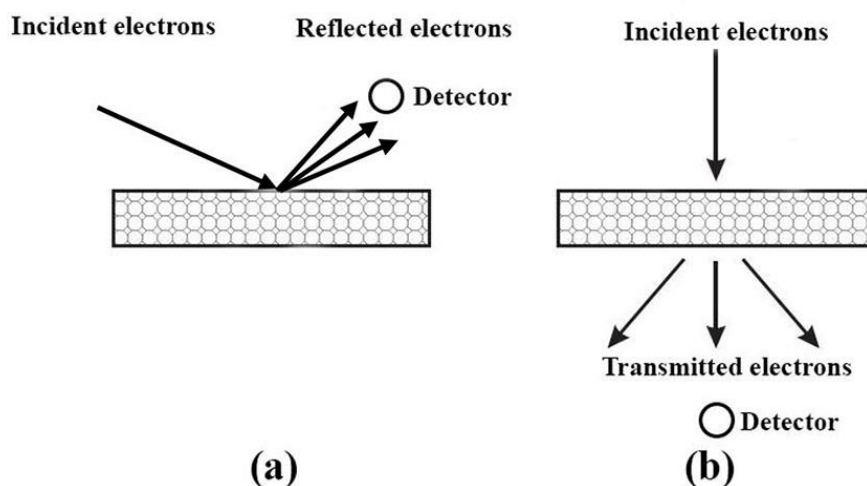


Fig. 1.0. Simplified beam path in (a) REELS and (b) Transmission EELS.

## 1.1 Interaction of electrons with matter

In EELS, a beam of fast electrons is used as the probe of atomic and electronic structures. When these fast electrons enter a solid, they interact with atoms in specimen through Coulomb forces and will be scattered. Consequently their direction and energy after interaction may both be altered. The scattering processes can be divided into elastic scattering which involves no energy change of incident electrons and inelastic scattering which involves an energy change.

### 1.1.1 Classification of electron scattering

Elastic scattering involves Coulomb interaction between incident electrons and atomic nuclei of the specimen. It can be of two types. One is large-angle elastic scattering, also known as Rutherford scattering. It happens when an incident electron approaches close enough to the nuclei. One exception should be mentioned that some large-angle scattering is not elastic but presents high energy transfer during collision, which may be enough to displace atoms from their original positions in crystalline lattice, resulting in displacement damage or atom sputtering from sample surface. The other scattering process is small-angle elastic scattering (typically 10-100 milliradians), when an incident electron approaches further to the nuclei. In crystalline solids, interference effect happens between electron waves scattered at small angles from regularly spaced atomic plane, so diffracted waves are formed in some specific directions given by Bragg's Law, thus

forming diffraction pattern. Usually Bragg spots in diffraction pattern is not sharp-edged but surrounded by a halo, as a consequence of inelastic scattering described below.

There are mainly four types of inelastic scattering mechanisms among many interaction processes with energy loss and transfer<sup>1</sup>:

(1) Incident electrons excite phonons that are atomic vibration in solid. The energy loss here is small ( $<0.1\text{eV}$ ), so it is immersed in unscattered electrons and hard to resolve. But the vibrational-loss spectrum actually contains rich information about the structures of sample, which has been observed with reflected low-energy electrons and high-resolution transmission spectroscopy.

(2) Incident electrons also excite plasmons (collective oscillation of valence electrons in a solid at characteristic angular frequency) by causing oscillations of potential and electron density inside the specimen. This resonant motion will keep up if there is no damping. In exciting plasmons, incident electrons transfer  $5\text{eV}$ - $30\text{eV}$  energy to the electron gas (valence electrons). In addition, there are also surface plasmons at each exterior surface.

(3) In single electron excitations, the incident electrons, through direct or indirect impact, transfer the energy to outer- or inner-shell atomic electrons of specimen, resulting in energy level transition of these atomic electrons. Fig. 1.1 presents the excitation process of a single electron, as well as the emission of photons and electrons due to de-excitation. For outer-shell electrons in an insulator or semiconductor, an electron may undergo an interband transition across the energy gap. Similarly in a metal, a conduction electron undergoes a transition to a higher state within the same energy band. If the excited electron has sufficient energy to leave the surface of the specimen, it is called secondary electron. Moreover, if an electron undergoes a downward transition to fill the “hole” left in outer-shell, a photon may be released. For deeply bound inner-shell electrons, a much greater amount of energy than outer-shell electrons is needed to make a transition. These ionized atoms will be de-ionized very soon, and liberate excess energy as electromagnetic radiation (X-ray) or kinetic energy of another atomic electron (Auger Emission).



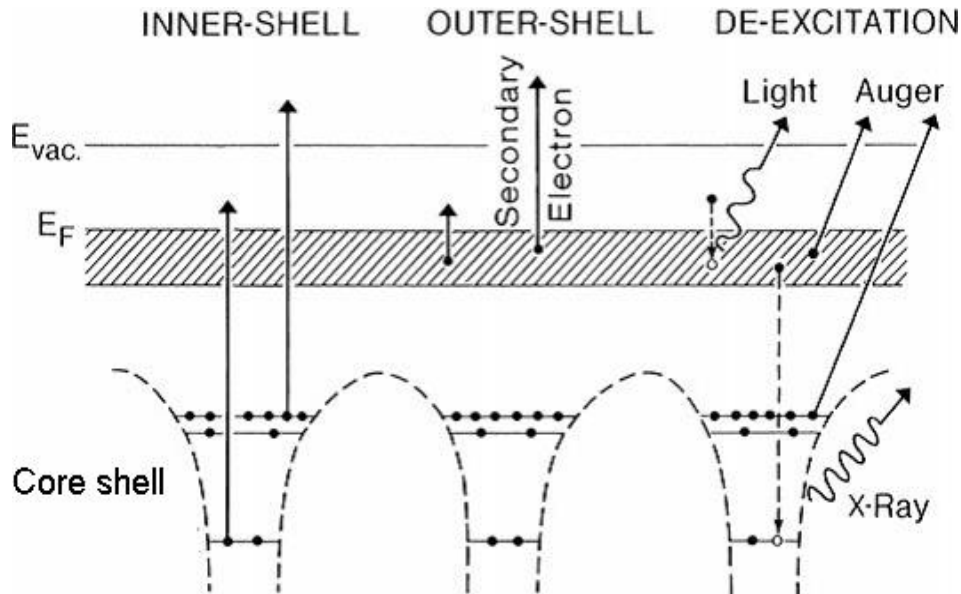


Fig. 1.1. Energy-level diagram of a solid, including core levels and a valence band of delocalized states (shaded);  $E_F$  is the Fermi level and  $E_{vac}$  the vacuum level. The primary processes of inner- and outer-shell excitation are shown on the left, secondary processes of photon and electron emission on the right<sup>1</sup>.

(4) Direct radiation loss also happens when the transmitted electron undergoes centripetal acceleration. This radiation, known as bremsstrahlung, carries energy within a wide range from zero to the incident electron's initial energy. Usually it contributes to the background of spectrum.

### 1.1.2 Physics of electron scattering

In addition to the intuitive description, the mathematic description is necessary to understand the electron scattering. A vector diagram is usually used to describe the elastic and inelastic scattering, as seen in Fig. 1.2.  $\mathbf{k}_i$  and  $\mathbf{k}_f$  are the wave vectors of the incident electron before and after being scattered and  $(\hbar/2\pi)\mathbf{q}$  represents the momentum transfer from the incident electron to the specimen, where the transfer scattering vector is  $\mathbf{q} = \mathbf{k}_i - \mathbf{k}_f$ . For elastic scattering  $|\mathbf{k}_i| = |\mathbf{k}_f|$ , no energy exchange happens. The momentum conservation law gives  $q = 2k \sin(\theta/2)$ , where  $q$  is the magnitude of  $\mathbf{q}$ ,  $k$  is the magnitude of  $\mathbf{k}$ , and  $\theta$  is the scattering angle. For inelastic scattering,

$q^2 = k_i^2(\theta^2 + \theta_E^2)$ .  $\theta_E$  is the characteristic angle corresponding to the average energy-loss

$E_{av}$ ,  $\theta_E = \frac{E_{av}}{\gamma m_0 v^2}$ , where  $\gamma = (1 - \frac{v^2}{c^2})^{-1/2}$ ,  $v$  and  $c$  are the incident electron velocity and light velocity,  $m_0$  is the electron rest mass.

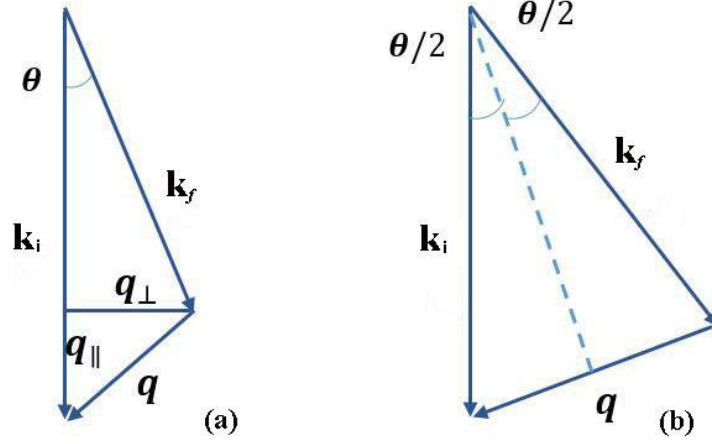


Fig. 1.2. Vector diagram<sup>1</sup> for (a) inelastic scattering and (b) elastic scattering.

After fast electrons enter the specimen, they may undergo single, plural, multiple scattering. The cross-section  $\sigma$  describes the probability of an incident electron to be scattered by a given atom in specimen<sup>4</sup>. The differential cross-section  $d\sigma/d\Omega$ , a quantity of basic importance in scattering theory, represents the cross-section per unit solid angle  $\Omega$ .

First, we discuss the differential cross-section of elastic scattering. According to the classical and wave-mechanical theory, it can be expressed as follow to estimate the large-angle elastic scattering<sup>1</sup>:

$$\frac{d\sigma}{d\Omega} = \frac{4\gamma^2 Z^2}{a_0^2 q^4} \quad (1.1)$$

here  $a_0 = 4\pi\epsilon_0\hbar^2/m_0e^2 = 0.529 \times 10^{-10} m$  is the Bohr radius and  $Z$  is the atom number.

But this formula will largely overestimate the small-angle elastic scattering, because the screening of nucleus field by atomic electrons is not taken into consideration. The formula incorporating screening can be expressed as angular distribution<sup>1</sup>:

$$\frac{d\sigma}{d\Omega} \approx \frac{4\gamma^2 Z^2}{a_0^2 k_i^4} \frac{1}{(\theta^2 + \theta_0^2)^2} \quad (1.2)$$

where  $\theta_0 = (k_i r_0)^{-1}$  is the characteristic angle of elastic scattering and  $r_0 = a_0 Z^{-1/3}$  is a screening radius. But what is described above is just based single atoms. Actually in a molecule, the cross-section at small angle per atom would be less because of the chemical bonding. In addition, in crystalline solid the angular distribution is dramatically changed by diffraction effect compared with amorphous solid. A structure factor  $F(\theta)$  is introduced to describe the elastic scattering in crystalline solid:

$$F(\theta) = \sum_j f_j(\theta) \exp(-i\mathbf{q} \cdot \mathbf{r}_j)$$

where  $r_j$  and  $f_j$  are respectively the coordinate and scattering amplitude of atom  $j$ . The angular distribution of intensity relative to incident beam is  $|F(\theta)|^2$  and peaks appear at the Bragg angle  $\theta_B$  which is defined from  $\lambda = 2d \sin \theta_B$ .

For the mathematic description of the inelastic scattering, it is more convenient to introduce double differential cross-section (DDSCS)  $\frac{d^2\sigma}{d\Omega dE}$ . This quantity is proportional to the number of incident electrons scattered within an energy range  $\Delta E$  and momentum variation into a solid angle  $\Delta\Omega$ . Quantum mechanics has been used to derivate the form of DDSCS.

We use the plane wave states in form of  $\exp(i\mathbf{k} \cdot \mathbf{r})$  to describe the incident electron, where  $\mathbf{k}$  can be  $\mathbf{k}_i$  and  $\mathbf{k}_f$  to represent the wave vector of incident electron before- and after-scattering respectively, and  $\mathbf{r}$  represent the coordinate. When an incident electron approaches an atomic electron within the specimen, the Coulombic interaction between them causes transition of atomic electron from initial state to final state. The initial one-electron state is represented by  $|\phi_i\rangle$  and the final one by  $|\phi_j\rangle$ . The transition rate between the two states can be described by Fermi's Golden Rule. Resulted from a set of mathematical derivation, the DDSCS is given in Eq. (1.3)<sup>5</sup>. Since only transitions to unoccupied states are allowed for a Fermionic system, there is an index  $j$  in the subset.

$$\frac{d^2\sigma}{d\Omega dE} = \frac{4\gamma^2}{a_0^2 q^4} \frac{k_f}{k_i} \sum_{j_{unoc}} |\langle \phi_i | \exp(i\mathbf{q} \cdot \mathbf{r}) | \phi_j \rangle|^2 \delta(E_i + E - E_j) \quad (1.3)$$

The DDSCS, now represented as a continuous function of energy-loss  $E$ , can be used to analyze the EELS spectrum which is a counted number of electrons as a function of energy loss.

## 1.2 Electron energy-loss spectrum

After interaction with a specimen, the scattered electrons carrying the chemical or structural information of the specimen are detected to form an EELS spectrum. In this section, we demonstrate a general form of EELS spectrum and describe different ionized edges in detail.

### 1.2.1 General form of EELS spectrum

The transmitted electrons, after single or plural scattering, go directly into the spectrometer and are separated according to their remaining kinetic energy. Thus an energy loss spectrum, which is seen as the counts of detected electrons as a function of their energy loss, can be obtained. Fig. 1.3 shows an example of EELS spectrum observed in TEM-EELS system.

The sharp zero loss peak (ZLP) at 0 eV energy loss comes from all the elastic scattered and quasi-elastic scattered electrons. The half-width of the ZLP depends on the energy resolution of incident electrons. Usually it does not contain structure information of the specimen. But it is still useful for adjustment of spectrometer, or quantitative analysis of sample.

The smaller peak in low-loss region, extending from a few eV to about 50 eV, corresponds to the interaction of fast electron with atomic valence electron. In this region, energy loss for plasmons takes the most part. With the plasmon peak, we can measure the sample thickness and permittivity in particular, and indirectly detect the chemical compound composition. If the sample is not very thin, plural or multiple scattering may occur, thus adding multiple plasmon peaks to the low-loss region. Furthermore, there may be also obvious peaks from interband and intraband transitions of valence electrons.

The high-loss region, extending from 40-50 eV to thousands of eV, contains the core electron excitation. For the ionization of atoms, the ionization energy (ionization threshold) must be transferred from the incident electron to the inner-shell electron, leading to ionization edges at specific energy losses in the EELS spectrum. As seen in Fig. 1.3, ionization edges are superimposed on a downward sloping background in this region. This downward sloping background can arise from valence electron scattering and the other ionization edges, and also possibly arise from plural scattering for thicker specimens. The sharp rise occurring at specific energy loss would tell us which element

is contained within the specimen. In the figure, Ba-N<sub>4,5</sub> edges, Ba-M<sub>4,5</sub> edges, Y-M<sub>3</sub> edge, O-K edge and Cu-L<sub>3</sub> edge are presented. The definition of these notations K, L, M, and N will be described in the next section 1.2.2. Electron energy loss near edge structure (ELNES) which is usually within 50 eV of transition threshold and extended energy loss structure (EXELFS) which is 50-300eV away from transition threshold both contain rich information. The fine structure of the edges reflects crystallographic and electronic structure of the specimen. In particular, ELNES reflects the unoccupied density of states above the Fermi level.

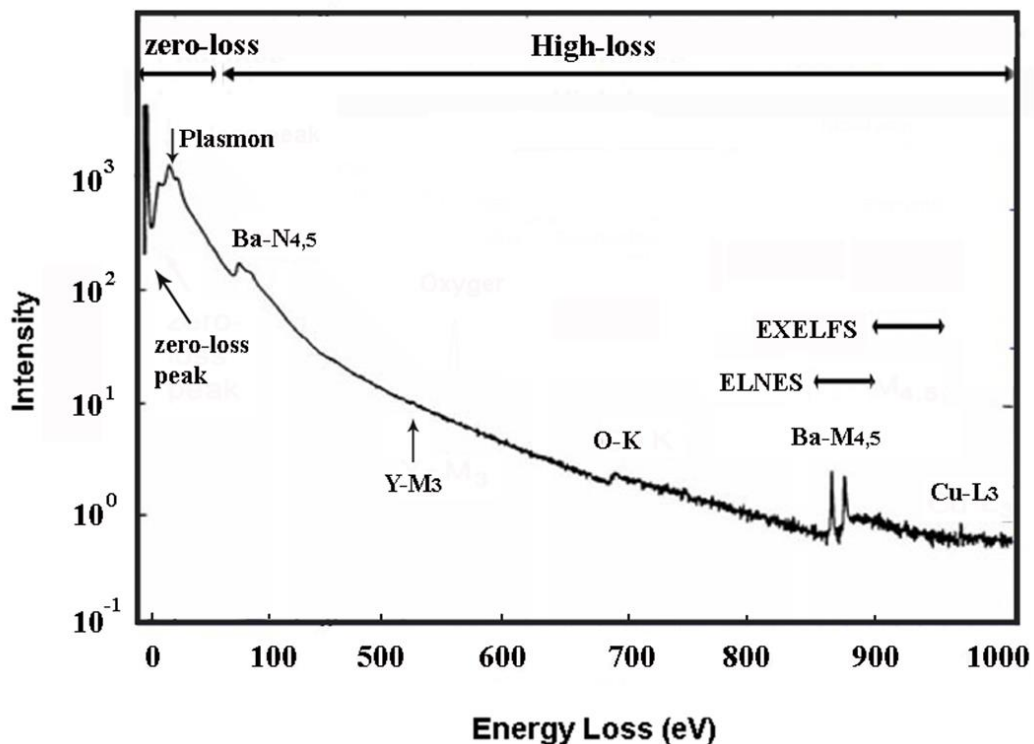


Fig 1.3. EELS spectrum<sup>1</sup> of a high-temperature superconductor (YBa<sub>2</sub>Cu<sub>3</sub>O<sub>7</sub>) with the electron intensity on a logarithmic scale, showing zero-loss peak, plasmon peaks and ionized edges arising from Y, O, Ba and Cu elements.

### 1.2.2 Ionization edges

In the previous section it is mentioned that the excitation of an electron from a core level into the valence band leads to an ionization edge in the spectrum. Different notations are used to indicate different edges. Generally a notation contains a letter K, L, M or N and one or more numbers as the subscript, as illustrated in Fig. 1.3. The letter represents the core shell that is excited. K means the transition is from first shell; L means the

transition is from second shell, and so on. The numbers in the subscript indicate which orbital in the core shell is excited. 1 corresponds to s state; 2 corresponds to p state; 3 corresponds to d state, and so on. For instance,  $L_1$  indicates a transition from the s orbital in the L shell. A sketch of electron shells and sub-shells is displayed in Fig. 1.4.

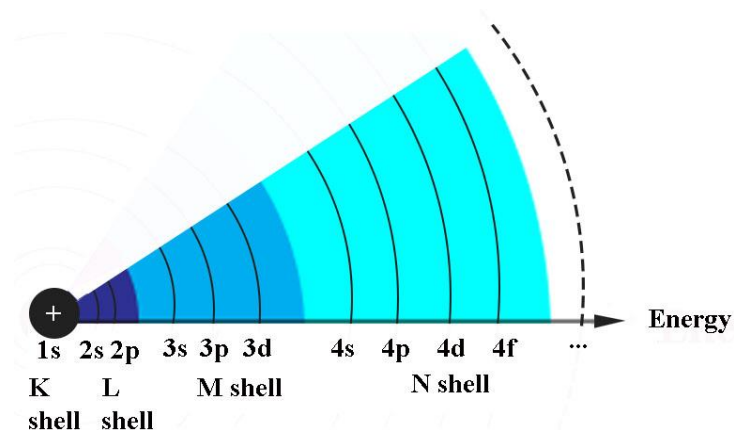


Fig. 1.4. A sketch of electron shells and sub-shells in an atom.

However, when the core level presents an energy split due to spin-orbit coupling, more than one peak which are separated in energy will appear in the corresponding ionization edges, resulting in more than one number in the subscript.  $L_{2,3}$  edges of Fe ion is taken as an example in Fig. 1.5. Fe is a transition metal with unfilled d states. In the L shell, the spin-orbit coupling in the 2p state splits this state into  $Fe2p_{3/2}$  and  $Fe2p_{1/2}$ . So two peaks are observed:  $L_3$  edge corresponds to  $Fe2p_{3/2} \rightarrow Fe3d$  transitions, while  $L_2$  edge corresponds to  $Fe2p_{1/2} \rightarrow Fe3d$ . Similarly, the split in the 3d state also results in separated peaks and two numbers in the subscript as  $M_{4,5}$ . The K edge, which shows only one peak, is an exception. It is because the spin-orbit interaction in 1s state is unavailable. The table 1.1 lists some important edges. Actually the ionization edges are directly related to both the spin-orbit coupling in core levels and the unoccupied density of valence states, making them very useful to extract electric structure information and further the magnetic information.

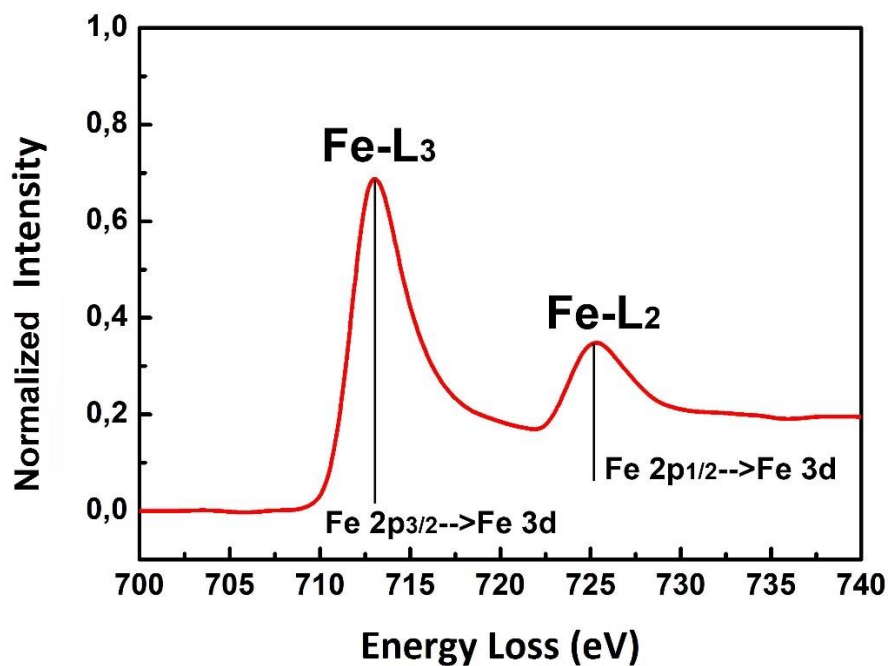


Fig. 1.5. Fe-L<sub>2,3</sub> edges in EELS spectrum.

Table 1.1. Some transitions from core levels and their corresponding notations of ionization edges.

1s → p or d	K
2p → 3d	L <sub>2,3</sub>
3d → 4f	M <sub>4,5</sub>
4d → 5f	N <sub>4,5</sub>
3d → 5f	M <sub>4,5</sub>
2p → 4d	L <sub>2,3</sub>
2p → 5d	L <sub>2,3</sub>

### 1.3 Chirality in EELS

Chirality is an important property of asymmetry in several branches of science. The word chirality is derived from the Greek,  $\chi\epsilon\iota\rho$ , "hand", a familiar chiral object. An object

or a system is chiral if it is distinguishable from its mirror image; that is, it cannot be superposed onto it. Conversely, a mirror image of an achiral object, such as a sphere, cannot be distinguished from the object.

In EELS, a beam of electrons is taken as the light source. It is the fundamental difference with some other spectroscopic techniques, where the light source is a beam of photons, e.g. XAS (X-ray absorption spectroscopy). Similarities between XAS and EELS in a transmission electron microscope have long been recognized, and EELS has been compared with XAS. It is known that the photon light source can be polarized circularly with positive or negative helicity, largely extending its application, so it is also interesting to study if the electron beam has the possibility of the similar helicity<sup>5</sup>. We start from the DDSCS.

As aforesaid, DDSCS is representative of the energy-loss spectrum due to inelastic electron scattering. The basic expression for DDSCS of an incident plane wave, given in eq. 1.3, can be expressed as:

$$\frac{d^2\sigma}{d\Omega dE} = \frac{4\gamma^2}{a_0^2 q^4} \frac{k_f}{k_i} S(\mathbf{q}, E) \quad (1.4)$$

when summed over all the final and initial states, and the S factor

$$S(\mathbf{q}, E) = \sum_{i,f} \left| \langle f | \mathbf{q} \cdot \mathbf{r} | i \rangle \right|^2 \delta(E_i - E_f + E) \quad (1.5)$$

is called Dynamic Form Factor.  $e^{i\mathbf{q}\cdot\mathbf{r}}$  has been approximated to  $i\mathbf{q} \cdot \mathbf{r}$  by applying dipole approximation for small scattering angles.

We assume that the incident electron creates an electric field at the atom when passing the target. The Fourier component of this electric field corresponding to a specific energy loss is defined as the perturbing oscillatory electric field  $\mathbf{E}$ , transferring the energy  $E = \hbar\omega$  from incident electrons to the target atom, forcing an electron transition in the atom, as sketched in Fig. 1.6(a)<sup>5</sup>. The electric field  $\mathbf{E}$  is parallel to  $\mathbf{q}$ :

$$\mathbf{E} \propto \mathbf{q} \Re \left[ \exp^{i(\omega t + \phi)} \right]$$

where  $\phi$  is a phase angle.



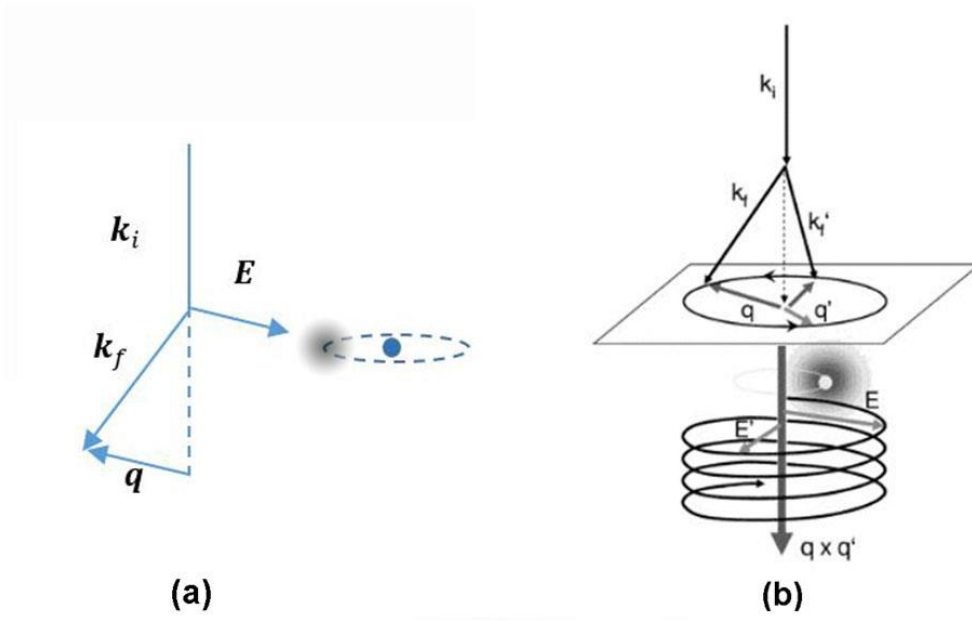


Fig. 1.6. (a) The Fourier component of  $\mathbf{E}$  that gives rise to an electronic transition is parallel to the momentum transfer vector  $\mathbf{q}$ . The target electron is symbolized by a diffused cloud surrounding the nucleus. (b) Principle of realizing helicity of the electric field  $\mathbf{E}$ , by selecting two perpendicular scattering vectors and a relative phase shift of  $\pi/2$ .<sup>5</sup>

If two scattering vectors  $\mathbf{q}$  and  $\mathbf{q}'$  are perpendicular to each other, they exhibit a relative phase difference of  $\pi/2$ . When they are combined, the total perturbing electric field is:

$$\begin{aligned} \mathbf{E} + \mathbf{E}' &= \mathbf{q} \Re[\exp^{i(\omega t + \phi)}] + \mathbf{q}' \Re[\exp^{i(\omega t + \phi + \pi/2)}] = \Re[\exp^{i(\omega t + \phi)} (\mathbf{q} + i\mathbf{q}')] \\ &= \mathbf{q} \cos(\omega t + \phi) - \mathbf{q}' \sin(\omega t + \phi) \end{aligned} \quad (1.6)$$

The electric field  $\mathbf{E} + \mathbf{E}'$  rotates counterclockwise in the plane perpendicular to the arrow  $\mathbf{q} \times \mathbf{q}'$ , when looking along this arrow, as seen in Fig. 1.6(b). If the relative phase difference is set to be  $-\pi/2$ , the electric field  $\mathbf{E} + \mathbf{E}'$  rotates clockwise. These two cases of electron scattering are analog to the absorption of effective photon with positive and negative helicity respectively. This is the departure point of the EMCD, where chiral atomic transitions in a specimen will be accessible with inelastic electron scattering under particular scattering conditions.

How is it possible to detect the two signals at one time and introduce a relative phase shift of  $\pi/2$  or  $-\pi/2$  between the two signals before they interfere? Using a bi-

prism and a phase shifter or a delay line would be possible, but it is extremely difficult to realize it experimentally. Now we present an accessible method, starting with the introduction of relationship between the inelastic interference and DDSCS.

When two incoherent plane waves with identical wave number  $k_i = k_i'$  are incident, we would expect a simple superposition of two DDSCS:

$$\frac{d^2\sigma}{d\Omega dE} = \frac{4\gamma^2}{a_0^2} \frac{k_f}{k_i} \left( \frac{S(\mathbf{q}, E)}{q^4} + \frac{S(\mathbf{q}', E)}{q'^4} \right) \quad (1.7)$$

But when the two plane waves are coherent, there is another interference term in the DDSCS:

$$\frac{d^2\sigma}{d\Omega dE} = \frac{4\gamma^2}{a_0^2} \frac{4k_f}{k_i} \left( \frac{S(\mathbf{q}, E)}{q^4} + \frac{S(\mathbf{q}', E)}{q'^4} + 2\Re \frac{e^{-i\phi} S(\mathbf{q}, \mathbf{q}', E)}{q^2 q'^2} \right) \quad (1.8)$$

Where  $S(\mathbf{q}, \mathbf{q}', E) = \sum_{i,f} \langle f | \mathbf{q} \times \mathbf{r} | i \rangle \langle i | \mathbf{q}' \times \mathbf{r} | f \rangle \delta(E_i - E_f + E)$  is the inelastic interference term, which is called Mixed Dynamic Form Factor (MDFF). The MDFF term contains both  $\mathbf{q}$  and  $\mathbf{q}'$ , so if they are perpendicular to each other and have a phase shift of  $\pi/2$  or  $-\pi/2$ , the DDSCS will contain a contribution from the inelastic electron scattering which is equivalent to absorption of effective photon with positive or negative helicity.

Experimentally, it is possible to select the signal selected from a specific position where  $\mathbf{q} \perp \mathbf{q}'$ , to meet the condition of two perpendicular transfer scattering vectors. Moreover, the crystal itself is found to be an effective beam splitter. It is to take advantage of the dynamical electron diffraction to tune a phase shift of a Bragg diffracted wave to the desired value of  $\pm\pi/2$ . Assuming the two coherent plane waves are the transmission plane wave  $\mathbf{0}$  and one Bragg diffracted wave  $\mathbf{g}$ , the equation 1.8 is to be:

$$\frac{d^2\sigma}{d\Omega dE} = \frac{4\gamma^2}{a_0^2} \frac{4k_f}{k_i} \left( |A_0|^2 \frac{S(\mathbf{q}_0, E)}{q_0^4} + |A_g|^2 \frac{S(\mathbf{q}_g, E)}{q_g^4} + 2\Re \frac{A_0 A_g^* S(\mathbf{q}_0, \mathbf{q}_g, E)}{q_0^2 q_g^2} \right) \quad (1.9)$$

Here, the coefficients  $A_i$  are the amplitudes of the transmission beam and Bragg diffracted beam, and we define  $\mathbf{q}_0 = \mathbf{k}_f - \mathbf{k}_i$ ,  $\mathbf{q}_g = \mathbf{k}_f - \mathbf{k}_i + \mathbf{g}$ . The symmetrized expression for the interference term in Eq. (1.9), equivalent to the helicity of photons, is called chirality:

$$Ch = 2\Im \left[ \frac{AA^* \mathbf{q} \times \mathbf{q}'}{qq'} \right] \mathbf{e}_k$$

$\mathbf{e}_k$  is the unit vector in the direction of the incident electron. In the ideal example shown in Eq. (1.9), achieving a phase shift of  $\pi/2$  between the scattering vectors, we have  $A = 1/\sqrt{2}$  and  $A' = i/\sqrt{2}$ ,  $\mathbf{q} \perp \mathbf{q}'$  the chirality is maximum,  $Ch = 1$ . A mirror operation on the axis, passing through the transmission beam and Bragg diffracted beam, can change the chirality from 1 to -1.

## 2. EMCD technique

The chirality in EELS has been explained and proved in the section 1.3. Considering that helical photons have already been used to obtain magnetic moment information in a magnetic material using X-ray magnetic circular dichroism (XMCD) technique<sup>6</sup>, the chirality in EELS can also be taken advantage to achieve the same kind of information in TEM. This emerging TEM technique was theoretically predicted in 2003<sup>7</sup> and experimentally realized in 2006<sup>8</sup>, and it is named energy-loss magnetic chiral dichroism (EMCD) technique, a counterpart of XMCD. It aims to measure the local magnetic moments of crystalline sample, improving our understanding of magnetic phenomena. In this section, the experimental configuration, signal record methods, data treatment methods and sum rules of EMCD will be introduced. But at first the analogy between EMCD and XMCD has to be made to well explain the principle of EMCD technique.

### 2.1 From XMCD to EMCD

XMCD is based on the fact that the absorption coefficients of circularly polarized X-rays with positive and negative helicity in ferromagnetic or paramagnetic materials are different. When the left- or right-circularly polarized X-ray, which has the circular polarization vector parallel or antiparallel to the external magnetic field, passes through the ferromagnetic sample, the X-ray absorption spectrum (XAS) is detected. The XMCD spectrum is obtained as the difference between the left- and right-circularly polarized XAS spectra. But why and how the magnetic moment information can be extracted from the XMCD spectrum?

In a simple picture, a two-step model<sup>9</sup> is used to describe the XMCD (see Fig. 1.7). We consider the 3d transition metal atom as an example. The first step is the absorption of circularly polarized photons by an atom in an initial p-state. For photon absorption in a p-state corresponding to the L<sub>2,3</sub>-absorption process, the transition can only happen from p-state to either a final s-state or d-state according to dipole selection rules. Regarding the absorption coefficient into a final s-state is much weaker than that into d-state, we can neglect the transition to s-state and only focus on the p→d transition. Second, we consider the absorption of circularly polarized photon. The 2p core state of a 3d metal is split into a J=3/2 level (2p<sub>3/2</sub> level corresponding to L<sub>3</sub> edge) and a J=1/2 level (2p<sub>1/2</sub> level corresponding to L<sub>2</sub> edge), due to spin-orbit coupling. In the electron transitions from 2p states to final 3d states, the spin-flip is generally forbidden, so the spin magnetic moment is not changed:  $\Delta m_s = 0$ . However, the different helicities of the photons impose different constraints for the change of the orbital magnetic moment  $m_l$ . Only  $\Delta m_l = +1$  is allowed in the transition excited by right-circularly polarized photon (helicity +1), and  $\Delta m_l = -1$  for left-circularly photon (helicity -1). As a result, X-rays with helicity +1 excite 62.5% spin up electrons and those with helicity -1 excite 37.5% spin-up electrons from the 2p<sub>3/2</sub> level, while for the 2p<sub>1/2</sub> level, X-rays with helicity +1 excite 25% spin-up and those with helicity -1 excite 75% spin-up. That is to say, X-rays with helicity +1 and helicity -1 excite different proportions of spin-up electrons during transition. The second step is that the unoccupied 3d valence band accepts the excited electrons. The spin-up holes accept only the spin-up excited electrons, and the spin-down holes accept only the spin-down ones. If there is a difference between the spin-up and spin-down holes in 3d valence band, which also means there is a 3d magnetic moment, the absorption of spin-up and spin-down excited electrons will differ. Thus the final absorption spectra of X-ray with helicity +1 and -1 will be different for both L<sub>3</sub> and L<sub>2</sub> peaks. This difference carries the information of the unoccupied 3d valence states, which is related to the 3d magnetic moment. The magnetic moment can be calculated from the spectra difference by applying the XMCD sum rules to it.

The discovery of EMCD originates from the early consideration that the role of polarization vector  $\boldsymbol{\varepsilon}$  in XAS is similar to the role of the wave vector transfer  $\mathbf{q}$  in EELS<sup>5</sup>. To explain it, the MDFF mentioned in the last section can be written in another form as follow:

$$S(\mathbf{q}, \mathbf{q}', E) = \left[ \frac{(r_+ + r_-) \mathbf{q}_\perp \cdot \mathbf{q}'_\perp}{2} \right] + r_0 q_z q'_z + \frac{i}{2} (r_+ - r_-) |\mathbf{q}_\perp \times \mathbf{q}'_\perp| \quad (1.10)$$

where  $r_+$ ,  $r_-$  and  $r_0$  means the transition probabilities from states  $|nlm\rangle$  to  $|nlm'\rangle$  with  $m' = m + 1, m - 1, \text{ or } m$ . This formula divides MDFD into a real part and an imaginary part. It is found that when  $\mathbf{q}$  and  $\mathbf{q}'$  are exchanged, the imaginary part changes its sign but the real part stays the same. For  $S(\mathbf{q}, E)$  ( $\mathbf{q} = \mathbf{q}'$  in eq. 1.10), it contains no imaginary part due to  $\mathbf{q}_\perp \times \mathbf{q}'_\perp = 0$ . So if  $\mathbf{q} = \mathbf{q}'$ ,  $\mathbf{q} \perp \mathbf{q}'$  and phase difference  $\phi = \pi/2$ , we subtract the DDSCS obtained in two conditions where the  $\mathbf{q}$  and  $\mathbf{q} \perp \mathbf{q}'$  are exchanged or not, as shown in Eq. (1.11), we only obtain the imaginary part in MDFD. The imaginary part can be finally interpreted as the difference in probability to change the magnetic quantum number by  $\pm 1$ . Eq. (1.11) is also an expression of the dichroic or chiral signal in EMCD, analog to the XAS spectra difference in XMCD.

$$\Delta\sigma = \left. \frac{d^2\sigma}{d\Omega dE} \right|_q^+ - \left. \frac{d^2\sigma}{d\Omega dE} \right|_q^- \quad (1.11)$$

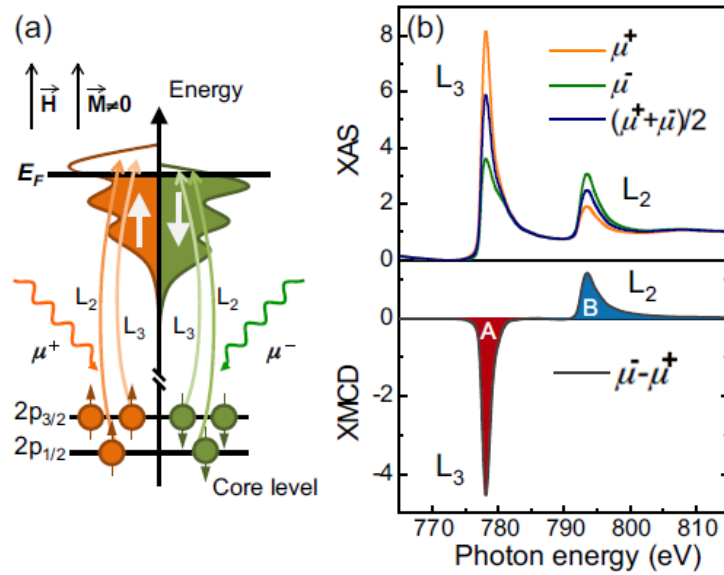


Fig. 1.7. (a) Absorption of X-rays with helicity +1 and -1 by 3d transition metal. (b) An example of XAS spectra and XMCD signal<sup>9</sup>.

## 2.2. EMCD sum rules

Since the sum rules for EMCD were derived<sup>10,11</sup>, the quantitative measurement of spin and orbital moments of specific element can be realized in a way similar to XMCD. For 3d transition metal atom, the EMCD sum rules can be written as Eq. (1.12-1.14)<sup>10</sup>.  $\sigma_2 - \sigma_1$  is the chiral dichroic signal. The expression  $\int_{L_3} (\sigma_2 - \sigma_1) dE$  means the integrated value of the difference spectrum within the energy-loss range corresponding to  $L_3$  peak.  $\langle L_z \rangle$ ,  $\langle S_z \rangle$ ,  $\langle T_z \rangle$  are respectively the ground-state values of orbital momentum, spin momentum and magnetic dipole operators.  $m_l$  and  $m_s$  are respectively the corresponding orbital and spin magnetic moment, expressed as  $m_l = \langle L_z \rangle \mu_B / \hbar$  and  $m_s = 2 \langle S_z \rangle \mu_B / \hbar$ .  $\langle T_z \rangle$  is negligible compared to  $\langle S_z \rangle$  for 3d transition atoms<sup>12</sup>. The coefficient  $K$  contains all the information related to the dynamical diffraction effects which is linked to the interaction of electrons with a regular lattice<sup>10</sup>. This coefficient depends on the excitation error of the incident beam, specimen thickness, detector position, and aperture size, *etc.* In the Eq. (1.14), the  $K$  factor is canceled when calculating the spin-to-orbital moment ratio. That is to say, the measured spin-to-orbital moment ratio is independent of any dynamical coefficient, sample orientation and thickness.

$$\frac{\int_{L_3} (\sigma_2 - \sigma_1) dE - 2 \int_{L_2} (\sigma_2 - \sigma_1) dE}{\int_{L_2+L_3} (\sigma_2 + \sigma_1) dE} = K \left( \frac{2 \langle S_z \rangle}{3 N_h} + \frac{7 \langle T_z \rangle}{3 N_h} \right) \quad (1.12)$$

$$\frac{\int_{L_2+L_3} (\sigma_2 - \sigma_1) dE}{\int_{L_2+L_3} (\sigma_2 + \sigma_1) dE} = K \frac{\langle L_z \rangle}{2 N_h} \quad (1.13)$$

$$\frac{\int_{L_3} (\sigma_2 - \sigma_1) dE - 2 \int_{L_2} (\sigma_2 - \sigma_1) dE}{\int_{L_2+L_3} (\sigma_2 - \sigma_1) dE} = \frac{4 \langle S_z \rangle + 14 \langle T_z \rangle}{3 \langle L_z \rangle} \quad (1.14)$$

The application condition of these sum rules to the EMCD signal has been further studied to discuss and improve the accuracy of quantitative analysis. The three-beam geometry is proposed to fulfill the symmetry sum rules requirements, making it preferable for quantitative measurement than two-beam geometry<sup>13</sup>. In addition, the influence of factors such as plural scattering<sup>14</sup> and experimental setup parameters<sup>15</sup> on the detected

signal are discussed, in order to interpret the error source of quantitative spin-to-moment ratio by applying sum rules. In the exploration of excellent performance in quantitative analysis, it was found and experimentally verified that EMCD has some more unique advantages compared with XMCD. L. Calmels *et al.*<sup>16</sup> pointed out through theoretical analysis that EMCD is site-specific. EMCD spectra recorded at the  $L_{2,3}$  edge of Fe contains contribution from different nonequivalent atomic sites in the crystal and the contribution of each site can be isolated, by changing the position of detector, sample orientation and thickness. Z. Q. Wang *et al.*<sup>17</sup> published a site-specific EMCD method, experimentally demonstrating quantitative measurement of atomic site-specific magnetic structure information on a nanometer scale, from one  $NiFe_2O_4$  nanograin in composite films.

## 2.3 Experimental setup

### 2.3.1 Detection of EELS spectrum

To obtain an EELS spectrum in a TEM, a spectrometer and a detector are commonly used. There are two types of position of the spectrometer. One is post-column energy filter (e.g. Gatan image filter), which can be added to an existing TEM column. The other is in-column energy filter, such as Omega filter, Alpha filter, Wien filter, Mandoline filter, *etc.* As a free attachment to TEM, post-column spectrometer is commonly used. In Fig. 1.8, we can see its general structure from the cross-sectional view of Gatan energy-filtered spectrometer, or called Gatan image filter (GIF).

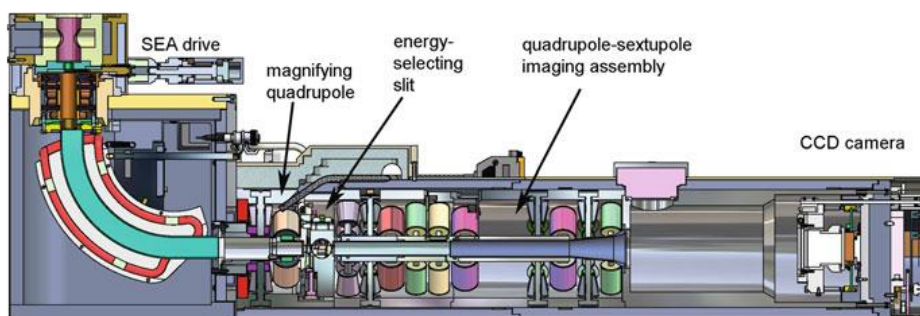


Fig. 1.8. Cross section of a Gatan GIF Tridiem energy-filtering spectrometer<sup>1</sup>.

In this system, the electron beam firstly passes through the spectrometer entrance aperture (SEA) close to TEM screen, and then undergoes bending, dispersion and focusing with the sectorial magnetic prim. Similar to the fact that the white light beam passing through glass prism will be dispersed into several light beams with different wavelength, electrons with different energy have different exit angles and will be focused or double focused in different positions on image plane of the prism (dispersion plane). In the way of double focusing, electrons with the same energy are focused in two perpendicular directions, but not in a single direction, thus finally the electrons are dispersed in a plane instead of a line. A very important parameter of spectrometer is the dispersion, representing the displacement of the focus per unit change of electron energy. Besides, magnetic prim also suffers aberration like any other optical element, so the multipole lens system is applied to correct aberration.

The GIF spectrometer can be operated in two modes for different purposes: EELS and EFTEM. The intensity distribution on dispersion plane can be recorded by CCD camera after aberration correction by multipole lenses, providing us EELS spectrum. The data of CCD will be saved by computer for further process. Moreover, if a slit at the dispersion plane is inserted to select electrons within a specific range of energy loss, the chosen electrons can recombine to form an image or diffraction pattern (known as energy filtered image or diffraction pattern) with the use of multipole lens system on CCD. The slit is controlled by piezoelectric transducer to choose any energy range we need, then we can obtain some information more conveniently.

In addition, the electron beam entering the spectrometer comes from the TEM column, therefore the properties of TEM lenses and the way in which they work have great influence on the performance of EELS. For post-column spectrometer, there are two kinds of coupling between spectrometer and TEM: TEM-image coupled and TEM-diffraction coupled. Fig. 1.9 is the schematic ray diagram of the two coupling ways.

If TEM works in image mode, an image of the specimen of magnification  $M$  is projected on the screen and a small diffraction pattern exists in the projector lens crossover. In this condition, it is the diffraction pattern that is on the spectrometer object plane, so the spectrometer is said to be diffraction coupled. The angular range of scattered electrons entering into spectrometer is controlled by the objective lens aperture, and the area of specimen contributing to EELS spectrum is determined by the spectrometer entrance aperture size. If TEM is operated in diffraction mode, conversely a small image



is at the projector lens crossover and a diffraction pattern on the screen, so it is called TEM-image coupled. In TEM-image coupled mode, the area of specimen being analyzed is usually controlled by selected area aperture.

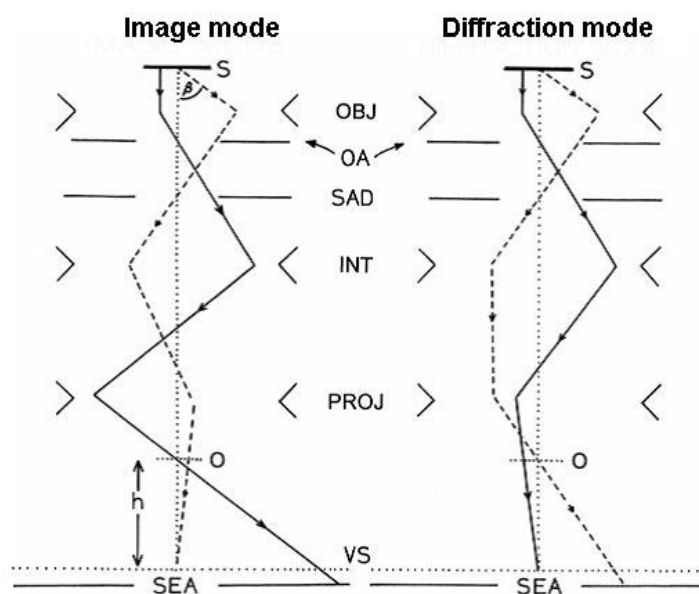


Fig. 1.9. Simplified optics for the image and diffraction modes of a conventional TEM. *S* represents the specimen; *OBJ*, *INT*, and *PROJ* represent the objective lens, intermediate-lens system, and final imaging (projector) lens. *O* and *VS* are the spectrometer object point and viewing screen; *OA*, *SAD*, and *SEA* are the objective, selected area diffraction and spectrometer entrance apertures<sup>1</sup>.

So we can understand that many factors will contribute to the energy resolution. For example, it is possible that the incident electrons are not monochromatic, resulted from the energy spread of gun or instability of high tension; the aberration, although partly corrected by multipole lens system, is still limiting the energy resolution; the CCD camera cannot be a perfectly record the projected image. The energy resolution can be indicated by the full width at half maximum of zero-loss peak in EELS spectrum. Understanding of these factors is necessary for better interpretation of acquired data.

### 2.3.2 EMCD experimental methods

In this section, we focus on the development of EMCD experimental setups. Fig. 1.10 sketches the basic experimental configuration<sup>18</sup>. A crystalline sample is tilted to

reach a two beam condition as shown in Fig. 1.10(a). In EMCD, the dichroism signal is the relative difference of EELS spectra recorded at two chiral positions<sup>8</sup>. These two positions are symmetrical points located on the Thales circle passing through the transmission spot and a Bragg spot on the diffraction pattern as indicated in fig. 1.10(b). At the two specific positions, different combinations of two perpendicular electron scattering vectors  $\mathbf{q}$  and  $\mathbf{q}'$  give rise to left- and right-handed polarized virtual photons, which are analog to circular polarized X-ray in XMCD. As previously mentioned in section 1.3, here the crystalline sample itself works as a beam splitter to achieve a phase shift of  $\pi/2$  between  $\mathbf{q}$  and  $\mathbf{q}'$ , otherwise there is no coherence and no interference term as well. This is a drawback of using the crystal as a beam splitter. Actually, since P. Schattschneider *et al.* realized the experiment of magnetic circular dichroism in a TEM in 2006<sup>8</sup>, experimental setups, signal recording methods, data processing methods have been constantly improved to make EMCD a more efficient technique<sup>19,20,21,22,23,24</sup>. It seems that they all have their own advantages and disadvantages.

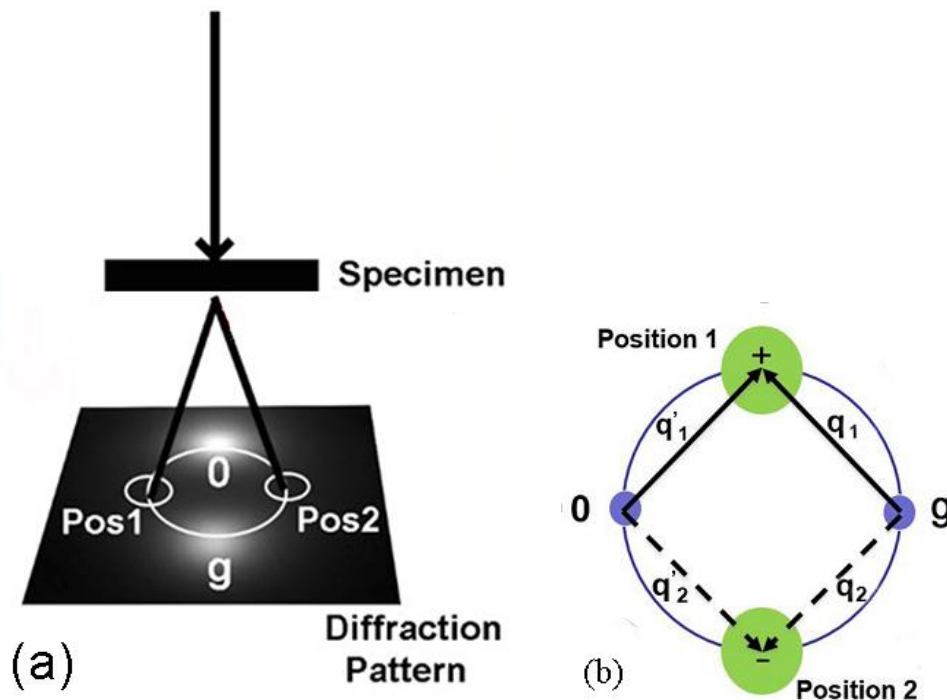
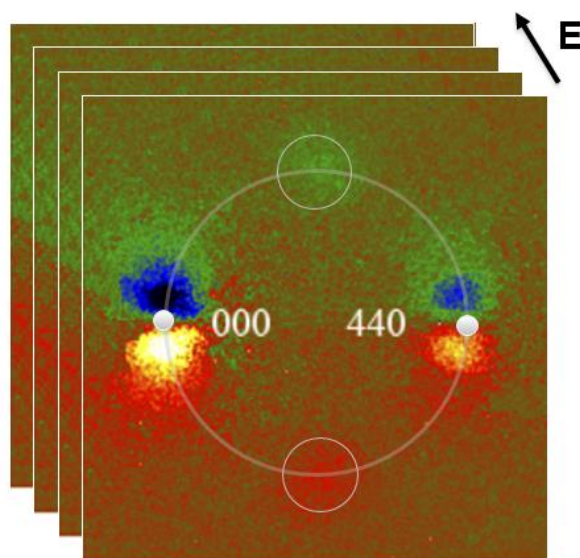


Fig. 1.10. (a) The basic EMCD experimental configuration. (b) Positions of the two virtual entrance apertures on the diffraction pattern for measurement of EMCD (green disks). The transmission spot  $\mathbf{0}$  and diffraction spot  $\mathbf{g}$  are represented (blue dots).

For diffraction setup, there are two ways to select  $\mathbf{q} \perp \mathbf{q}'$  in the diffraction pattern. In the first way, the microscope is operated in image mode. The selection of  $\mathbf{q} \perp \mathbf{q}'$  in diffraction pattern is obtained by objective aperture (OA), and the target area of specimen is selected by the projected spectrometer entrance aperture (SEA) in image mode<sup>21</sup>. To record the spectrum in a reversed chirality, OA is shifted from one symmetry point on the Thales circle to the other one. Since the spatial resolution is determined by the area which is given by the projection of SEA, nanometer range can be achieved by setting higher magnification. However, it has obvious drawbacks in positioning both OA and SEA. First, this method works in image mode, so it is inconvenient to switch between image mode and diffraction mode twice for positioning two chiral points in diffraction plane with OA. Besides, it is not accurate to select investigated area with SEA and also not accurate to position OA aperture. In the second way, in which the microscope works in diffraction mode, these disadvantages are overcome. The selection of  $\mathbf{q} \perp \mathbf{q}'$  can be made by SEA and the investigated specimen area by selected area aperture (SAA)<sup>21,25</sup>. Diffraction pattern is shifted with respect to SEA, thus spectra in two chiral points are recorded. The biggest problem of this method is that the intensity is low, thus the signal is weak. It is because much electron beam is blocked out by SAA, especially when parallel illumination is applied. What is more, the spatial resolution is determined by the size of SAA, so it will not be better than 100nm. The related background knowledge of the TEM to understand the experimental configurations mentioned above is demonstrated in Appendix I.

In order to increase the intensity, LACDIF setup<sup>19,26</sup> was proposed to obtain a sharp diffraction pattern in image mode. This is achieved by converging the beam on the specimen, which is raised from the eucentric position by a distance of  $z$ . The investigated specimen area, given by the cone of illumination, is significantly reduced, allowing spatial resolution of 10 nm or better<sup>25</sup>. In this case, no SAA in this method is used to block out intensity, so the signal to noise ratio is largely increased. Another advantage of LACDIF setup is that the configuration is less sensitive to the exact crystal orientation, given that the incident cone averages over a wide distribution of incident directions. The LACDIF setup has been commonly used in EMCD experiment and many efforts were then taken to further increase spatial resolution and improve signal to noise ratio<sup>19,27,28</sup>.

With the LACDIF setup, the way of recording the signal for higher signal to noise ratio was discussed<sup>19,25</sup>. One is to record the  $(q, E)$  diagram using rotational sample holder to align the reciprocal lattice vector  $\mathbf{g}$  parallel to energy dispersive axis of CCD camera. Therefore the entire range of spectra vertical to energy dispersive axis can be recorded, instead of the spectra with a single acquisition<sup>25</sup>. The other one is to record a series of energy filtered diffraction patterns so as to construct dichroic spectra. The energy spectrum imaging (ESI) is used to map the inelastic signal in a data cube of scattering angle and energy loss, as shown in Fig. 1.11<sup>19</sup>. With the ESI technique, the positions of the virtual entrance apertures can be determined accurately during post-process data treatment. It successfully avoids the problem of locating the spectrometer entrance aperture (SEA) or objective aperture (OA) which is tough to be located accurately on the two specific positions. Post corrections of non-isochromaticity and spatial drift were achieved in our case using a home-made Digital-Micrograph image processing package<sup>28,29</sup>.



*Fig. 1.11. A series of energy filtered diffraction patterns are recorded so as to construct the chiral spectra with ESI method<sup>19</sup>.*

In addition, Verbeeck et al.<sup>30</sup> optimized the position and size of entrance aperture in EMCD experiment, discussing the impact of the detection position and scope on the EMCD signal detection. P. Schattschneider et al.<sup>27</sup> presented a new setup operated in STEM in which the crystal is tilted to a three-beam case instead of two, realizing the

resolution of 2nm. Actually in an ultimate case of tailored beams, the spatial resolution can be even less<sup>31,32</sup>. Recently, S. Muto et al.<sup>24</sup> developed a new method for extraction of EMCD spectra from energy-filtered diffraction pattern without symmetry and orientation of the crystal, with a multivariate curve resolution technique. It is expected to simplify the future analysis and extraction of EMCD spectra. What is more, generation of electron beams carrying orbital angular momentum<sup>33</sup> and vortex electron beam<sup>22</sup> made the specific condition of diffraction no longer necessary for EMCD experiment. However, P. Schattschneider in 2014 published a paper named “is magnetic chiral dichroism feasible with electron vortices” that the EMCD signal cannot be detected with vortex beam. These achievements promote the EMCD technique continually and higher resolution as well as more practical improvements is open for researchers in electron microscopy science.

#### **2.4 EMCD: summary of literature outcome**

Practically EMCD technique has been applied to material science in recent years. In 2009, Zhang *et al.* proved the intrinsic ferromagnetism of diluted magnetic semiconductor (DMS) nanowire of ZnO doped with Fe and Co with EMCD technique<sup>34</sup>. DMS can be hopefully applied to spintronics and thus receives an intensive attention on developing it. Che et al. studied the domain walls of permalloy with EMCD technique under Lorentz mode of transmission electron microscope<sup>35</sup>. Warot-fonrose et al. investigated the sensitivity of the method to the magnetic properties on a series of  $\text{Fe}_x\text{Co}_{1-x}$  alloys<sup>36</sup>. Salafranca et al. in 2012 used EMCD technique to map the magnetization of metal-oxide nanoparticles in real space with sub-nanometer spatial resolution<sup>37</sup>. Dong et al. in 2015 characterized the magnetic properties of  $\text{Y}_3\text{Fe}_5\text{O}_{12}$  (YIG)/Pt interface with EMCD technique, together with the atomic and electronic structure in TEM, to correlate the microstructure and magnetic properties with interfacial transport properties. It provides the knowledge of controlling the interfacial structure and properties to obtain higher spin transport efficiency<sup>38</sup>. These applications of EMCD technique in material science will help both understanding and designing of new devices in spintronics, multiferroics or magnetic storage technology. We make a summary of EMCD results from literature in Table 1.2.

Table 1.2. EMCD results in literature.  $\Delta\sigma/\sigma$  is the relative EMCD signal (difference of the two EELS spectra acquired in two chiral points divided by their sum).

Reference	Sample (thickness)		$\Delta\sigma/\sigma$	Orbital to spin moment ratio ml/ms	Experimental Setup	Spatial Resolution
8	Fe single crystal(10±2nm)		7%±8%		Objective aperture(OA)/Detector shift In (110) two beam condition	
10	Fe single crystal			0.09±0.03	large angle convergent diffraction(LACDIF) and (energy spectrum imaging (ESI) In (110) two beam condition	
27	Fe layer in Fe/Au multilayer				Convergent beam electron diffraction (CBED) with STEM mode in ±(200) three beam condition	2nm
39	Fe single crystal(19±2nm)		8%	0.09±0.01	ESI in (200) two beam condition	Potential for Subnanometer
				0.08±0.01	ESI and Double difference procedure in ±(200) three beam condition	
28	Fe single crystal(10nm)		20%	0.065±0.005	LACBED and ESI in ±(110) three beam condition	~40nm
15	Fe single crystal(25nm)			0.08±0.01	Reciprocal space map in ±(200) three beam condition	~600nm
					OA shift and real space map In ±(200) three beam condition	~2nm
14	Fe single crystal		30%	0.04±0.01	Data treatment with Double difference and plasmon removal	
40	Fe single crystal (10-40nm)			e.g. 0.029±0.002 for 10nm 0.024±0.0006 for 20nm	Data treatment with Multivariate curve resolution technique in free beam condition	
17	NiFe2O4 single crystal (29nm and 42nm)	Fe edge	33%	0.01±0.02 for Octahedral Fe 0.06±0.02 for Tetrahedral Fe	detector shift In ±(004) and ±(2 $\bar{2}$ 0) three beam condition	~50nm
		Ni edge	42%	0.24±0.02 for Ni		
24	Polycrystalline Fe (30nm)		20%	0.0429±0.0075	acquiring hundreds of spectra without restriction in STEM mode	A few nanometer
19	Fe <sub>3</sub> O <sub>4</sub> (Fe-L edge) (40nm)		~15%		LACBED and ESI In (440) two beam condition	10nm-40nm
20	Co, Ni single crystal(~50nm)				Comparison of OA shift, Detector shift and LACDIF	30nm-200nm
25	Co single crystal (18±3nm)		~5%		LACDIF and q-E diagram In (10 $\bar{1}$ 0) two beam condition	Towards 10nm
23	Co single crystal			0.14±0.03	LACDIF and SED	30nm
34	Co,Fe doped in ZnO				Under Lorenz mode in (0002)two beam condition	
41	Heusler alloy Ni2MnSn(25nm)	Mn edge	9%		Detector Shift Method In three beam condition	~1nm
		Ni edge	16%			
42	NiFe2O4 (NFO)	Fe and Ni edge				
	CoFe2O4(CFO)					

In conclusion, this chapter introduces the EMCD technique from the aspects of theory and experiment. The physics of EELS is presented in the beginning as necessary background knowledge to understand EMCD. The possibility to achieve the chirality in EELS, which is a precondition of EMCD, is particularly discussed. Then using XMCD as an analog, the theoretical principle of EMCD is illustrated, and the EMCD sum rules

are presented. What follows is a review on the development of EMCD experimental setup as well as its applications in recent years. From the review, we can see that EMCD is still on its way to be a routine characterization tool, and it is interesting to explore this technique of high potential.

## Bibliography

1. Ray Egerton, *Electron Energy-Loss Spectroscopy in the Electron Microscope*, (Springer, 2015)
2. Wang, Z. L. & Cowley, J. M. Reflection electron energy loss spectroscopy (reels): A technique for the study of surfaces. *Surf. Sci.* **193**, 501–512 (1988).
3. Ahn, C. C. *Transmission Electron Energy Loss Spectrometry in Materials Science and the EELS Atlas*. (John Wiley & Sons, 2006).
4. Leo, W. R. *Techniques for Nuclear and Particle Physics Experiments: A How-To Approach*. (Springer Science & Business Media, 1994).
5. Schattschneider, P. *Linear and Chiral Dichroism in the Electron Microscope*. (CRC Press, 2012).
6. Van der Laan, G. & Thole, B. T. Strong magnetic x-ray dichroism in 2p absorption spectra of 3d transition-metal ions. *Phys. Rev. B* **43**, 13401–13411 (1991).
7. Hébert, C. & Schattschneider, P. A proposal for dichroic experiments in the electron microscope. *Ultramicroscopy* **96**, 463–468 (2003).
8. Schattschneider, P. *et al.* Detection of magnetic circular dichroism using a transmission electron microscope. *Nature* **441**, 486–488 (2006).
9. Van der Laan, G. & Figueroa, A. I. X-ray magnetic circular dichroism—A versatile tool to study magnetism. *Coord. Chem. Rev.* **277-278**, 95-129, 2014.
10. Calmels, L. *et al.* Experimental application of sum rules for electron energy loss magnetic chiral dichroism. *Phys. Rev. B* **76**, 060409 (2007).
11. Rusz, J., Eriksson, O., Novák, P. & Oppeneer, P. M. Sum rules for electron energy loss near edge spectra. *Phys. Rev. B* **76**, 060408 (2007).
12. Carra, P., Thole, B. T., Altarelli, M. & Wang, X. X-ray circular dichroism and local magnetic fields. *Phys. Rev. Lett.* **70**, 694–697 (1993).
13. Rusz, J. *et al.* Quantitative magnetic measurements with transmission electron microscope. *J. Magn. Magn. Mater.* **322**, 1478–1480 (2010).
14. Rusz, J. *et al.* Influence of plural scattering on the quantitative determination of spin and orbital moments in electron magnetic chiral dichroism measurements. *Phys. Rev. B* **83**, 132402 (2011).
15. Lidbaum, H. *et al.* Reciprocal and real space maps for EMCD experiments. *Ultramicroscopy* **110**, 1380–1389 (2010).



16. Calmels, L. & Rusz, J. Atomic site sensitivity of the energy loss magnetic chiral dichroic spectra of complex oxides. *J. Appl. Phys.* **109**, 07D328 (2011).
17. Wang, Z. Q., Zhong, X. Y., Yu, R., Cheng, Z. Y. & Zhu, J. Quantitative experimental determination of site-specific magnetic structures by transmitted electrons. *Nat. Commun.* **4**, 1395 (2013).
18. Rusz, J., Rubino, S. & Schattschneider, P. First-principles theory of chiral dichroism in electron microscopy applied to 3d ferromagnets. *Phys. Rev. B* **75**, 214425 (2007).
19. Warot-Fonrose, B. *et al.* Mapping inelastic intensities in diffraction patterns of magnetic samples using the energy spectrum imaging technique. *Ultramicroscopy* **108**, 393–398 (2008).
20. Hébert, C. *et al.* Magnetic circular dichroism in electron energy loss spectrometry. *Ultramicroscopy* **108**, 277–284 (2008).
21. Rubino, S. *et al.* Energy-loss magnetic chiral dichroism (EMCD): Magnetic chiral dichroism in the electron microscope. *J. Mater. Res.* **23**, 2582–2590 (2008).
22. Verbeeck, J., Tian, H. & Schattschneider, P. Production and application of electron vortex beams. *Nature* **467**, 301–304 (2010).
23. Schattschneider, P. *et al.* Energy loss magnetic chiral dichroism: A new technique for the study of magnetic properties in the electron microscope (invited). *J. Appl. Phys.* **103**, 07D931 (2008).
24. Muto, S. *et al.* Quantitative characterization of nanoscale polycrystalline magnets with electron magnetic circular dichroism. *Nat. Commun.* **5**, 1-7,(2014).
25. Schattschneider, P. *et al.* Magnetic circular dichroism in EELS: Towards 10 nm resolution. *Ultramicroscopy* **108**, 433–438 (2008).
26. Morniroli, J. P. *et al.* LACDIF, a new electron diffraction technique obtained with the LACBED configuration and a Cs corrector: Comparison with electron precession. *Ultramicroscopy* **108**, 100–115 (2008).
27. Schattschneider, P. *et al.* Detection of magnetic circular dichroism on the two-nanometer scale. *Phys. Rev. B* **78**, 104413 (2008).
28. Warot-Fonrose, B., Gatel, C., Calmels, L., Serin, V. & Schattschneider, P. Effect of spatial and energy distortions on energy-loss magnetic chiral dichroism measurements: Application to an iron thin film. *Ultramicroscopy* **110**, 1033–1037 (2010).
29. Gatel, C., Warot-Fonrose, B. & Schattschneider, P. Distortion corrections of ESI data cubes for magnetic studies. *Ultramicroscopy* **109**, 1465–1471 (2009).
30. Verbeeck, J. *et al.* Optimal aperture sizes and positions for EMCD experiments. *Ultramicroscopy* **108**, 865–872 (2008).

31. Pohl, D., Schneider, S., Rusz, J. & Rellinghaus, B. Electron vortex beams prepared by a spiral aperture with the goal to measure EMCD on ferromagnetic films via STEM. *Ultramicroscopy* **150**, 16–22 (2015).
32. Schattschneider, P. *et al.* Real space maps of magnetic moments on the atomic scale: Theory and feasibility. *Ultramicroscopy* **110**, 1038–1041 (2010).
33. Uchida, M. & Tonomura, A. Generation of electron beams carrying orbital angular momentum. *Nature* **464**, 737–739 (2010).
34. Zhang, Z. H. *et al.* Evidence of intrinsic ferromagnetism in individual dilute magnetic semiconducting nanostructures. *Nat. Nanotechnol.* **4**, 523–527 (2009).
35. Che, R. C., Liang, C. Y., He, X., Liu, H. H. & Duan, X. F. Characterization of magnetic domain walls using electron magnetic chiral dichroism. *Sci. Technol. Adv. Mater.* **12**, 025004 (2011).
36. Warot-Fonrose, B. *et al.* Magnetic properties of FeCo alloys measured by energy-loss magnetic chiral dichroism. *J. Appl. Phys.* **107**, 09D301 (2010).
37. Salafranca, J. *et al.* Surfactant Organic Molecules Restore Magnetism in Metal-Oxide Nanoparticle Surfaces. *Nano Lett.* **12**, 2499–2503 (2012).
38. Song, D., Ma, L., Zhou, S. & Zhu, J. Oxygen deficiency induced deterioration in microstructure and magnetic properties at Y<sub>3</sub>Fe<sub>5</sub>O<sub>12</sub>/Pt interface. *Appl. Phys. Lett.* **107**, 042401 (2015).
39. Lidbaum, H. *et al.* Quantitative Magnetic Information from Reciprocal Space Maps in Transmission Electron Microscopy. *Phys. Rev. Lett.* **102**, 037201 (2009).
40. Muto, S., Tatsumi, K. & Rusz, J. Parameter-free extraction of EMCD from an energy-filtered diffraction datacube using multivariate curve resolution. *Ultramicroscopy* **125**, 89–96 (2013).
41. Ennen, I. *et al.* Site-specific chirality in magnetic transitions. *J. Magn. Magn. Mater.* **324**, 2723–2726 (2012).
42. Loukya, B. *et al.* Effect of Bloch wave electron propagation and momentum-resolved signal detection on the quantitative and site-specific electron magnetic chiral dichroism of magnetic spinel oxide thin films. *Phys. Rev. B* **91**, 134412 (2015).



## Chapter II

### Epitaxial MnAs Thin Films on GaAs Substrate

---

The first studies concerning MnAs were reported about 100 years ago by Heusler<sup>1</sup>. Since ferromagnetism with Curie temperature  $T_c \approx 40^\circ\text{C}$  was firstly observed in this metallic compound in 1911<sup>2</sup>, particular attention has been paid to the transition between ferromagnetic  $\alpha$ -MnAs and paramagnetic (or antiferromagnetic as controversially discussed<sup>3,4</sup>)  $\beta$ -MnAs<sup>5,6</sup>. Over the last two decades, with the high interest in hybrid ferromagnetic-semiconductor structures, epitaxial MnAs thin films grown on GaAs substrate have been extensively studied due to its potential applications in spin injection<sup>7,8</sup>, magnetic tunnel junction<sup>9,10</sup> and magnetologic devices<sup>11</sup>. MnAs thin films exhibit more complex magnetic properties compared to bulk MnAs, and they are known to have interesting microstructures, which are self-organized periodic stripes of both two phases in the temperature range of around  $15^\circ\text{C}$  to  $45^\circ\text{C}$ <sup>12,13</sup>.

In this chapter, I will summarize the knowledge on the crystallographic structure, micromagnetic structure and magnetization of MnAs films grown on GaAs substrate. Our EMCD experimental results on this type of samples will be demonstrated in chapter IV.

#### 1. Crystallographic Structure

Fig. 2.1 displays the conventional cell of  $\alpha$ -MnAs,  $\beta$ -MnAs and GaAs.  $\alpha$ -MnAs crystalizes in the hexagonal NiAs-type structure<sup>6</sup>. When it transforms into  $\beta$  phase, the crystal presents orthorhombic MnP-type structure with small displacement of Mn atoms<sup>6</sup>. We can notice their similarity by comparing Fig. 2.1(a) and (b). Thus the  $\beta$ -phase is also considered to be quasi-hexagonal<sup>14</sup>. GaAs crystalizes in cubic ZnS-type structure. In all the contents below, MnAs is in hexagonal structure unless otherwise specified.

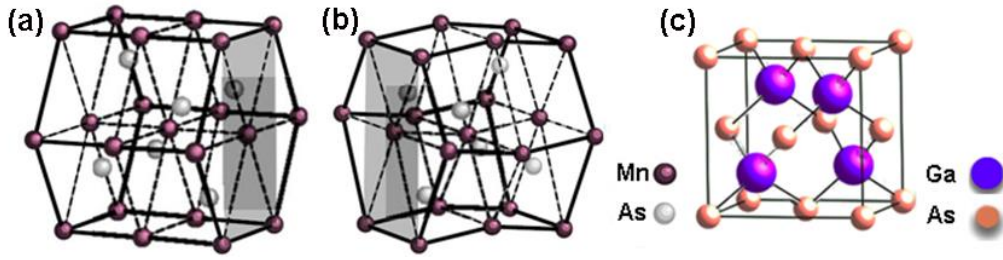


Fig. 2.1. <sup>15</sup>(a) The conventional cell of (a) MnAs in  $\alpha$ -phase and (b)  $\beta$ -phase, (c) GaAs.

MnAs films on GaAs substrate can be grown by MBE in various orientations. Different types of hetero-structures namely MnAs/GaAs(001)<sup>16,17</sup>, MnAs/GaAs(110)<sup>18</sup>, MnAs/GaAs(113)A<sup>19</sup> and MnAs/GaAs(111)<sup>20,21</sup> have been synthesized and studied so far<sup>13</sup>. They exhibit different interface structures, as well as different optical, electronic and magnetic properties. Table 2.1<sup>13</sup> summarizes all the types studied in recent years. The first column is the growth surface of GaAs substrate, and the second column is the growth plane of MnAs. For convenience, the crystal axes and planes of hexagonal structure are specified in Fig. 2.2(a).

Table 2.1. <sup>13</sup>Various orientations of MnAs on substrate GaAs

GaAs	MnAs	Azimuthal orientation	Notation
(001)	( $\bar{1}\bar{1}00$ )	MnAs[ $11\bar{2}0$ ] $\parallel$ GaAs[110] MnAs[0001] $\parallel$ GaAs[ $1\bar{1}0$ ]	A-A <sub>0</sub>
	( $\bar{1}\bar{1}01$ )	MnAs[ $11\bar{2}0$ ] $\parallel$ GaAs[110] MnAs[ $11\bar{2}0$ ] $\parallel$ GaAs[ $1\bar{1}0$ ]	A <sub>1</sub>
	( $\bar{1}\bar{1}00$ )	MnAs[ $11\bar{2}0$ ] $\parallel$ GaAs[ $1\bar{1}0$ ] MnAs[0001] $\parallel$ GaAs[110]	B <sub>0</sub>
	( $\bar{1}\bar{1}01$ )	MnAs[ $11\bar{2}0$ ] $\parallel$ GaAs[ $1\bar{1}0$ ] MnAs[ $11\bar{2}0$ ] $\parallel$ GaAs[110]	B-B <sub>1</sub>
	( $11\bar{2}1$ )	MnAs[ $1\bar{1}02$ ] $\parallel$ GaAs[110] MnAs[0001] inclined//GaAs[110]	B*
	(110)	( $\bar{1}\bar{1}00$ )	MnAs[ $11\bar{2}0$ ] $\parallel$ GaAs[ $1\bar{1}0$ ] MnAs[0001] $\parallel$ GaAs[001]
(113)A	$\sim(\bar{1}\bar{1}00)$	MnAs[ $11\bar{2}0$ ] $\parallel$ GaAs[ $1\bar{1}0$ ] MnAs[0001] $\sim \parallel$ GaAs[ $33\bar{2}$ ], 4° tilted	
(111)A	( $\bar{1}\bar{1}01$ )	MnAs[ $11\bar{2}0$ ] $\parallel$ GaAs[ $1\bar{1}0$ ] $T_s < 300^\circ\text{C}$ MnAs[ $\bar{1}102$ ] $\parallel$ GaAs[ $\bar{1}\bar{1}2$ ]	
	(0001)	MnAs[ $11\bar{2}0$ ] $\parallel$ GaAs[ $1\bar{1}0$ ] $T_s 300\text{--}400^\circ\text{C}$ MnAs[ $\bar{1}100$ ] $\parallel$ GaAs[ $\bar{1}\bar{1}2$ ]	
(111)B	(0001)	MnAs[ $11\bar{2}0$ ] $\parallel$ GaAs[ $1\bar{1}0$ ] MnAs[ $\bar{1}100$ ] $\parallel$ GaAs[ $\bar{1}\bar{1}2$ ]	

Among all the types, MnAs/GaAs(001) is mostly investigated, especially the A<sub>0</sub> type in which  $[11\bar{2}0]\text{MnAs}/[110]\text{GaAs}$  and  $[0001]\text{MnAs}/[1\bar{1}0]\text{GaAs}$ <sup>17</sup>. The epitaxial relationship of A<sub>0</sub> type is illustrated in Fig. 2.2(b). There is also B<sub>0</sub>-type, in which  $[11\bar{2}0]\text{MnAs}/[1\bar{1}0]\text{GaAs}$  and  $[0001]\text{MnAs}/[110]\text{GaAs}$ <sup>17</sup>. Both of them have the same growth planes MnAs( $\bar{1}100$ ). In addition, the c axis ( $[0001]$  axis) of MnAs films can be tilted in some angles, as drafted in Fig. 2.2(c), to study if the tilted angle affects the properties of epitaxial films<sup>16,22</sup>.

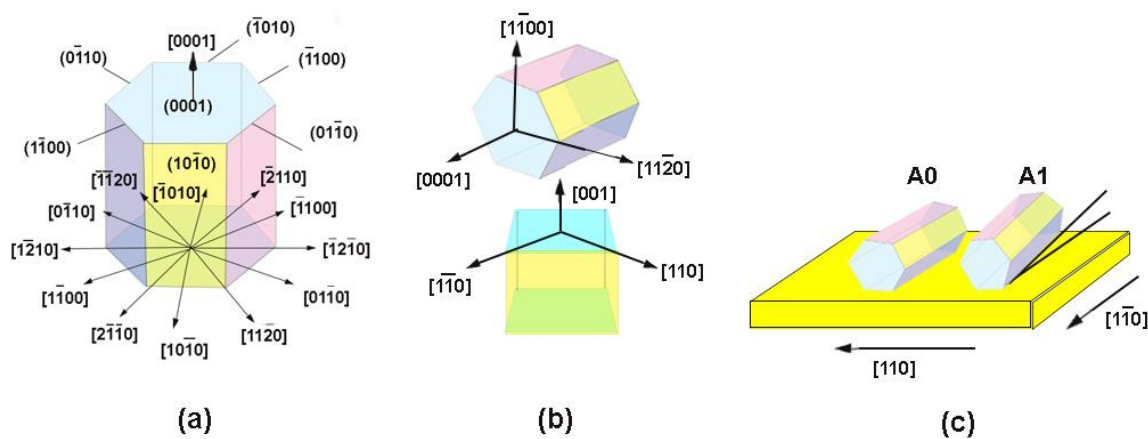


Fig. 2.2. (a) Crystal axes and planes of hexagonal structure; (b) epitaxial relationship between MnAs and GaAs in A<sub>0</sub>-type MnAs/GaAs(001) heterostructure; (c) a sketch diagram to show the difference between A<sub>0</sub> type and A<sub>1</sub> type.

In Fig 2.3 some illustrating HREM results from literature are presented. This will guide us to analyze our own samples in the chapter 4. We can see rather smooth interface between MnAs film and GaAs substrate in Fig. 2.3(a-d), indicating that high quality growth of MnAs films is available on all the four substrate orientations. Small dislocations at some positions of the interface must appear due to lattice mismatch. An example is shown in the dashed square in Fig. 2.3(a).

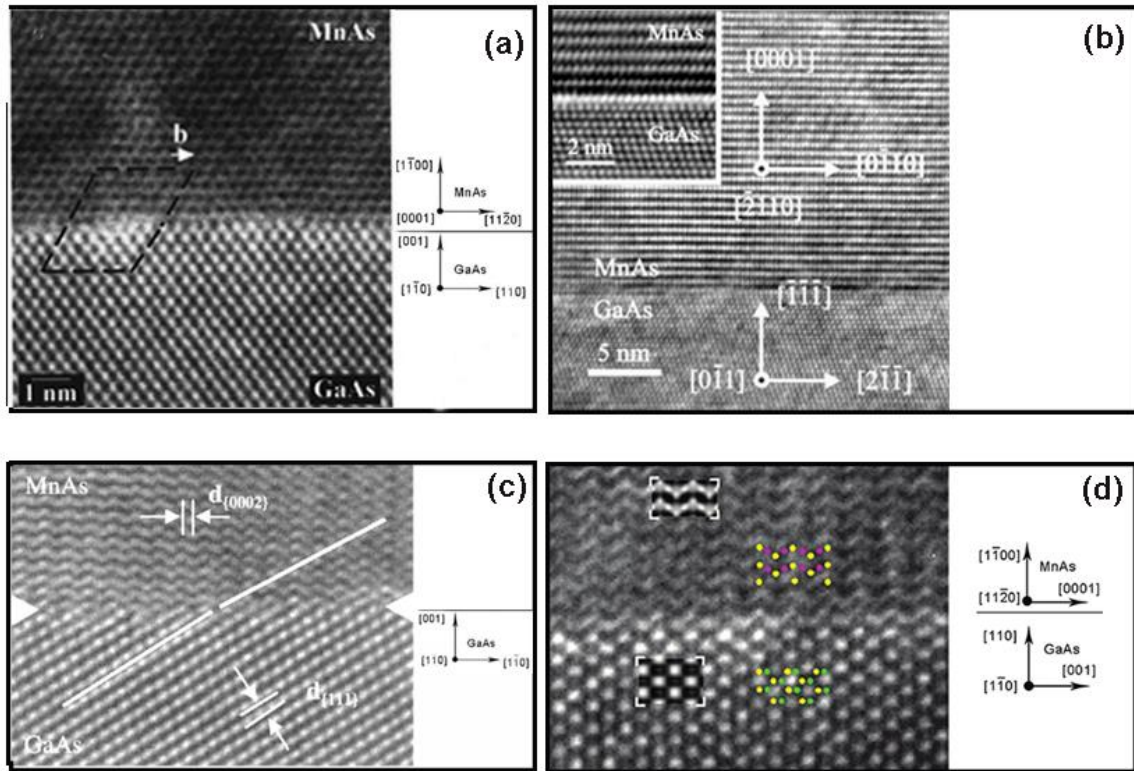


Fig. 2.3. HREM images of (a)  $MnAs/GaAs(001)^{17}$  type  $A_0$ , (b)  $MnAs/GaAs(111)B$ , (c)  $MnAs/GaAs(113)A^{19}$  and (d)  $MnAs/GaAs(110)^{18}$  from literature.

## 2. Micromagnetic Structure

As mentioned above, the epitaxial MnAs thin film undergoes a phase transition within a temperature range from around  $15^\circ\text{C}$  to  $45^\circ\text{C}$ , resulting in a coexistence of  $\alpha$  and  $\beta$  phase for at least  $30^\circ\text{C}$ , and thus exhibits unique topography and magnetic properties. To study these properties, it is critical to have a detailed understanding of the domain structure, as many important properties like magnetic stray field, magnetoresistance, and magnetization reversal are all governed by the micromagnetic structure<sup>23,24</sup>. In this section, the domain structures of MnAs films on GaAs(001) substrate observed with various techniques are presented. Then the temperature-dependent domain structure is demonstrated in particular. We only discuss the  $A_0$ -type MnAs/GaAs(001) in the following text, unless specified.

## 2.1 Domain structure observed with various techniques

Table 2.2. Observation of domain structure of MnAs/GaAs(001) in literature

Applied Technique	What has been observed	Reference
<b>Magnetic force microscopy (MFM)</b>	Basic domain types at RT	25
	Temperature-dependent domain structures	26,12
	Thickness-dependent domain structures	27
	Applied magnetic field-dependent domain structures	28,29,27
<b>X-ray magnetic circular dichroism photo emission electron microscopy (XMCD-PEEM)</b>	Basic domain types at RT	30,31,23
	Temperature-dependent domain structures	30
<b>Kerr microscopy</b>	Field-dependent domain structures	32
	Fast domain wall dynamics	33
<b>Elastic back scattering diffraction (EBSD)</b>	Mapping of crystallographic domains	34
<b>Time-resolved pump-probe scattering</b>	Dynamics of $\alpha$ and $\beta$ phase stripe domains	35

Various techniques have been applied to study the magnetic domain structures of MnAs/GaAs(001), as listed in table 2.2. The most commonly used techniques are magnetic force microscopy (MFM) and X-ray magnetic circular dichroism photo emission electron microscopy (XMCD-PEEM). In this section, investigations with these two techniques are mainly discussed.

MFM is a variant of the atomic force microscope (AFM) technique. It is capable of recording the magnetostatic force or vertical force gradient due to stray fields emanating from the sample by using a magnetic tip<sup>26</sup>. The advantage of this technique is that no special experimental condition and sample preparation are required, if the sample surface is what we want to study. But the interpretation of MFM images is not straightforward<sup>30</sup>, as it detects the stray field instead of directly mapping the domains. On the contrary, the complementary XMCD-PEEM technique in combination with low-energy electron microscopy (LEEM) and low-energy electron diffraction (LEED) provides sufficient lateral resolution and direct access to the surface magnetization<sup>36</sup>.



XMCD-PEEM is a surface-sensitive magnetic imaging technique that combines X-ray absorption spectroscopy and electron microscopy. The contrast formation originates from the difference in X-ray absorption coefficients depending on the relative orientation of photon helicity and magnetization. This technique has to be operated with synchrotron radiation.

Fig. 2.4 shows typical AFM/MFM and LEED/XMCD-PEEM images of MnAs film on GaAs(001) substrate around room temperature. It proves experimentally that ferromagnetic  $\alpha$ -MnAs and non-ferromagnetic  $\beta$ -MnAs stripes, perpendicular to MnAs[0001] direction, coexist in the form of bridges and grooves alternately as sketched in Fig. 2.4(a). The domain structures of  $\alpha$ -MnAs can be seen in Fig. 2.4 (c) and (f). Various kinds of domain patterns are classified into three basic types, which are characterized by the number of domains in a single ferromagnetic stripe along MnAs[11 $\bar{2}$ 0] direction. In Fig. 2.4(d), the meander-like contrast labeled I comes from the domains of alternating directions; the type II domain, characterized by two lines at the stripe edges and one in the middle with different contrast, shows head-on domain pattern; the type III domain, similar to type II, has three subdomains instead of two. Actually, more complex domain structures combining two or three basic domain types may appear. The magnetization directions of those domains are represented by arrows. In Fig. 2.4(f), the domain magnetization in XMCD-PEEM image is also interpreted, which is consistent with the interpretation of MFM images.

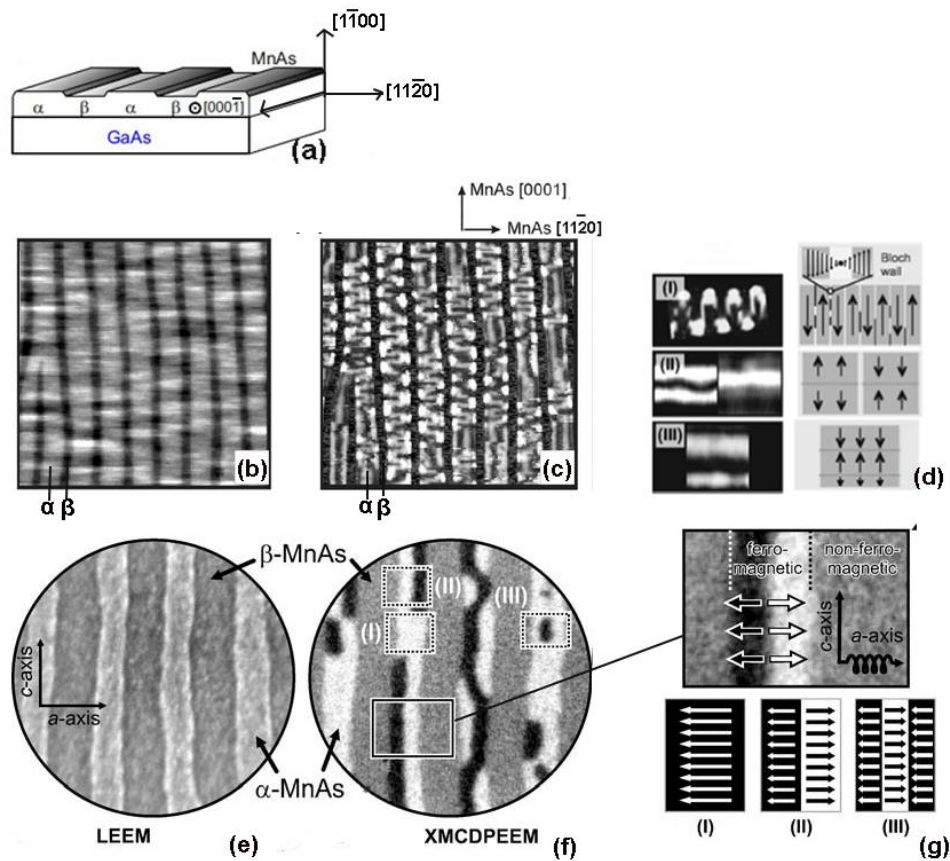


Fig. 2.4. (a) Schematic view of  $\alpha$ - $\beta$  stripes<sup>15</sup>; (b)<sup>8</sup> AFM image and (c)<sup>8</sup> MFM image of 180nm-thick MnAs film on GaAs(001) in exactly the same area ( $6\mu\text{m} \times 7\mu\text{m}$ ); (e)<sup>30</sup> LEEM image and (f)<sup>30</sup> XMCD-PEEM image of 180nm-thick MnAs film on GaAs(001) in exactly the same area (diameter  $7\mu\text{m}$ ); (d)<sup>25</sup> MFM images of three basic domain types I, II, III in ferromagnetic  $\alpha$ -MnAs and corresponding magnetization directions represented by arrows; (g)<sup>30</sup> magnetization directions represented by arrows in three basic domain types I, II, III in XMCD-PEEM image.

## 2.2 Temperature-dependent domain structure

The domain structures of MnAs films can vary with factors such as temperature, thickness and applied magnetic field (see table 2.2). It is important to study domain structures during a phase transition period, for a better understanding of the interplay between micromagnetic structures and micromagnetic properties. A sequence of XMCD-PEEM images in Fig. 2.5 recorded at increasing temperatures in the same sample area of

a 120-nm-thick MnAs film can give us a detailed instruction about the temperature dependent domain structure<sup>30</sup>. From 0°C to 23°C, the regular  $\beta$ -stripe structure is gradually formed, but only after 16°C slight change in the domain structure becomes apparent. The domain structure undergoes a dramatic change at 26°C. The opposite magnetization in intra-stripe regime starts to nucleate and above 28°C all type (I) domains transform into type (II) domains until the stripes become so narrow that they become single domain again. Finally the  $\alpha$ -stripes decompose into isolated ferromagnetic dots. It is found out that the magnetization decreases with increasing temperature not only due to thermal disorder but also due to the breaking of inter-stripe coupling resulted from increased distance between ferromagnetic stripes.

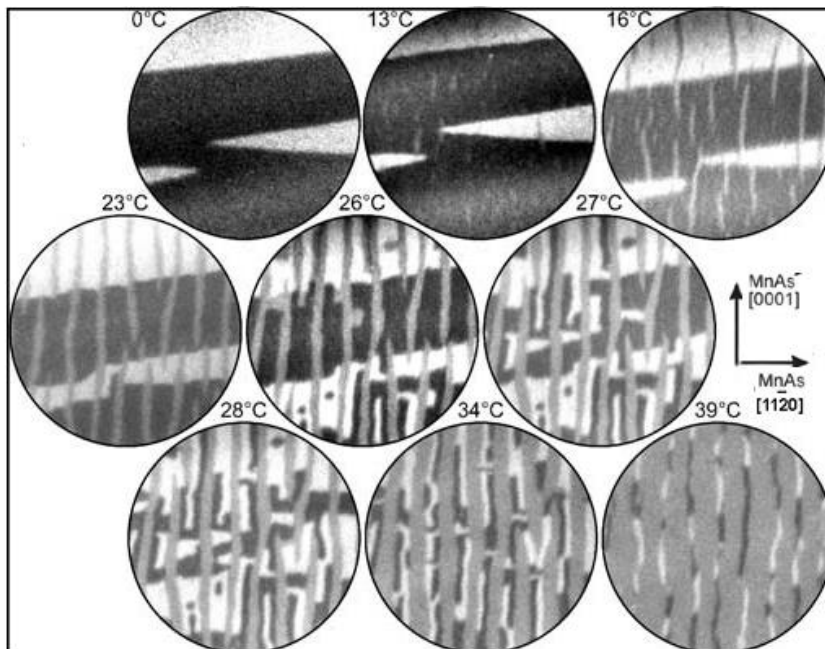


Fig. 2.5. <sup>30</sup>Stripe width-dependent domain patterns of a 120 nm-thick MnAs film on GaAs(001) imaged by XMCD-PEEM. Field-of-view diameter: 10  $\mu\text{m}$ .

In addition, it was found that the microstructures of MnAs film are different in heating and cooling process for a given temperature<sup>26,12</sup>, as shown in Fig. 2.6. At 30°C, for instance, the single domain appears in heating process, but there are much more complex domains in cooling process. It explains the temperature hysteresis of magnetization curve which will be discussed in the section 3.2.

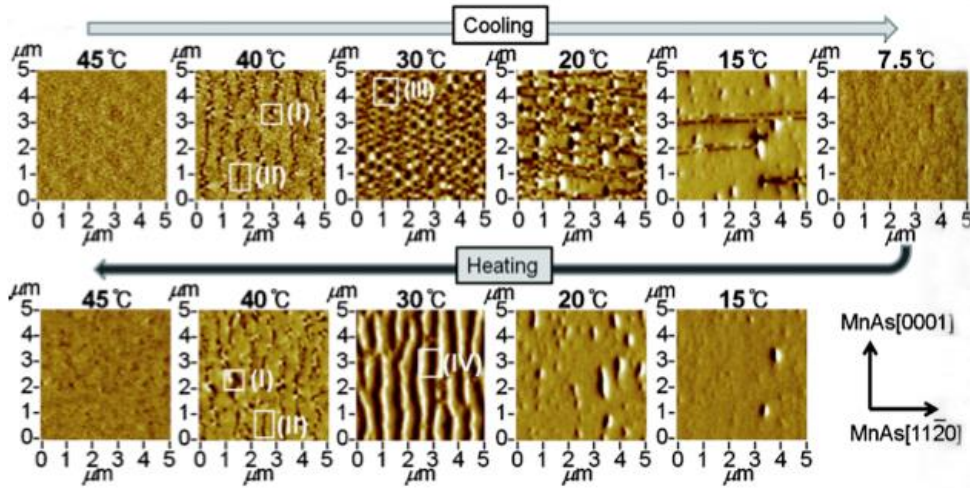


Fig. 2.6.  $^{12}\text{MFM}$  images of the 100nm-thick MnAs film on GaAs(001) at various temperatures.

### 2.3 Thickness-dependent domain structure

The thickness of the film is another factor that strongly influences the magnetic domain size and structure. Understanding the thickness-dependence magnetic domain structure of epitaxial MnAs films is necessary for designing spintronic devices.

The ferromagnetic stripe width  $w_\alpha$  and the non-ferromagnetic stripe width  $w_\beta$  are found to be a function of the film thickness. We define the  $\alpha$ - and  $\beta$ -phase contents as  $c_i = w_i/p$  with  $i = \alpha, \beta$ . The stripe period  $p = w_\alpha + w_\beta$  is a linear function of the film thickness  $t$  with  $p = 4.8 t$  at RT<sup>30</sup>. Manago *et al.* systematically investigated thickness-dependent topography and domain structures of MnAs films using MFM at RT<sup>27</sup>. The observed thickness range is from 5 to 500 nm, as seen in Fig. 2.7. MnAs films here are demagnetized and with zero applied magnetic field.

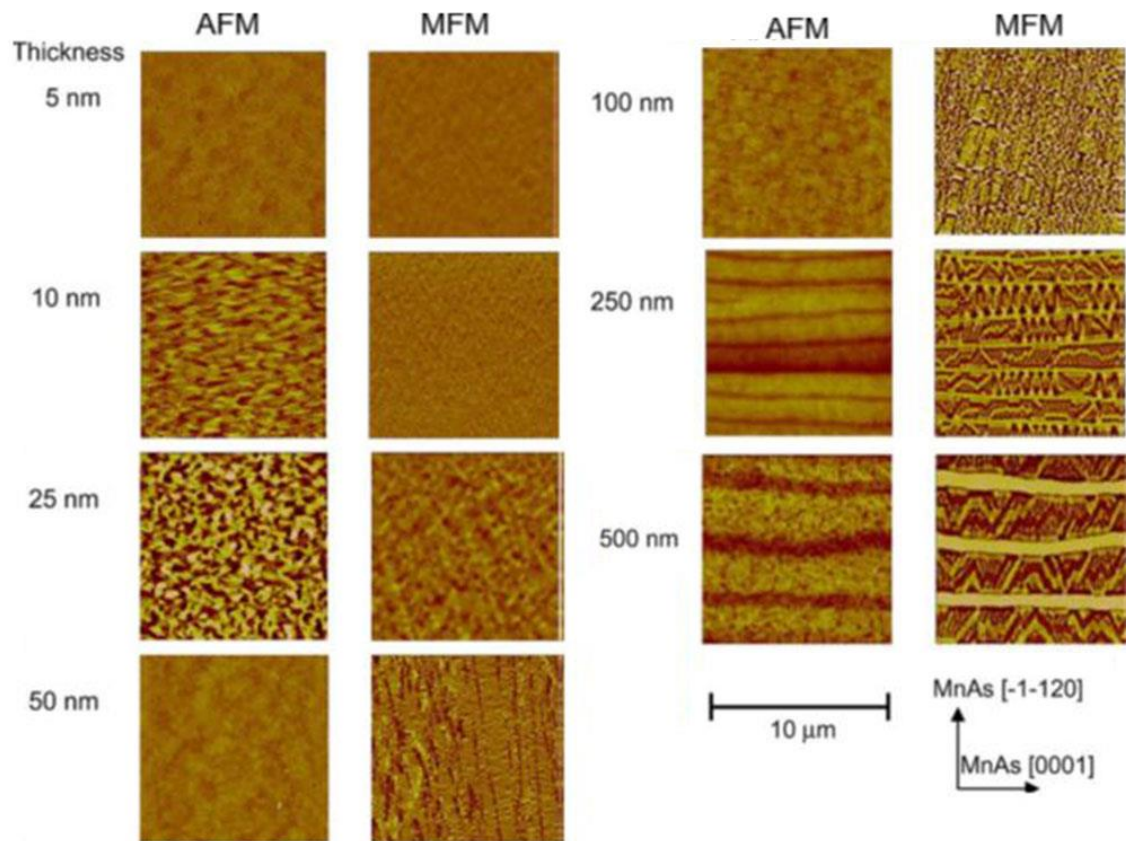


Fig. 2.7. <sup>27</sup> The change of topography and domain structure of demagnetized epitaxial MnAs film on GaAs (001) with increasing thickness from 5 nm to 500 nm, observed using AFM and MFM at RT.

For topographic images observed by the AFM, the random surface roughness once increases from 5 nm and then turns to decrease above the thickness of 50 nm. But in thicker films (>100 nm),  $\beta$ -MnAs appears as periodic linear grooves, and both the width and the period of grooves are larger in thicker films. For magnetic domain structures observed by the MFM, it is more complicated. There are no clear domain structure and domain wall until the thickness reaches 50 nm. In the 100-nm-thick film, a lot of rectangular domains appear, which are more likely the domain of type I as mentioned in Fig. 2.4. In the 250-nm-thick film, domains of type I are dominant but in the 500-nm-thick film, those of type I+III with zig-zag shape are dominant.

### 3. Magnetic anisotropy

As summarized above, epitaxial MnAs thin films on GaAs(001) substrate demonstrate micromagnetic structure depending on temperature, film thickness, applied field, etc. Correspondingly, the magnetization of MnAs films in different conditions has also been extensively studied, using Superconducting Quantum Interference Device (SQUID) technique in general, or XMCD technique as well as Cantilever Beam Magnetometer (CBM). Table 2.3 lists several published experimental results measured on MnAs films with different thickness and temperatures. All of the results in this table were acquired on the MnAs films magnetized along its easy axis. Actually MnAs films exhibits both in-plane and out-of-plane magnetic anisotropy, and the magnetization shows interesting temperature hysteresis. In the following text, the anisotropy and the temperature-dependent magnetization of A<sub>0</sub>-type MnAs thin films will be discussed in detail.

Table 2.3. Several experimental results of magnetic moment measured on MnAs/GaAs(001).

Technique	Sample thickness	Magnetic moment at ~280K	Magnetic moment at ~100K	Reference
SQUID	108 nm	~2.55 $\mu\text{B}/\text{Mn}$	~3.09 $\mu\text{B}/\text{Mn}$	37
	37nm	~2.18 $\mu\text{B}/\text{Mn}$	~2.91 $\mu\text{B}/\text{Mn}$	
	500nm	~1.82 $\mu\text{B}/\text{Mn}$		
	70nm	~2.18 $\mu\text{B}/\text{Mn}$		38
	100 nm	~2.90 $\mu\text{B}/\text{Mn}$	~3.5 $\mu\text{B}/\text{Mn}$	39
XMCD	ml/ms $\approx$ 0.03	~5 $\mu\text{B}/\text{Mn}$ ml/ms $\approx$ 0.025		
Cantilever Beam Magnetometer (CBM)	60nm	~2.37 $\mu\text{B}/\text{Mn}$		40

\*The SQUID results are unified from  $\text{emu}/\text{cm}^3$  to  $\mu\text{B}/\text{Mn}$ , and in the calculation the tiny contribution of Arsenic atom to the magnetic moment is ignored. MnAs is in its ferromagnetic phase at the temperature of both 100K and 280K.

### 3.1 In plane and out-of-plane anisotropy

It is known that bulk MnAs has a magnetocrystalline anisotropy with an easy plane of MnAs(0001) without any preferred magnetization direction in the easy plane. However, epitaxial MnAs film exhibits a different behavior. It not only presents a strong in-plane uniaxial magnetic anisotropy with the easy axis MnAs[11 $\bar{2}$ 0] and hard axis [0001], but also presents out-of-plane magnetic anisotropy with intermediate axis  $[\bar{1}100]$ <sup>41,42,38</sup>. Referring to Fig. 2.4(a) or the inset of Fig. 2.8, “in-plane” means the film growth plane MnAs( $\bar{1}100$ ) and “out-of-plane” here means the plane perpendicular to the growth plane. Experimental results acquired by SQUID technique in Fig. 2.8 verifies the strong in-plane magnetic anisotropy, given that much higher magnetic field is required to achieve magnetic saturation along hard axis MnAs[0001] (c axis) than easy axis MnAs[11 $\bar{2}$ 0] (a axis)<sup>38</sup>. The saturation magnetization field of intermediate axis MnAs[ $\bar{1}100$ ] (b axis) is between that of easy and hard axis, verifying the out-of-plane anisotropy.

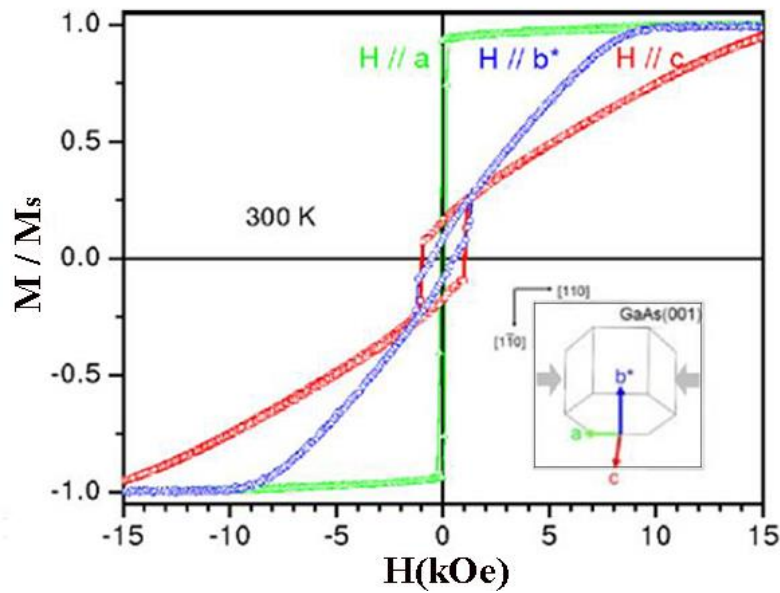


Fig. 2.8.<sup>38</sup> Hysteresis loops measured at RT with magnetic fields applied along the distinct crystallographic directions for 70nm-thick MnAs/GaAs(001), by SQUID. Insets identify the directions along which the magnetic fields are applied relative to the hexagonal cell of the crystal structure. a//MnAs[11 $\bar{2}$ 0], b//MnAs[ $\bar{1}100$ ], c//MnAs[0001].

### 3.2 Temperature-dependent magnetization

Hysteresis loops of MnAs films vary drastically with temperature. Fig. 2.9 demonstrates the curve magnetization ( $M$ ) versus magnetic field ( $H$ ) within a wide range of temperature. Given the magnetization along both easy axis and hard axis, we find the saturation magnetization  $M_s$  becomes lower with increasing temperature<sup>39</sup>, which is similarly indicated in Fig. 2.10. However, the saturation magnetization of MnAs films can be different even at the same temperature point. Fig. 2.10 shows  $M_s(T)$  curves measured on a 108-nm-thick MnAs/GaAs (001) film<sup>37</sup>. Under zero magnetic field, cooling and heating branches of  $M_s(T)$  curves reveal a thermal hysteresis. What is behind the thermal hysteresis? In region A of the heating branch, only  $\alpha$ -MnAs exists and the change of magnetization with temperature is mainly due to thermal fluctuation of the magnetic moments. In region B, the formation of  $\beta$ -MnAs starts, splitting the ferromagnetic  $\alpha$ -MnAs into separate parts. But there still exists ferromagnetic order in  $\alpha$ -MnAs stripes across  $\beta$ -MnAs ones. The ferromagnetic interaction of  $\alpha$ -MnAs stripes is then largely reduced in region C due to the broader  $\beta$ -MnAs stripes. In region D after 316K, the magnetization finally becomes zero. Compared to the heating branch, the magnetization begins to largely decrease at lower temperature in the cooling branch. It corresponds to the different processes of domain evolution during heating and cooling as shown in Fig. 2.6. In addition, thermal hysteresis can be nearly completely lifted when the external applied magnetic field is high enough, because nearly all magnetic moments become oriented along the applied field in this situation.

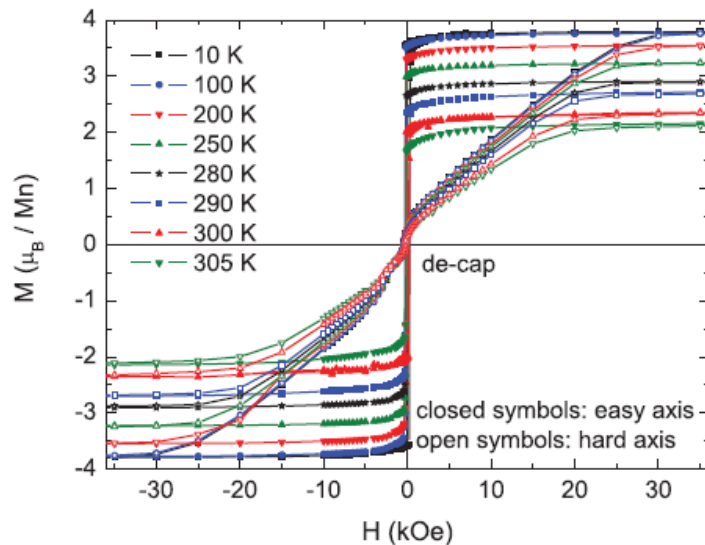




Fig. 2.9. Magnetization ( $M$ ) versus field ( $H$ ) at different temperatures, in the range 10–305 K, for the de-cap sample, with filled symbols corresponding to a field applied along the easy axis ( $[11\bar{2}0]$  direction) of magnetization and open symbols to a field applied along the hard axis ( $[0001]$  direction) of magnetization<sup>39</sup>.

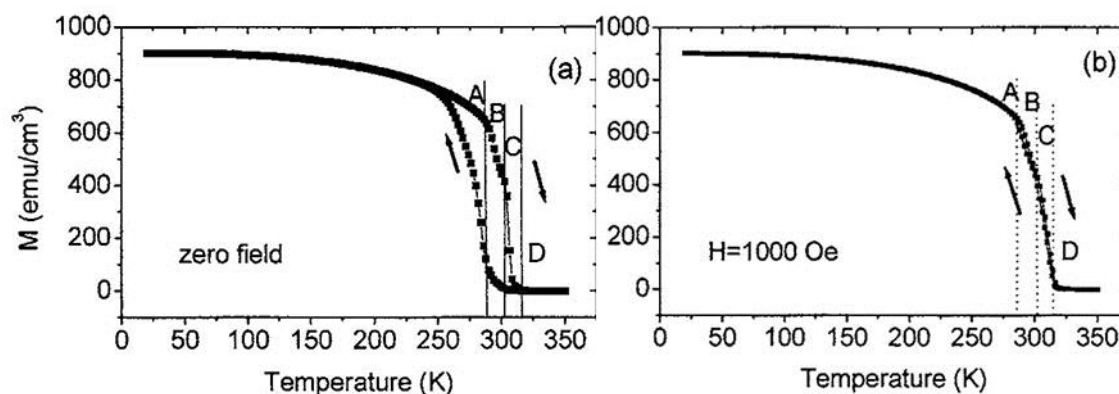


Fig. 2.10. Temperature dependence of (a) the saturation magnetization of a 108-nm-thick MnAs/GaAs(001) film measured without external field, and (b) in a field of 1000 Oe. The letters A, B, C, and D denote temperature regions with characteristic differences in the magnetic microstructure<sup>37</sup>.

### 3.3 Thickness-dependent magnetization

The magnetization of MnAs films also changes with the film thickness, corresponding to the thickness-dependent domain structure in section 2.3 of this chapter. As shown in Fig. 2.11, a square loop is observed for a 108-nm-thick film, while with increasing film thickness, the loop inclines gradually into a rounded shape<sup>37</sup>. The tendency shown in Fig. 2.11 is consistent with the results of many other studies<sup>43,19,44</sup>. Moreover, a characteristic change of the saturation magnetization  $M_s$  with the film thickness is of interest<sup>43,37</sup>. In Fig. 2.12,  $M_s$  increases up to a special thickness  $t^*$  and decreases after that. This behavior is actually observed for differently orientated MnAs films on GaAs substrate, e.g. MnAs/GaAs(001), MnAs/GaAs(113)A and MnAs/GaAs(111)B, which have at least one  $[11\bar{2}0]$  direction lying in the interface plane.

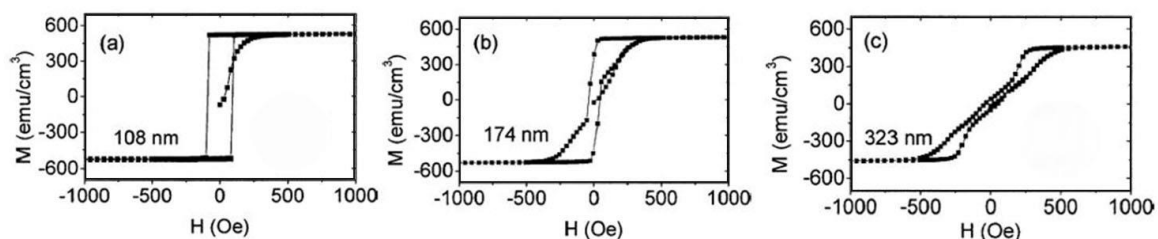


Fig. 2.11.<sup>37</sup> Magnetic hysteresis loops of MnAs thin films of (a) 108nm-thick; (b) 174nm-thick; (c) 323nm-thick, at RT.

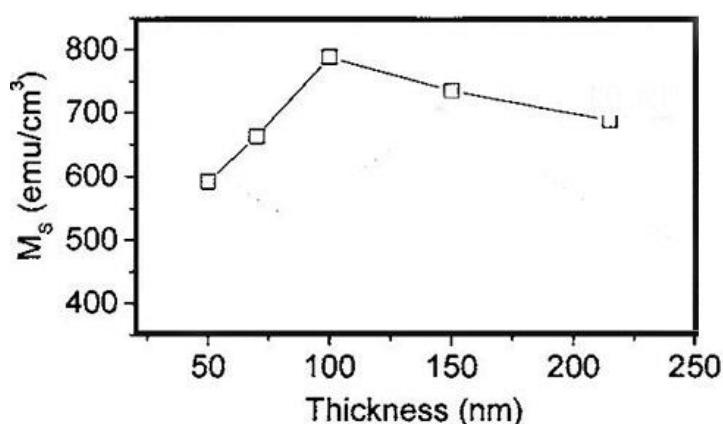


Fig. 2.12.<sup>37</sup> Thickness dependence of the saturation magnetization of MnAs films on GaAs(001) substrate, measured by SQUID at RT.

In conclusion, both structural and magnetic properties of epitaxial MnAs thin films on GaAs are summarized in this chapter. At first, different types of MnAs/GaAs heterostructures with various growth orientations in literature are gathered, and their epitaxial relationships between the MnAs layer and GaAs substrate are illustrated and compared. Regarding the magnetic properties, we summarize the research results of the micromagnetic domain structure and magnetization characteristics of MnAs films on GaAs(001) in recent decades. In particular, the dependence of the domain structure and magnetization on the temperature and thickness is discussed in detail. This chapter provides rich information of MnAs thin films, which will be used when discussing the experimental results in chapter IV.

## Bibliography

1. Heusler, F. Über Manganbronze und über die Synthese magnetisierbarer Legierungen aus unmagnetischen Metallen. *Angew. Chem.* **17**, 260–264 (1904).
2. Hilpert, S. & Dieckmann, T. Arsenides. I. Iron and Manganese Arsenides. *Ber Dtsch Chem Ges* **44**, 2378–2385 (1911).
3. Guillaud, C. Les points de transformation des composés définis MnAs, MnBi en relation avec un mécanisme probable d'antiferromagnétisme. *J Phys Radium* **12**, 223–227 (1951).
4. Niranjana, M. K., Sahu, B. R. & Kleinman, L. Density functional determination of the magnetic state of  $\beta$ -MnAs. *Phys. Rev. B* **70**, 180406 (2004).
5. Ney, A. *et al.* Nature of the magnetic and structural phase transition in MnAs/GaAs(001). *Phys. Rev. B* **69**, 081306 (2004).
6. Wilson, R. H. & Kasper, J. S. The crystal structure of MnAs above 40°C. *Acta Crystallogr.* **17**, 95–101 (1964).
7. Ramsteiner, M. *et al.* Electrical spin injection from ferromagnetic MnAs metal layers into GaAs. *Phys. Rev. B* **66**, 081304 (2002).
8. Däweritz, L. *et al.* Structural and magnetic order in MnAs films grown by molecular beam epitaxy on GaAs for spin injection. *J. Cryst. Growth* **251**, 297–302 (2003).
9. Sugahara, S. & Tanaka, M. Tunneling magnetoresistance in fully epitaxial MnAs/AlAs/MnAs ferromagnetic tunnel junctions grown on vicinal GaAs(111)B substrates. *Appl. Phys. Lett.* **80**, 1969–1971 (2002).
10. Garcia, V. *et al.* Resonant tunneling magnetoresistance in MnAs/III-V/MnAs junctions. *Phys. Rev. B* **72**, 081303 (2005).
11. Pampuch, C. *et al.* Magnetologic with  $\alpha$ -MnAs Thin Films. *Phys. Rev. Lett.* **91**, 147203 (2003).
12. Kim, J., Akinaga, H. & Kim, J. Observation of magnetic domain structures in epitaxial MnAs film on GaAs(001) with temperature hysteresis. *Appl. Phys. Lett.* **98**, 102511 (2011).
13. Däweritz, L. Interplay of stress and magnetic properties in epitaxial MnAs films. *Rep. Prog. Phys.* **69**, 2581 (2006).
14. Rungger, I. & Sanvito, S. Ab initio study of the magnetostructural properties of MnAs. *Phys. Rev. B* **74**, 024429 (2006).

15. Breitwieser, R. *et al.* Phase transition and surface morphology of MnAs/GaAs(001) studied with in situ variable-temperature scanning tunneling microscopy. *Phys. Rev. B* **80**, 045403 (2009).
16. Tanaka, M. *et al.* Epitaxial orientation and magnetic properties of MnAs thin films grown on (001) GaAs: Template effects. *Appl. Phys. Lett.* **65**, 1964–1966 (1994).
17. Schippan, F., Trampert, A., Däweritz, L. & Ploog, K. H. Kinetics of MnAs growth on GaAs(001) and interface structure. *J. Vac. Sci. Technol. B* **17**, 1716–1721 (1999).
18. Wan, Q. & Trampert, A. Atomic Configuration of the MnAs/GaAs (110) Interface Analyzed by High-Resolution Electron Microscopy. *J. Phys. Chem. C* **115**, 529–533 (2011).
19. Däweritz, L. *et al.* Thickness dependence of the magnetic properties of MnAs films on GaAs(001) and GaAs(113)A: Role of a natural array of ferromagnetic stripes. *J. Appl. Phys.* **96**, 5056–5062 (2004).
20. Engel-Herbert, R., Hesjedal, T., Schaadt, D. M., Däweritz, L. & Ploog, K. H. Micromagnetic properties of MnAs(0001)/GaAs(111) epitaxial films. *Appl. Phys. Lett.* **88**, 052505 (2006).
21. Friedland, K.-J., Kästner, M. & Däweritz, L. Ordinary Hall effect in MBE-grown MnAs films grown on GaAs(001) and GaAs(111)B. *Phys. Rev. B* **67**, 113301 (2003).
22. Iikawa, F. *et al.* Effect of MnAs/GaAs(001) film accommodations on the phase-transition temperature. *Appl. Phys. Lett.* **85**, 2250–2252 (2004).
23. Engel-Herbert, R., Hesjedal, T. & Schaadt, D. M. Three-dimensional micromagnetic domain structure of MnAs films on GaAs(001): Experimental imaging and simulations. *Phys. Rev. B* **75**, 094430 (2007).
24. Engel-Herbert, R. & Hesjedal, T. Investigation of slanted and V-shaped domain walls in MnAs films. *J. Appl. Phys.* **105**, 07D504 (2009).
25. Engel-Herbert, R. *et al.* Understanding the submicron domain structure of MnAs thin films on GaAs(001): Magnetic force microscopy measurements and simulations. *Appl. Phys. Lett.* **84**, 1132–1134 (2004).
26. Mohanty, J. *et al.* Variable-temperature micromagnetic study of epitaxially grown MnAs films on GaAs(001). *Appl. Phys. A* **77**, 739–742 (2003).
27. Manago, T., Kuramochi, H. & Akinaga, H. Thickness dependence of magnetic domains of MnAs films. *Surf. Sci.* **600**, 4155–4159 (2006).
28. Engel-Herbert, R., Hesjedal, T., Mohanty, J., Schaadt, D. M. & Ploog, K. H. Field dependence of micromagnetic domain patterns in MnAs films. *J. Appl. Phys.* **98**, 063909 (2005).
29. Engel-Herbert, R., Hesjedal, T., Mohanty, J., Schaadt, D. M. & Ploog, K. H. Magnetization reversal in MnAs films: Magnetic force microscopy, SQUID magnetometry, and micromagnetic simulations. *Phys. Rev. B* **73**, 104441 (2006).

30. Engel-Herbert, R. *et al.* Investigation of magnetically coupled ferromagnetic stripe arrays. *Appl. Phys. A* **84**, 231–236 (2006).
31. Engel-Herbert, R. *et al.* The nature of charged zig-zag domains in MnAs thin films. *J. Magn. Magn. Mater.* **305**, 457–463 (2006).
32. Manago, T. & Akinaga, H. Ladder-type magnetic structures in MnAs epitaxial films—measurements and micromagnetic simulations. *J. Appl. Phys.* **104**, 093901 (2008).
33. Tortarolo, M. *et al.* Fast domain wall dynamics in MnAs/GaAs films. *Appl. Phys. Lett.* **101**, 072408 (2012).
34. Takagaki, Y. *et al.* Distribution of structural domains in MnAs layers grown on GaAs substrates. *J. Appl. Phys.* **108**, 123510 (2010).
35. Sacchi, M. *et al.* Time resolved pump-probe scattering in MnAs/GaAs(001): A look into the dynamics of  $\alpha$ - $\beta$  stripe domains. *Appl. Phys. Lett.* **100**, 211905–211905–4 (2012).
36. Bauer, E. *et al.* Low-energy electron microscopy/x-ray magnetic circular dichroism photoemission electron microscopy study of epitaxial MnAs on GaAs. *J. Vac. Sci. Technol. B* **20**, 2539–2542 (2002).
37. Däweritz, L. *et al.* Tailoring of the structural and magnetic properties of MnAs films grown on GaAs—Strain and annealing effects. *J. Vac. Sci. Technol. B* **23**, 1759–1768 (2005).
38. Paes, V. Z. C., Graff, I. L., Varalda, J., Etgens, V. H. & Mosca, D. H. The role of magnetoelastic and magnetostrictive energies in the magnetization process of MnAs/GaAs epilayers. *J. Phys. Condens. Matter* **25**, 046003 (2013).
39. Wikberg, J. M. *et al.* Magnetocrystalline anisotropy and uniaxiality of MnAs/GaAs(100) films. *Phys. Rev. B* **83**, 024417 (2011).
40. Das, A. K. *et al.* Ferromagnetism of MnAs Studied by Heteroepitaxial Films on GaAs(001). *Phys. Rev. Lett.* **91**, 087203 (2003).
41. Schippan, F. *et al.* Magnetic structure of epitaxially grown MnAs on GaAs(001). *J. Appl. Phys.* **88**, 2766–2770 (2000).
42. Ney, A. *et al.* Magnetic out-of-plane component in MnAs/GaAs(001). *Appl. Phys. Lett.* **83**, 2850–2852 (2003).
43. Toliński, T. *et al.* Magnetic coupling and exchange stiffness in striped MnAs films. *EPL Europhys. Lett.* **68**, 726 (2004).
44. Ryu, K.-S. *et al.* Origin of uniaxial magnetic anisotropy in epitaxial MnAs film on GaAs(001) substrate. *Appl. Phys. Lett.* **92**, 082503 (2008).

## Chapter III

### DyFe<sub>2</sub>/YFe<sub>2</sub> Laves Phase Superlattices

Exchange-coupled systems, composed of two magnetic materials that interact with each other at the interface, are found to demonstrate largely different magnetic behaviors compared with each component. The exchange spring magnets consisting of a hard and a soft magnetic material emerge as exchange-coupled systems. When a suitable external field is applied, the magnetization of the soft material is pinned to the magnetization of the hard material at the interfaces while twisting towards the applied field in the bulk. But the twisted moments in soft material will rotate back into alignment with that of the hard material, when the applied magnetic field is removed. That is why such magnets are characterized by enhanced remanent magnetization and reversible demagnetization curves<sup>1</sup>. This resembles a mechanical torsion spring, seen in Fig. 3.1, thus comes the name “exchange spring”<sup>2</sup>.

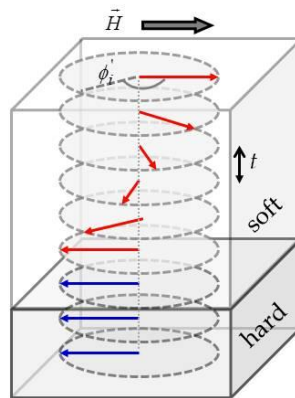


Fig. 3.1. Schematic illustration of exchange spring magnets.

Exchange spring magnets are promising candidates for a set of applications, e.g. permanent magnets, data storage media, micro electromechanical system (MEMS). They are initially proposed to increase the maximum energy product of permanent magnets<sup>3</sup>. It was predicted that a giant energy product of 120 MGOe (about three times that of

commercially available permanent magnets) is possible in superlattice structures consisting of aligned hard-magnet layers that are exchange coupled to soft layers with high magnetization<sup>1</sup>. Sequent studies reveal that the antiferromagnetical coupled exchange spring systems can be used for perpendicular recording media because they are thermally stable and easy to write<sup>4</sup>. They can also be applied to magnetic MEMS devices as micro-sensors and micro-actuators.

The materials that exhibit magnetic exchange spring behavior therefore attract much attention. REFe<sub>2</sub>/RE\*Fe<sub>2</sub> superlattice, in which RE is a highly anisotropic rare-earth element (Dy, Tb, Sm, Er, Nd) and RE\* is a nonmagnetic rare-earth element (Y, La, Lu) or an almost isotropic metal such as Gd<sup>5</sup>, is of great interest. Differing from the other polycrystalline or amorphous exchange spring systems, the REFe<sub>2</sub> Laves Phase superlattice is single-crystal. That makes it a model system to study magnetic springs, exchange bias phenomena and magnetization reversal process in exchange coupled systems<sup>6</sup>.

This summary focuses on DyFe<sub>2</sub>/YFe<sub>2</sub> superlattice, which is REFe<sub>2</sub> Laves Phase superlattice. Its microstructure is described in the section 1, followed by its magnetic properties such as exchange spring effect in the section 2.

## 1. Crystallographic structure

Laves phases form a large group of intermetallic phases. They have the composition AB<sub>2</sub>, and crystallize either in a cubic MgCu<sub>2</sub> (C15), or an hexagonal MgZn<sub>2</sub> (C14) or an hexagonal MgNi<sub>2</sub> (C36) structure. In general, the A atoms are ordered as in diamond or a similar structure, and the B atoms are arranged in tetrahedrons. Fig. 3.2 (a) shows the conventional unit cell of the C15 Laves phase.

Both bulk DyFe<sub>2</sub> and YFe<sub>2</sub> compounds crystallize in the C15 Laves Phase structure, made up of a face centered cubic diamond lattice of RE atoms and tetrahedral of iron atoms. Eight REFe<sub>2</sub> units are contained in the cubic unit cell. The two compounds also have close bulk lattice parameters of 0.732nm and 0.763nm respectively at room temperature, making it possible to grow superlattices with the two materials by MBE. Fig. 3.2(b) is a schematic view of the epitaxial DyFe<sub>2</sub>/YFe<sub>2</sub> superlattice sample. Generally the growth plane of this superlattice is DyFe<sub>2</sub>(110). A (11 $\bar{2}$ 0) orientated sapphire substrate is covered by (110) niobium as a chemical buffer, followed by the

deposition of an iron seed layer and then the alternate growth of (110)  $DyFe_2$  and (110) $YFe_2$  layers. The epitaxial relationship of the superlattice and substrate is  $[11\bar{2}0]$   $Al_2O_3//[110]DyFe_2$ ,  $[0001]$  Sapphire// $[1\bar{1}\bar{1}]DyFe_2$  and  $[\bar{1}100]$  Sapphire// $[1\bar{1}\bar{2}]DyFe_2$ . All the  $DyFe_2$  layers in the superlattice must be with the same thickness  $t_1$ , so as the  $YFe_2$  layers  $t_2$  as shown in Fig. 3.3, while the thickness ratio  $t_1/t_2$  of  $DyFe_2$  and  $YFe_2$  layers can be adjusted<sup>7</sup>. Fig. 3.3 gives two TEM images of a  $DyFe_2/YFe_2$  superlattice along the  $DyFe_2[\bar{1}10]$  zone axis observed at two different magnifications.

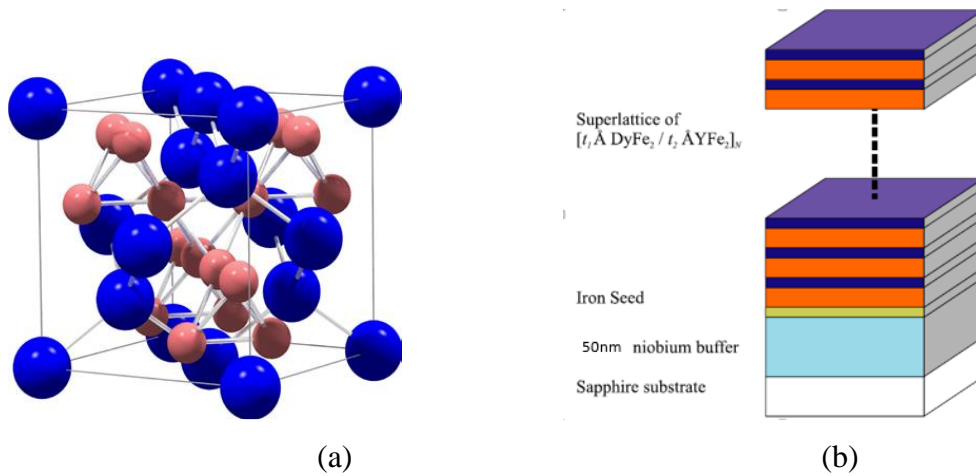


Fig. 3.2. <sup>8,9</sup>(a) The conventional unit cell of the C15 Laves phases. If it is  $DyFe_2$  or  $YFe_2$ , the large spheres represent dysprosium or yttrium atoms and the small spheres represent iron atoms. They crystallize in the face-centered cubic structure  $O7h$  ( $Fd.3m$ ) with 24 atoms per cubic unit cell. (b) A schematic view of a Laves phase superlattice sample grown by MBE.

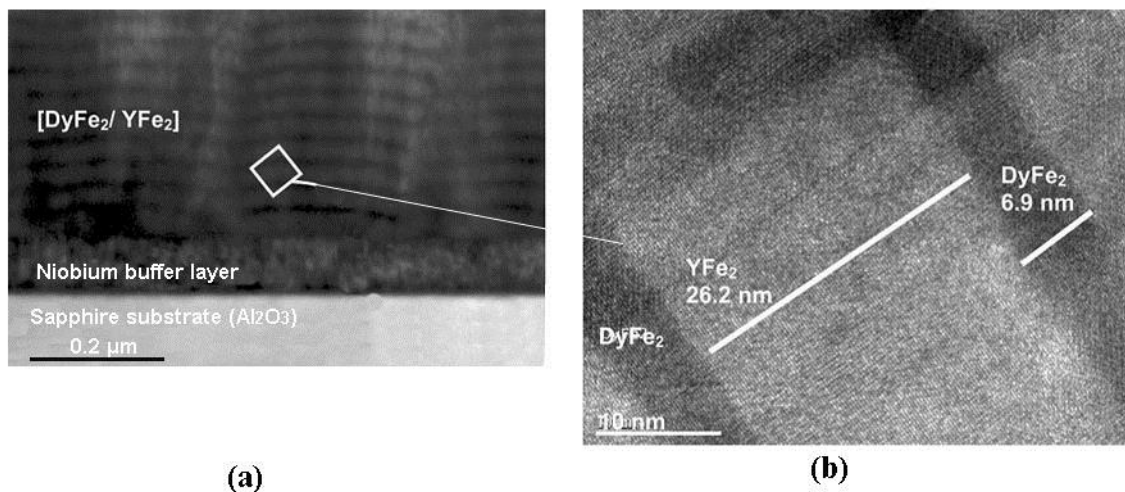


Fig. 3.3. <sup>7</sup>TEM images observed at two different magnifications for the  $DyFe_2/YFe_2$  superlattice with a 33.1 nm bilayer repeat distance along the  $[110]$  growth direction.



## 2. Magnetic properties

As previously mentioned, the DyFe<sub>2</sub>/YFe<sub>2</sub> superlattice is a model system to study magnetic springs, exchange bias phenomena and magnetization reversal process in exchange coupled systems. These magnetic properties can be investigated with various techniques, as summarized in Table 3.1. In this section 2, after the moment coupling in DyFe<sub>2</sub>/YFe<sub>2</sub> system is introduced, several important magnetic phenomena will be explained in detail.

Table 3.1. Summary of research on DyFe<sub>2</sub>/YFe<sub>2</sub> multi-layers in recent years

Temperature range	Applied magnetic field range	What to measure	technique	Reference
10K-300k	-8T~8T	Magnetization	SQUID and XMCD	5,10,11,6,12,13,14,15,7,16,17
12K-300k	-8T~8T	angle of moment /Magnetization	Neutron reflectometry and SQUID	18,8
<b>12K-300k</b>	-12T~12T	Magnetization	Vibrating Sample Magnetometer	19,20,21,22, 23,24,25,26,8
---	---	Room-temperature magneto-optic Kerr effect (MOKE)	MOKE	27
---	---	Magnetization	Monte Carlo or OOMMF Simulation	28,29,30

### 2.1 The exchange coupling in DyFe<sub>2</sub>/YFe<sub>2</sub> system

DyFe<sub>2</sub> is a ferrimagnet, in which Dy and Fe moments have an antiparallel coupling and the net magnetization is along the dominant Dy moment direction, as sketched in Fig. 3.4. It is a hard magnetic material. The easy axis of epitaxial DyFe<sub>2</sub> thin layers grown on (110) planes is temperature dependent, though the easy axis of bulk DyFe<sub>2</sub> always stays along <001> for all temperatures<sup>31,32</sup>. It is because the magnetic anisotropy is due to both crystal field interaction and lattice strain elastic interaction, and the contribution of elastic interaction increases with rising temperature, thus rotates the direction of the easy axis. YFe<sub>2</sub> is also a ferrimagnet, but the Y site has only a small induced moment as seen in Fig. 3.4, so that the anisotropy is very weak. Therefore YFe<sub>2</sub> can be considered as a soft

magnetic material. The coercivity of DyFe<sub>2</sub>/YFe<sub>2</sub> superlattice is mainly derived from the DyFe<sub>2</sub> hard phase.

The magnetic coupling is complex in this hard/soft system, including within the Laves phases and at the interface of the two Laves phases. It is known that in Laves phases, there are three magnetic interactions that couple the moments of the rare-earth and transition metal sites<sup>7</sup>. The three interactions in DyFe<sub>2</sub> are described below. For better demonstration, Fig. 3.4 gives a schematic view of the equilibrium magnetic configuration in a DyFe<sub>2</sub>/YFe<sub>2</sub>/DyFe<sub>2</sub> stacking.

(1) the transition-metal – transition-metal interaction ( $J_{Fe-Fe}$ ). Those intermetallic compounds like DyFe<sub>2</sub> and YFe<sub>2</sub> have high Curie temperature, largely due to the strong Fe-Fe exchange interaction.

(2) the rare-earth – transition-metal interaction ( $J_{Dy-Fe}$ ). Because of the effective coupling of the 3d electrons in the transition metal with the 4f electrons of the rare-earth metal, the rare-earth and transition metal moments are antiparallely aligned. This coupling is weaker than the Fe-Fe one.

(3) the rare-earth – rare-earth interaction ( $J_{Dy-Dy}$ ). The coupling between rare-earth moments is by far the weakest interaction, due to the small overlap of the 4f wavefunctions.

Strong Fe-Fe interaction, weak rare-earth – rare-earth interaction, and antiparallel alignment between rare-earth and Fe moment result in that the iron moments in DyFe<sub>2</sub> layer and YFe<sub>2</sub> layer at the interface tend to align parallel to each other, as shown in Fig. 3.4. That means the interaction at the DyFe<sub>2</sub>/YFe<sub>2</sub> interface is mainly the interaction between iron spins. Therefore the net moments in DyFe<sub>2</sub> layer and YFe<sub>2</sub> layer are antiparallel, saying antiferromagnetical coupled (some other spring magnets multilayers are ferromagnetically coupled like Sm/Co-Co layer). The net magnetization of the whole superlattice depends on the relative thickness of DyFe<sub>2</sub> and YFe<sub>2</sub>.

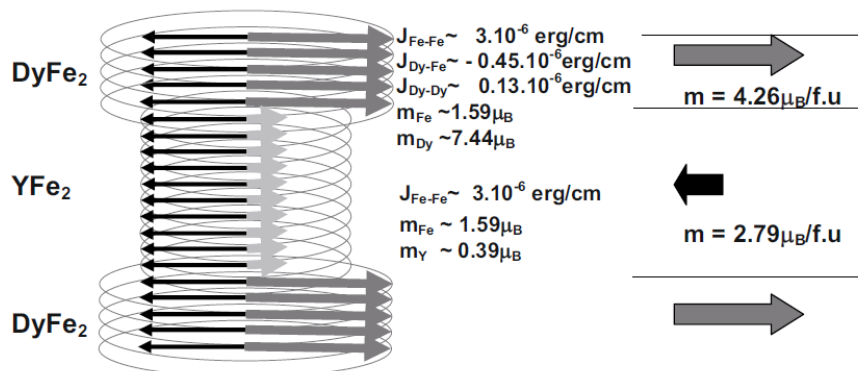


Fig. 3.4. <sup>7</sup>Schematic view of the equilibrium magnetic configuration in a  $DyFe_2/YFe_2/DyFe_2$  stacking. Black arrows represent Fe moments, while gray arrows represent Dy (dark gray) and Y (light gray) moments. The  $J$  values are the exchange interaction constants<sup>8</sup>; the values of the magnetic moments are those reported at 300 K.

## 2.2 Magnetic exchange springs and associated phenomena

### 2.2.1 Three different reversal processes

Several techniques have been applied to reveal the complicated reversal process of  $DyFe_2/YFe_2$  superlattice such as vibrating sample magnetometer (VSM)<sup>19,20,21,22,23,24,25,26</sup>, SQUID and X-ray magnetic chiral dichroism (XMCD)<sup>5,10,11,6,12,13,14,15,7,16,17</sup>, magneto-optic Kerr effect<sup>27</sup>, neutron reflectometry<sup>18,8</sup>. A group in Institut Jean Lamour has a series of papers working on  $DyFe_2/YFe_2$  superlattice with XMCD technique. By monitoring the XMCD signal at the Dy- $L_3$  (2d-5d transitions) and Y- $L_3$  (2p-4d transitions) absorption edges as a function of applied magnetic field, element-specific hysteresis loops are obtained. In this way, the technique isolates the magnetic response of each chemical constituents in the sample, providing a deep sight into the mechanism<sup>7</sup>.

As introduced in the beginning of the summary, the simplest model to describe the magnetization reversal in such hard/soft coupled systems is the “exchange springs” in the soft material. The magnetic configuration is as Fig. 3.5(c) when the applied field is 0 or small. The “bending field”  $BB$  is a critical point where the exchange spring structure starts to set up when applied magnetic field increases, as Fig. 3.5(d). Domain wall at the interfaces is wild then. Applied field continues to increase, and the domain wall becomes thinner and thinner. Finally the coupling  $J_{Dy-Fe}$  is overcome, therefore all the moments are forced along the field and the spring structure disappears as in Fig. 3.5(e). If the applied field starts to decrease from this saturation condition, the spring reappears and the domain wall extends gradually. Until the spring is completely released as Fig. 3.5(c), it becomes ferrimagnetic. Further at the condition of coercivity, the magnetization of  $DyFe_2$  abruptly switches with the following formation of domain walls again in soft layer.

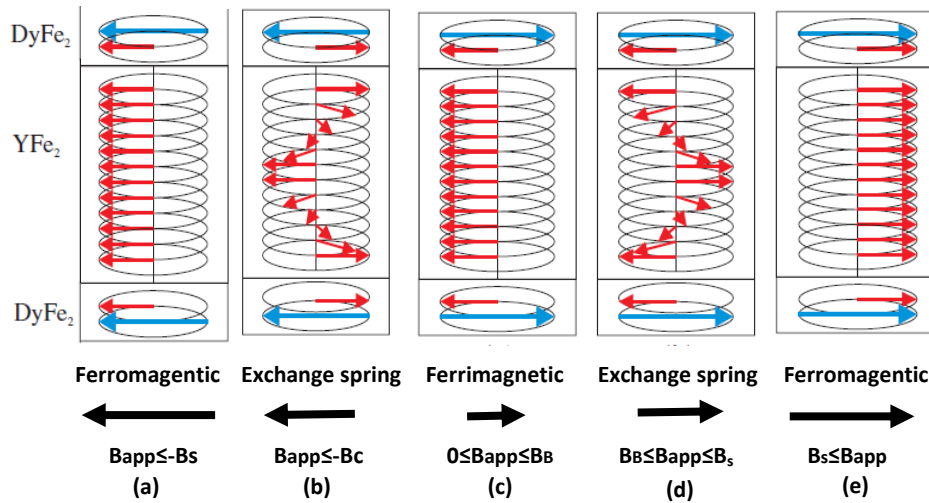


Fig. 3.5. <sup>8</sup>A schematic view of the ferromagnetic, exchange spring and ferrimagnetic state in a DyFe<sub>2</sub>/YFe<sub>2</sub> multilayer. The long arrows represent the Dy moment while the short arrows represent the Fe moment. The arrows below each panel show the direction of the applied field.

The simplest model might be adapted when the magnetization of the DyFe<sub>2</sub> layers dominates. However, it is likely too oversimplified when it comes to the situation where the magnetization of the DyFe<sub>2</sub> and YFe<sub>2</sub> layers are comparable or when the magnetization of the YFe<sub>2</sub> layers dominates<sup>11</sup>. It is necessary to figure out how to compare the magnetization of the two layers. It is known from Fig. 3.4 that the  $m$  value of DyFe<sub>2</sub> layer is the double of YFe<sub>2</sub>, so generally YFe<sub>2</sub> magnetization dominates if the thickness of YFe<sub>2</sub> layer is three or four times larger than that of the DyFe<sub>2</sub> layer. Similarly, DyFe<sub>2</sub> dominates if the thickness of DyFe<sub>2</sub> is the nearly the same or more than YFe<sub>2</sub>. DyFe<sub>2</sub> magnetization almost equals to YFe<sub>2</sub> if around two times at low temperature.

It is verified in many papers that the magnetization reversal processes of DyFe<sub>2</sub>/YFe<sub>2</sub> superlattice is related to the environmental temperature and the relative thickness, as they are two important factors to decide whose magnetization is dominating. K.Dumesnil in 2009<sup>7</sup> described three distinct temperatures and thickness dependent reversal processes in DyFe<sub>2</sub>/YFe<sub>2</sub> superlattice and explained the mechanisms, named rigid magnetic block (RB), soft layers first (SF) and hard layers first (HF).

Reversal as a rigid magnetic block (RB) means that both layers reverse simultaneously without the formation of spring structure. It is believed that individual soft

layer is too thin so that the domain wall can not be able to develop. For example, [DyFe<sub>2</sub>(1nm)/YFe<sub>2</sub>(4nm)] in Ref. [9] exhibits RB behavior.

Soft phase reverses first (SF) is exactly the simple process described in the Fig. 3.5 [DyFe<sub>2</sub>(10nm)/YFe<sub>2</sub>(13nm)] in Ref. [9] follows SF for all temperatures since it is DyFe<sub>2</sub>-magnetization-dominating sample. The abrupt switch of Dy moment is proved by the XMCD results of Dy-L<sub>3</sub> edge in Fig. 3.6. The hysteresis loop at the temperature of 200k is narrower than that at 100k, because the magnetization of DyFe<sub>2</sub> hard material must be reduced with increasing temperature. Additionally, even the YFe<sub>2</sub> magnetization is slightly larger than DyFe<sub>2</sub> magnetization, the sample still experiences SF, but exhibits negative coercivity, which will be shown in 2.2.3.

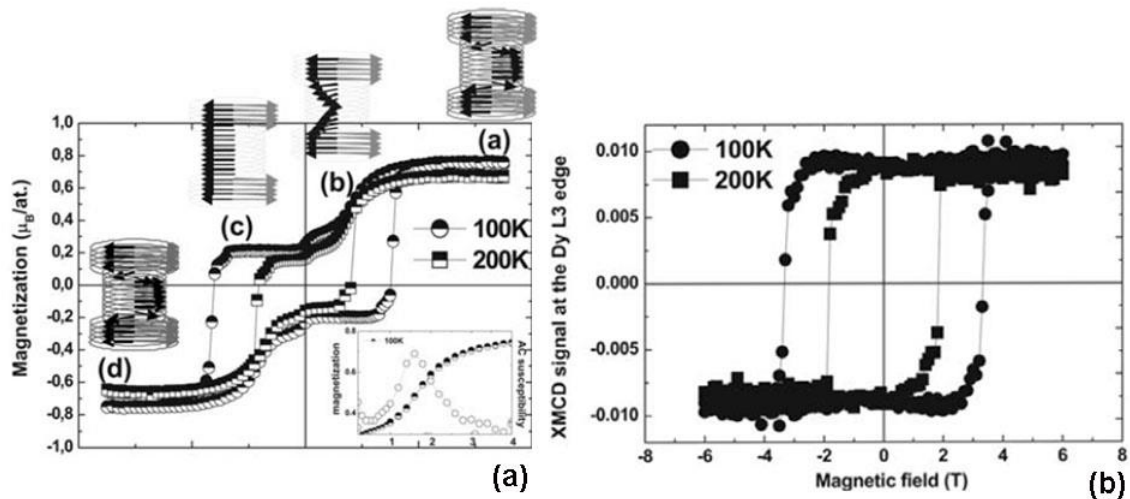


Fig. 3.6. <sup>7</sup>Measurements performed at 100 K and at 200 K for the superlattice SLE. (a) The curves are macroscopic magnetization measurements. The inset presents the superposition of magnetization and AC susceptibility measurements at 100 K (blown up between 0 T and 4 T). Loops in (b) are XMCD results measured at the Dy-L<sub>3</sub> edge.

However, for YFe<sub>2</sub> layer magnetization-dominant sample, it has distinct reversal processes in different temperature regimes. In low temperature regime, it still follows the SF, with possible positive or negative coercivity. But in high temperature regime where the anisotropy and magnetization of DyFe<sub>2</sub> is much reduced, its mechanism changes to HF which is completely different from the classical description of magnetic spring. The process is shown in Fig. 3.7. Starting from a configuration where the net magnetization in both compounds is aligned with a high external field, the first stage of

magnetization reversal affects both compounds, as evidenced by the reduction of the XMCD signals with the decrease of external field at both the Dy and Y edges. This process ends in the complete reversal of the  $DyFe_2$  magnetization around 1 T at 200 K, proved by the fact that the XMCD Dy signal measured at 1T is opposite to the one at 7 T. This process is the so-called Hard First, in comparison to the SF reversal process occurring at lower temperature. This complete reversal of the  $DyFe_2$  layers induces the annihilation of interface magnetic walls (increase of the XMCD signal at the Y edge) and leads to the ferrimagnetic configuration. The second stage of the magnetization reversal is the abrupt switch of the ferrimagnetic block for a negative field close to  $-1$  T, as a result of the Zeeman interaction. Then, the increase of the negative external field tends to progressively break the ferrimagnetic arrangement to align the  $DyFe_2$  magnetization along the field, proved by the decrease of the Dy XMCD signal. This third reversal of the  $DyFe_2$  magnetization drives of course part of the  $YFe_2$  moments, which is again visible as a slight reduction of the XMCD Y signal.

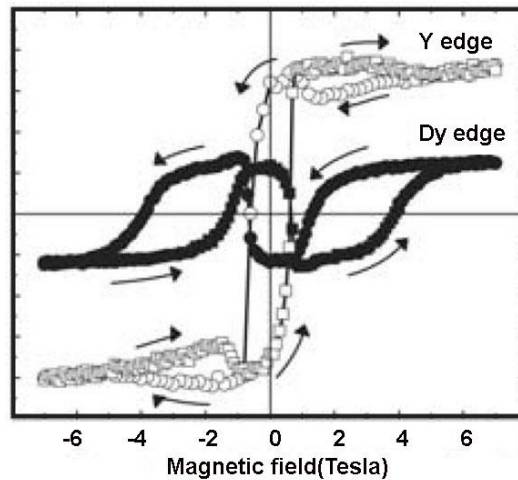


Fig. 3.7.  $^7\text{XMCD}$  results measured at the  $L_3$  edges of Dy (filled symbols) and Y (empty symbols) at the temperature of 200k with  $DyFe_2(5\text{nm})/YFe(20\text{nm})$  superlattice.

### 2.2.2 Irreversible magnetic exchange-spring processes

Generally when discussing the exchange spring, it has been assumed that the hard layer has very high anisotropy and the anisotropy of soft layer is close to zero. Under this assumption, the exchange spring winding and unwinding process is reversible and the bending field  $BB$  is predicted to obey the inverse square law,  $BB \propto 1/ts^2$  where  $ts$  is the

thickness of the soft layer at least at low temperature<sup>22</sup>. This law adapted well to the previous experiments results.

However, Guang-hua Guo proposed that for exchange-coupled hard-soft magnetic bilayers and multilayers, the film with soft layers thicker than  $t_c$  is characterized by a irreversible exchange-spring process<sup>33</sup>.

D.Wang *et al.* in 2009 presented room-temperature magneto-optic Kerr effect (MOKE) studies on surface magnetic exchange springs in  $DyFe_2/YFe_2$  superlattices. It was observed in this work that the bending field at room temperature derivates the previously established inverse square law<sup>27</sup>. The possible reason presented in this paper is the impractical assumption made in that law. In fact, the hard phase should not be seen as infinitely hard and the soft phase also not infinitely soft. D.Wang *et al.* in 2014 presented another work to experimentally prove the reason and theoretically interpretate the antiferromagnetical coupled irreversible exchange springs in  $DyFe_2/YFe_2$  superlattice<sup>29</sup>, by adding a very thin  $DyFe_2$  layer in the  $YFe_2$  soft layer to increase the anisotropy of soft layer.

### 2.2.3 Exchange bias and other phenomena

Based on the property of exchange spring, some other interesting phenomena in  $DyFe_2/YFe_2$  multilayer are observed, e. g. exchange bias effect, tunable coercivity, exchange spring-driven giant magnetoresistance (GMR), *etc.* They extend the applications of exchange spring magnets.

Exchange bias effect of  $DyFe_2/YFe_2$  superlattice is increasingly studied in recent five years for its important technological applications in “spin-valve” devices<sup>14</sup>. Exchange bias is defined as the shift of magnetization of a ferromagnet about the zero of applied magnetic field. For example in Fig. 3.8, we can see the symmetry center of the magnetization curve is not at the zero applied magnetic field, but at -2 T.

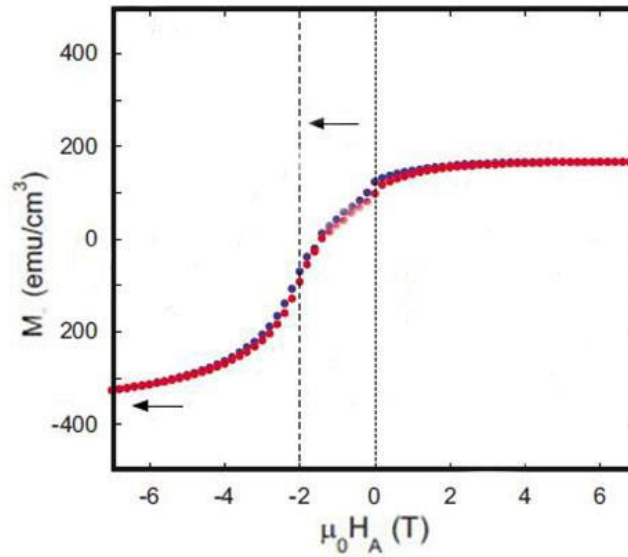


Fig. 3.8. <sup>14</sup>Magnetization curve of DyFe<sub>2</sub>/YFe<sub>2</sub> superlattice with exchange bias.

In addition, the coercivity of DyFe<sub>2</sub>/YFe<sub>2</sub> multilayer or superlattice is adjustable with manipulation of temperature and the thickness of each layer. Especially the negative coercivity, illustrated in Fig. 3.9, was experimentally investigated and theoretically explained<sup>19,23,24,25,34</sup>. The negative coercivity generally occurs when the YFe<sub>2</sub> magnetization dominates. It is also found that the formation of short exchange springs (20Å) in the magnetically soft YFe<sub>2</sub> layers results in a giant magnetoresistance as high as 32% in the spring region<sup>26</sup>.

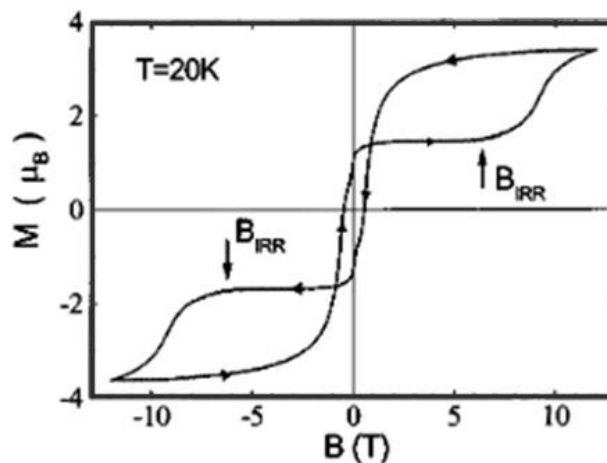


Fig. 3.9. <sup>24</sup>The magnetization curve for DyFe<sub>2</sub> (50Å)/YFe<sub>2</sub> (200Å) superlattice obtained at T=20K. The coercivity is negative in this curve.



In conclusion, this chapter summarizes the crystallographic and magnetic properties of  $\text{DyFe}_2/\text{YFe}_2$  superlattices in literature. Lots of essential information is given, e. g. the epitaxial growth process, lattice parameters, the morphology and the exchange coupling among Dy, Fe and Y moments with and without any applied magnetic field, *etc.*  $\text{DyFe}_2/\text{YFe}_2$  superlattices with various thickness ratios between  $\text{DyFe}_2$  and  $\text{YFe}_2$  layers may exhibit three different magnetization reversal processes, observed by the element-specific XMCD technique. These three reversal processes are described in rich details, revealing the complex coupling behavior in exchange spring systems and offering guidance to analyze the experimental results in chapter V. In addition, some other interesting phenomena based on the property of exchange spring, such as exchange bias effect, are also presented in the latter part. The exploration on these phenomena may bring new application of  $\text{DyFe}_2/\text{YFe}_2$  superlattices.

## Bibliography

1. Fullerton, E. E., Jiang, J. S., Grimsditch, M., Sowers, C. H. & Bader, S. D. Exchange-spring behavior in epitaxial hard/soft magnetic bilayers. *Phys. Rev. B* **58**, 12193–12200 (1998).
2. Franchin, M. *et al.* Micromagnetic Modelling of the Dynamics of Exchange Springs in Multi-Layer Systems. *IEEE Trans. Magn.* **43**, 2887–2889 (2007).
3. Kneller, E. F. & Hawig, R. The exchange-spring magnet: a new material principle for permanent magnets. *IEEE Trans. Magn.* **27**, 3588–3560 (1991).
4. Zimmermann, J. P. *et al.* Magnetic switching modes for exchange spring systems with competing anisotropies. *J. Magn. Magn. Mater.* **321**, 2499–2507 (2009).
5. Dumesnil, K., Dufour, C., Mangin, P. & Rogalev, A. Magnetic springs in exchange-coupled DyFe<sub>2</sub>/YFe<sub>2</sub> superlattices: An element-selective x-ray magnetic circular dichroism study. *Phys. Rev. B* **65**, 094401 (2002).
6. Dumesnil, K., Dufour, C., Mangin, P., Rogalev, A. & Wilhelm, F. Temperature dependence in the magnetization reversal process of DyFe<sub>2</sub>/YFe<sub>2</sub> exchange-coupled superlattices. *J. Phys. Condens. Matter* **17**, L215 (2005).
7. Dumesnil, K. *et al.* Temperature and thickness dependence of the magnetization reversal in DyFe<sub>2</sub>/YFe<sub>2</sub> exchange-coupled superlattices. *Eur. Phys. J. B* **72**, 159–171 (2009).
8. Bentall, M. J. *et al.* Magnetic structures of Laves phase superlattices. *J. Phys. Condens. Matter* **15**, 4301 (2003).
9. Bentall, M. J., Ward, R. C. C., Grier, E. J. & Wells, M. R. Structure of DyFe<sub>2</sub>/YFe<sub>2</sub> Laves phase superlattices grown by molecular beam epitaxy. *J. Phys. Condens. Matter* **15**, 6493 (2003).
10. Dumesnil, K., Dufour, C., Mangin, P., Wilhelm, F. & Rogalev, A. Thermal dependence of magnetic springs location in a DyFe<sub>2</sub>/YFe<sub>2</sub> superlattice. *J. Appl. Phys.* **95**, 6843–6845 (2004).
11. Dumesnil, K. *et al.* Magnetization reversal in a YFe<sub>2</sub>-dominant DyFe<sub>2</sub>/YFe<sub>2</sub> exchange-coupled superlattice: An x-ray magnetic circular dichroism and polarized neutron reflectometry study. *J. Appl. Phys.* **97**, 10K108–10K108–3 (2005).
12. Fitzsimmons, M. R. *et al.* Vector magnetization depth profile of a Laves-phase exchange-coupled superlattice obtained using a combined approach of micromagnetic simulation and neutron reflectometry. *Phys. Rev. B* **73**, 134413 (2006).
13. Zimmermann, J. P. *et al.* Micromagnetic simulation of the magnetic exchange spring system DyFe<sub>2</sub>/YFe<sub>2</sub>. *J. Appl. Phys.* **99**, 08B904 (2006).

14. Fitzsimmons, M. R., Dufour, C., Dumesnil, K., Dou, J. & Pechan, M. Mechanisms of exchange bias in DyFe<sub>2</sub>/YFe<sub>2</sub> exchange-coupled superlattices. *Phys. Rev. B* **79**, 144425 (2009).
15. Dumesnil, K. *et al.* Low temperature exchange bias in [DyFe<sub>2</sub>/YFe<sub>2</sub>] superlattices: effect of the thermo-magnetic preparation. *J. Phys. Condens. Matter* **21**, 236002 (2009).
16. Stenning, G. B. G. *et al.* Magnetic reversal in a YFe<sub>2</sub> dominated DyFe<sub>2</sub>/YFe<sub>2</sub> multilayer film. *Appl. Phys. Lett.* **101**, 072412–072412–4 (2012).
17. Stenning, G. B. G. *et al.* Transverse magnetic exchange springs in a DyFe<sub>2</sub>/YFe<sub>2</sub> superlattice. *Phys. Rev. B* **86**, 174420 (2012).
18. Dufour, C. *et al.* Nanometer-size magnetic domains and coherent magnetization reversal in a giant exchange-bias system. *Phys. Rev. B* **84**, 064420 (2011).
19. Sawicki, M. *et al.* Engineering coercivity in epitaxially grown (110) films of DyFe<sub>2</sub>/YFe<sub>2</sub> superlattices. *Appl. Phys. Lett.* **77**, 573–575 (2000).
20. Sawicki, M. *et al.* Magnetic properties of epitaxial (110) multilayer films of DyFe<sub>2</sub> and YFe<sub>2</sub>. *J. Appl. Phys.* **87**, 6839–6841 (2000).
21. Dumesnil, K., Dutheil, M., Dufour, C. & Mangin, P. Spring magnet behavior in DyFe<sub>2</sub>/YFe<sub>2</sub> Laves phases superlattices. *Phys. Rev. B* **62**, 1136–1140 (2000).
22. Sawicki, M. *et al.* Exchange springs in antiferromagnetically coupled DyFe<sub>2</sub>-YFe<sub>2</sub> superlattices. *Phys. Rev. B* **62**, 5817–5820 (2000).
23. Beaujour, J. M. L. *et al.* Effect of exchange springs on the coercivity of DyFe<sub>2</sub>-YFe<sub>2</sub> superlattices. *J. Magn. Magn. Mater.* **226–230, Part 2**, 1714–1716 (2001).
24. Beaujour, J.-M. L. *et al.* Negative coercivity in epitaxially grown (110) DyFe<sub>2</sub>/YFe<sub>2</sub> superlattices. *Appl. Phys. Lett.* **78**, 964–966 (2001).
25. Gordeev, S. N. *et al.* Spin configurations and negative coercivity in epitaxially grown DyFe<sub>2</sub>/YFe<sub>2</sub> superlattices. *J. Appl. Phys.* **89**, 6828–6830 (2001).
26. Gordeev, S. N. *et al.* Giant Magnetoresistance by Exchange Springs in DyFe<sub>2</sub>/YFe<sub>2</sub> Superlattices. *Phys. Rev. Lett.* **87**, 186808 (2001).
27. Wang, D. *et al.* Room temperature magneto optic exchange springs in superlattices. *J. Magn. Magn. Mater.* **321**, 586–589 (2009).
28. Djedai, S. & Berche, P. E. Monte Carlo simulation of the magnetic exchange spring system DyFe<sub>2</sub>(1)/YFe<sub>2</sub>(4). *J. Phys. Conf. Ser.* **286**, 012036 (2011).
29. Wang, D., Buckingham, A. R., Bowden, G. J., Ward, R. C. C. & Groot, P. A. J. de. Engineering irreversibility of exchange springs in antiferromagnetic DyFe<sub>2</sub>/YFe<sub>2</sub> superlattices. *Mater. Res. Express* **1**, 036110 (2014).

30. Djedai, S., Talbot, E. & Berche, P. E. A Monte Carlo study of the magnetization reversal in DyFe<sub>2</sub>/YFe<sub>2</sub> exchange-coupled superlattices. *J. Magn. Magn. Mater.* **368**, 29–35 (2014).
31. Mougin, A., Dufour, C., Dumesnil, K. & Mangin, P. Strain-induced magnetic anisotropy in single-crystal RFe<sub>2</sub>(110) thin films (R=Dy, Er, Tb, Dy<sub>0.7</sub>Tb<sub>0.3</sub>, Sm, Y). *Phys. Rev. B* **62**, 9517–9531 (2000).
32. Oderno, V. *et al.* Magnetic anisotropy in (110) epitaxial DyFe<sub>2</sub> Laves phase. *Phys. Rev. B* **54**, R17375–R17378 (1996).
33. Guo, G. *et al.* Irreversible magnetic exchange-spring processes in antiferromagnetic exchange-coupled bilayer systems. *Appl. Phys. Lett.* **93**, 102505 (2008).
34. Bowden, G. J. *et al.* Modeling the magnetic properties of DyFe<sub>2</sub>/YFe<sub>2</sub> superlattices. *J. Appl. Phys.* **93**, 6480–6482 (2003).



## Chapter IV

### **Experimental Results of MnAs/GaAs(001) Epitaxial Layers**

---

This chapter presents the experimental results of MnAs/GaAs(001) epitaxial layers. After a brief introduction of the sample preparation in section 1, structural properties of the sample obtained with several techniques will be described in section 2. How the hexagonal  $\alpha$ -MnAs and quasi-hexagonal  $\beta$ -MnAs are distinguished by electron diffraction in a TEM is highlighted. What follows in the next two sections is the EMCD study on the identified  $\alpha$ -MnAs crystal along the easy, hard and intermediate axes at RT, and then on its phase transition into  $\beta$ -MnAs. Lots of details of this original work on EMCD will be displayed. In addition, an observation of the phase transition by an electron holography technique will be added in the last section, as complementary information to the EMCD results. The background knowledge on the EMCD technique and MnAs/GaAs(001) epitaxial layers have already been shown in chapter I and II respectively.

#### **1. Sample preparation**

The MnAs thin films were grown using the solid-source molecular beam epitaxy (MBE) technique on semi-insulating GaAs(001) substrates, in the Institut des NanoSciences de Paris<sup>1</sup>. At first, epi-ready GaAs substrates were deoxidized under As overpressure at elevated temperature. A GaAs buffer layer was then grown in standard growth conditions. To optimize the surface quality, the surface was annealed at 600 °C under As until the presence of a clear  $(2\times 4)\beta$  diagram, at the end of buffer layer growth. After the  $(2\times 4)$  reconstruction formation, samples were cooled down to 350°C and annealed for more than two hours under As-rich condition<sup>2</sup>. A stable and high-quality As-terminated  $c(4\times 4)$  surface was thus ready. The MnAs film growth was performed at 260 °C under As-rich condition and a growth rate of about 3 nm/min. The whole growth procedure was monitored by reflection high-energy electron diffraction (RHEED).

Finally a 10-nm-thick As capping-layer was deposited on a 150-nm-thick MnAs epilayer for preventing MnAs surface oxidation in the MBE chamber, after the cooling down the sample to the lowest temperature in MBE system. The detailed description of MBE technique is provided in Appendix III.

Grown MnAs/GaAs(001) samples were used to prepare two cross-section specimens and one plan-view specimen for TEM experiments, following the process of specimen preparation described in Appendix II. One of the cross-section specimens has a zone axis parallel to the easy axis MnAs[11 $\bar{2}$ 0] and the other one has a zone axis parallel to the hard axis MnAs[0001]. The plan-view specimen has the plane perpendicular to the intermediate axis MnAs [ $\bar{1}$ 100]. It should be mentioned that the As capping-layer has been removed from the surface of a bulk sample by being evaporated at high temperature before preparing the plan-view specimen, while in the cross-section specimens, the capping layer was kept.

## 2. Structural Characterization at Room Temperature

Structural characterization was performed using several techniques successively. The growth direction of the MnAs film was checked by X-ray diffraction (XRD) just after the synthesis of the sample. A map of the magnetic contrast on the film surface, which implied the pattern of  $\alpha$ - and  $\beta$ -MnAs stripes, was acquired on a capping-layer-removed bulk sample using the magnetic force microscope (MFM). The cross-section and plan-view specimens were then observed in a TEM, providing crystallographic information obtained along various directions of MnAs. Special efforts were made to study how to make a distinction between the  $\alpha$ - and  $\beta$ -MnAs by electron diffraction. I will explain the method to distinguish the two phases with simulated diffraction patterns and then display experimental patterns to show its validity.

### 2.1 X-ray diffraction (XRD)

XRD  $\theta - 2\theta$  scans were carried out on a laboratory 5-circles diffractometer (Rigaku Smartlab), equipped with a  $CuK_{\alpha 1}$  radiation. A XRD  $\theta - 2\theta$  scan is shown in Fig. 4.1. The peaks around  $27.7^\circ$ ,  $57.1^\circ$ ,  $91.7^\circ$  correspond to  $(\bar{1}100)$ ,  $(\bar{2}200)$  and  $(\bar{3}300)\alpha -$

MnAs planes, respectively. It indicates that the MnAs film is constituted of only one epitaxial out-of-plane orientation, which is MnAs( $\bar{1}100$ ). The peaks corresponding to GaAs(002) and GaAs(006) planes verifies that the MnAs layer is grown on the GaAs(001) substrate. In addition, a weak peak denoted by an arrow in the figure, and shifted about  $1.3^\circ$  from the large ( $\bar{3}300$ ) peak of  $\alpha$ -MnAs, is attributed to  $\beta$ -MnAs. It indicates the coexistence of the two phases at RT.

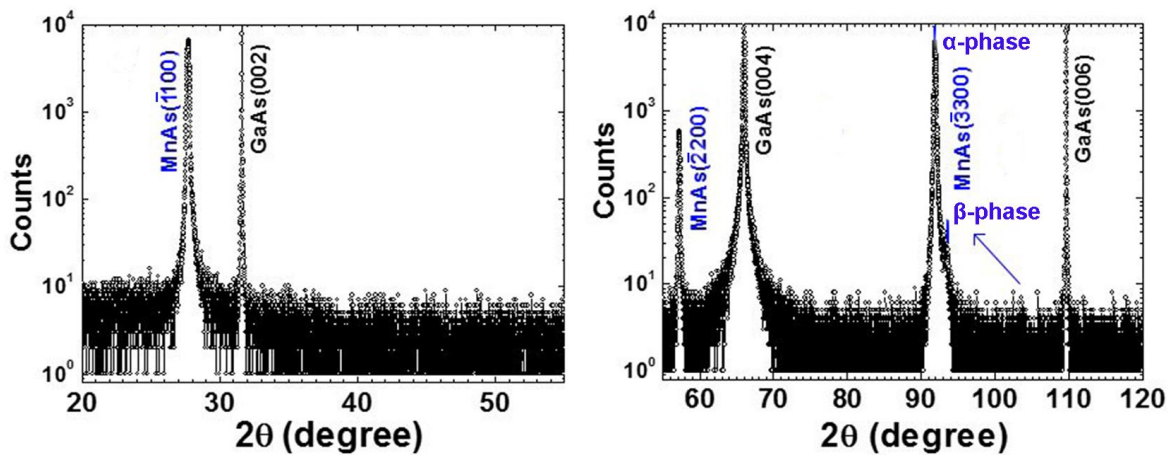


Fig. 4.1. X-ray diffraction (XRD)  $\theta - 2\theta$  scan for MnAs thin film grown on GaAs(001) substrate. (done by in the Institut des NanoSciences de Paris<sup>1</sup>)

## 2.2 Magnetic force microscopy (MFM)

As expected from the previous study presented in chapter II, a MnAs film grown on GaAs substrate is known to have a unique structure, in the form of self-organized periodic stripes of two phases in the temperature range of  $20^\circ\text{C}$  to  $45^\circ\text{C}$ . MFM was performed at the CEMES to observe the magnetic contrast of the MnAs thin film at remanence after being magnetized along the easy axis, at room temperature. MFM experiment was made on a Bruker Multimode AFM operated in LiftMode procedure.

The MFM scan in Fig. 4.2(a) shows some periodic stripe-like bright and dark contrasts which stretch along the  $[0001]$  direction. The period of those stripes is about  $1\ \mu\text{m}$ . The principle of the MFM technique will be simply explained here before interpreting Fig. 4.2(a). The MFM maps the sample surface magnetization by recording the magnetostatic force or vertical force gradient due to stray fields emanating from the



sample<sup>3</sup>. As illustrated in Fig. 4.2(e), the contrast indicates that there is a change of magnetization, and the brighter parts generally correspond to an upward stray field while the darker parts correspond to a reverse one. However, our sample is at remanence after being saturated along the easy axis  $[11\bar{2}0]$ . It means the magnetization is almost along the same direction, so the periodic contrasts in Fig. 4.2(a) do not come from a magnetization reversal as shown in Fig. 4.2(e), but are more likely due to alternating ferromagnetic  $\alpha$ -MnAs and non-ferromagnetic  $\beta$ -MnAs stripes as demonstrated in Fig. 4.2(c-d).

Our MFM result agrees with what is published in literature. Chapter II has shown several MFM images extracted from the literature and discussed that the domain pattern of MnAs thin film is dependent of the film thickness, temperature and applied magnetic field, thus the MFM images should be dependent of these factors as well. However, no MFM images in chapter II were acquired a MnAs film with a similar film thickness to our sample, which is 150nm thick. Even so, we can have a look at the similarity and difference, by comparing Fig. 2.4(b) in chapter II and Fig. 4.2(a) in this chapter. The periodic stripe-like contrasts stretching along  $[0001]$  direction can be clearly seen in both MFM images, indicating the coexistence of  $\alpha$  and  $\beta$  phases. But it is easy to find that finer contrasts within the ferromagnetic stripes can be observed in Fig. 2.4(b) of chapter II but not in ours. It is because the  $\beta$  stripes are not wide enough in our case, so that the magnetic moments within the neighbouring  $\alpha$  stripes still have strong antiparallel coupling with each other over the  $\beta$  stripes.

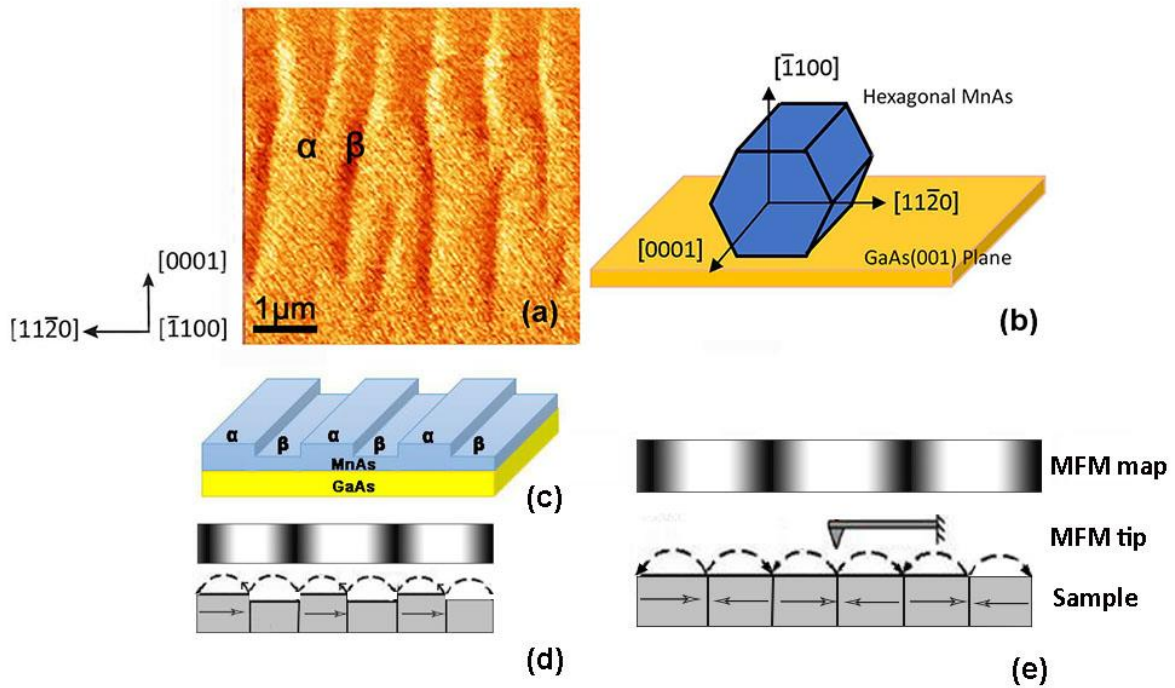


Fig. 4.2. (a)  $5 \times 5\mu\text{m}^2$  MFM scan of MnAs thin film at remanence at RT. (b) schematic diagram of  $\alpha$ -MnAs crystal orientation. (c) A sketch of MnAs surface with alternating  $\alpha$ - and  $\beta$ -MnAs stripes. (d) A sketch of MFM detected from the surface plane of the MnAs film and its possible corresponding magnetization configuration in ferromagnetic and non-ferromagnetic stripes. (e) A sketch of magnetization configuration in a sample and its corresponding contrasts in the MFM map for demonstrating the principle of MFM.

As a conclusion, our MFM image implies that the ferromagnetic  $\alpha$ -MnAs and non-ferromagnetic  $\beta$ -MnAs stripes appear alternatively along the direction of  $[0001]$  at RT. For the sake of clarity, Fig. 4.2 (a) and (b) give the relationship between the stripe direction and crystal orientation of the  $\alpha$ -MnAs with respect to the (001) plane of GaAs substrate. In addition, such a contrast between the two phases can hardly be directly observed by TEM imaging, due to their similar crystal structures<sup>4</sup>. However, the distinction between the two phases can still be made in the diffraction mode of TEM and it will be presented in the following section 2.3.

## 2.3 Transmission electron microscopy (TEM)

### 2.3.1 TEM imaging

In this section, I'm going to present the morphology and the structure of the studied samples. It will be the starting point of the next key experiments of EMCD.

It was at first determined by electron diffraction that the plan-view sample is a single crystal with some defects in it. Fig. 4.3 (a) and (b) display a low-magnification bright-field and a high-resolution image of the plan-view sample, as well as a diffraction pattern. All these images were recorded along the same MnAs $[\bar{1}100]$  zone axis. From both the low-mag and high-resolution images, the boundary between  $\alpha$  and  $\beta$  phases cannot be resolved, as the crystal structures of the two phases are too similar.

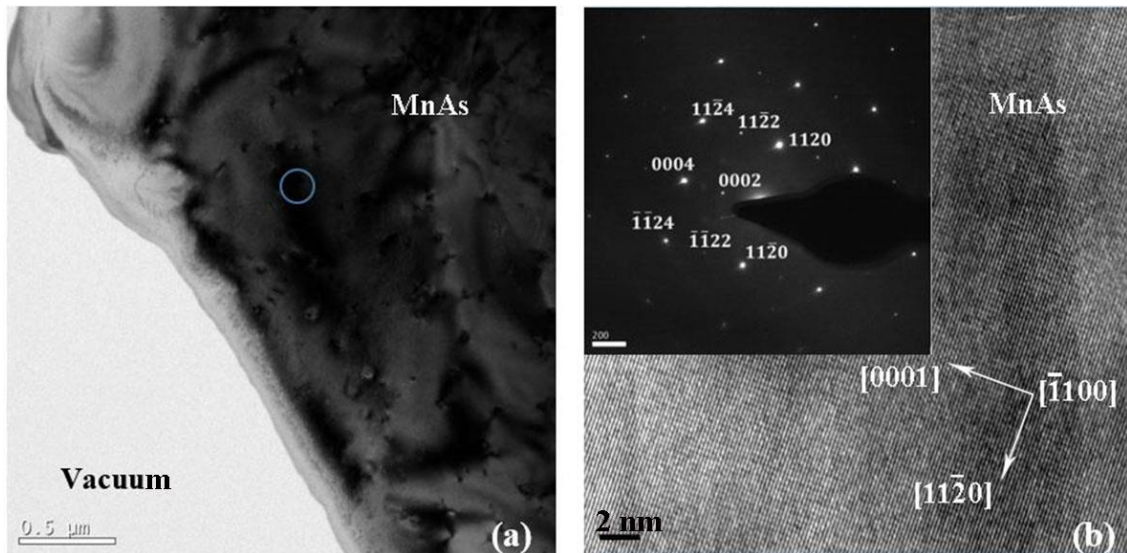


Fig. 4.3. (a) low-magnification bright-field, and (b) high-resolution TEM image of a plan-view sample recorded along the MnAs  $[\bar{1}100]$  zone axis. The indexed diffraction pattern recorded along the same zone axis illustrates the crystal orientation.

Images of Fig. 4.4 and 4.5 illustrate what is observed for cross-section samples. In Fig.4.4, the MnAs zone axis was set to  $[0001]$ . The low-magnification image in Fig. 4.4 (a) displays the regular 150-nm-thick MnAs layer, capped by a 10-nm-thick As layer, and in the other side, grown on the GaAs substrate. The central grey-light phase is the glue used for TEM preparation of the cross-section. The high resolution image of Fig. 4.4(b) is acquired in the position denoted by a circle in Fig. 4.4(a). This latter image clearly

demonstrates the epitaxial relationship between MnAs and GaAs. The  $[11\bar{2}0]$  magnetic easy axis of MnAs is parallel to GaAs $[110]$ , and MnAs  $[0001]$  is parallel to GaAs  $[\bar{1}10]$ . Moreover, the interface appears rather flat, indicating the high-quality epitaxy of the MnAs layer on the GaAs substrate. Some misfit dislocations can however be observed at the interface, due to the difference of lattice constant between GaAs and MnAs crystals. The measured interplaner distance of MnAs $(11\bar{2}0)$  and GaAs $(110)$  is 0.189 nm and 0.202 nm respectively. Thus the in-plane lattice mismatch along the MnAs  $[11\bar{2}0]$  and GaAs $[110]$  crystallographic direction is 6.43%. My calculated lattice mismatch is consistent with the value of about 7% in Ref. [5]. One dislocation is pointed out by an arrow as an example.

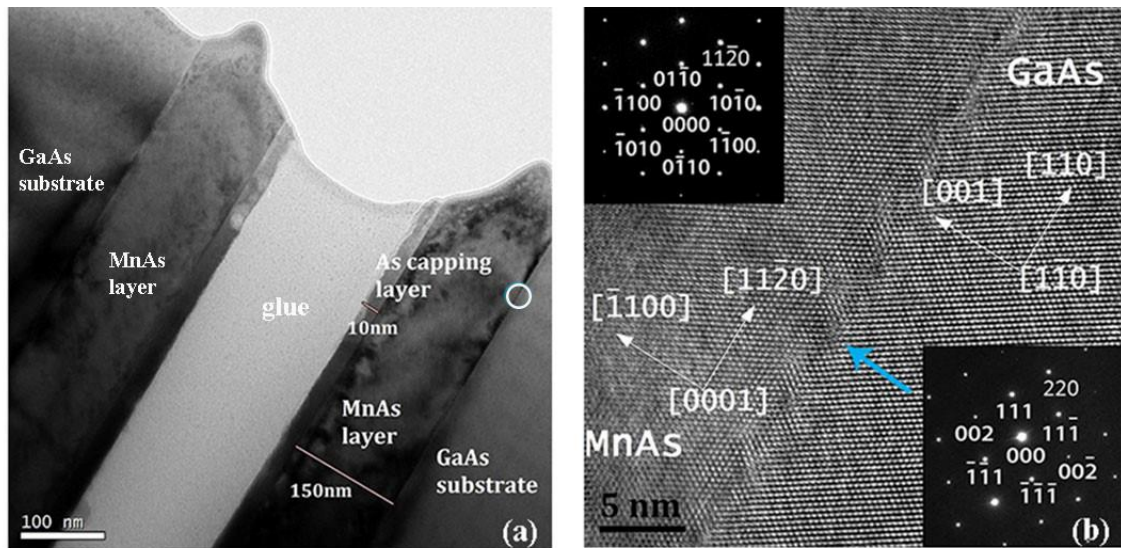


Fig. 4.4. Cross-sectional sample: (a) Low-magnification TEM image, and (b) HREM image of the MnAs/GaAs(001) heterostructure along the zone axis of MnAs $[0001]$ //GaAs $[1\bar{1}0]$  at RT, the image has been processed by Wiener Filter. The upper-left insert in (b) is the diffraction pattern of MnAs layer acquired at the  $[0001]$  zone axis and in the other insert is the diffraction pattern of GaAs substrate acquired at the  $[1\bar{1}0]$  zone axis.

The low-magnification and high-resolution images in Fig. 4.5 were acquired on a different cross-section specimen along the MnAs $[11\bar{2}0]$  zone axis. Similar to Fig. 4.4(a), Fig. 4.5(a) displays the regular 150-nm-thick MnAs layer, capped by a 10-nm-thick As

layer and grown on the GaAs substrate. Fig. 4.5(b) is a high-resolution image acquired in the position denoted by a circle in Fig. 4.5(a). The interface is rather flat and the misfit dislocations also exist at the interface. The measured interplaner distance of MnAs(0001) and GaAs(1 $\bar{1}$ 0) is 0.198nm and 0.283nm respectively. Thus the in-plane lattice mismatch along the MnAs[11 $\bar{2}$ 0] and GaAs[110] crystallographic direction is 30.00%, which agrees very well with the value of about 30% in Ref. [5].

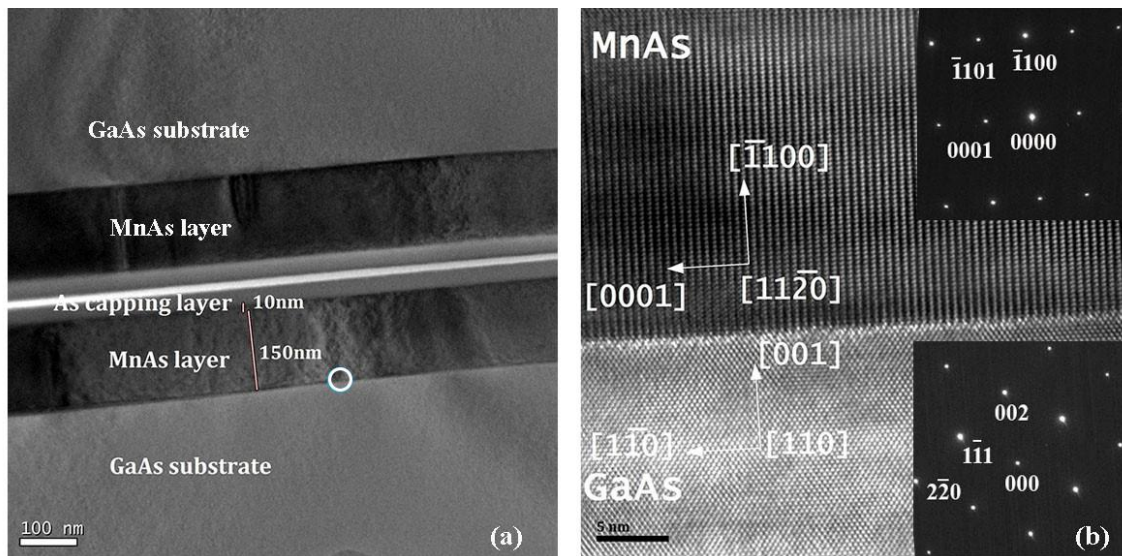


Fig. 4.5. Second cross-sectional sample: (a) Low-magnification TEM image, and (b) HREM image of the MnAs/GaAs(001) heterostructure along the zone axis of MnAs[11 $\bar{2}$ 0]//GaAs[110] at RT, processed by a Wiener Filter (cf. Appendix I). The upper-right insert in (b) is the diffraction pattern of MnAs layer acquired at the [11 $\bar{2}$ 0] zone axis and in the other insert is the diffraction pattern of GaAs substrate acquired at the [110] axis.

### 2.3.2 Electron diffraction

In chapter II, it has been in particular reported that the  $\alpha$ -MnAs of MnAs thin film displays magnetocrystalline anisotropy: along the easy axis [11 $\bar{2}$ 0] and hard axis [0001] lying in the ( $\bar{1}$ 100) plane, and also along an intermediate axis [ $\bar{1}$ 100], corresponding to out-of-plane anisotropy, for which the saturation field is in between the one along easy axis and hard axis. Before studying the magnetocrystalline anisotropy of the magnetic  $\alpha$ -MnAs using EMCD technique, we must firstly distinguish  $\alpha$ -MnAs from  $\beta$ -MnAs at RT.

We are going to see that it will be reachable by electron diffraction in some very specific situations.

It is known that  $\alpha$ -MnAs crystallizes in the hexagonal NiAs-type (B8<sub>1</sub>) structure, and  $\beta$ -MnAs in the orthorhombic MnP-type (B31) structure. In fact, the lattice of  $\beta$ -MnAs corresponds to the slightly distorted  $\alpha$ -MnAs lattice, thus the  $\beta$ -MnAs is also considered as quasi-hexagonal. Fig. 4.6(a-h) demonstrate the similarity as well as the tiny difference between atomic structures of the two phases. For better demonstrating the similarity of the two phases in Fig. 4.6(a-d), the hexagonal crystal of  $\alpha$ -MnAs and the orthorhombic crystal of  $\beta$ -MnAs are orientated such that  $\alpha$ -MnAs[0001] is parallel to  $\beta$ -MnAs[100] and  $\alpha$ -MnAs[11 $\bar{2}$ 0] is parallel to  $\beta$ -MnAs[010]. A c axis is defined as the [0001] axis in  $\alpha$ -MnAs and the [100] axis in  $\beta$ -MnAs. Fig. 4.6(c-d) are atomic structures of the two phases observed along their defined c axes. I separate the 1, 2 and 3 planes in both lattices, thus we can clearly see how the lattice is regularly distorted from  $\alpha$ -MnAs to  $\beta$ -MnAs. All the atoms in plane 1, 2 and 3 of  $\beta$ -MnAs are slightly dislocated along the line that is parallel to the  $\alpha$ -MnAs[ $\bar{1}$ 100] axis, but the dislocation direction in plane 1 and 3 is opposite to that in plane 2, as displayed in Fig. 4.6(e-h). The atom dislocation is actually smaller than 3%, so that the boundary between the two phases could not be resolved in HRTEM images and unfortunately, as a result of simulation, their diffraction patterns are also too similar to differentiate at most zone axes in practical cases. The diffraction patterns of  $\alpha$ -MnAs and  $\beta$ -MnAs along their c axes are given as an example in Fig. 4.6(i) and (j) to show how similar their diffraction patterns can be.

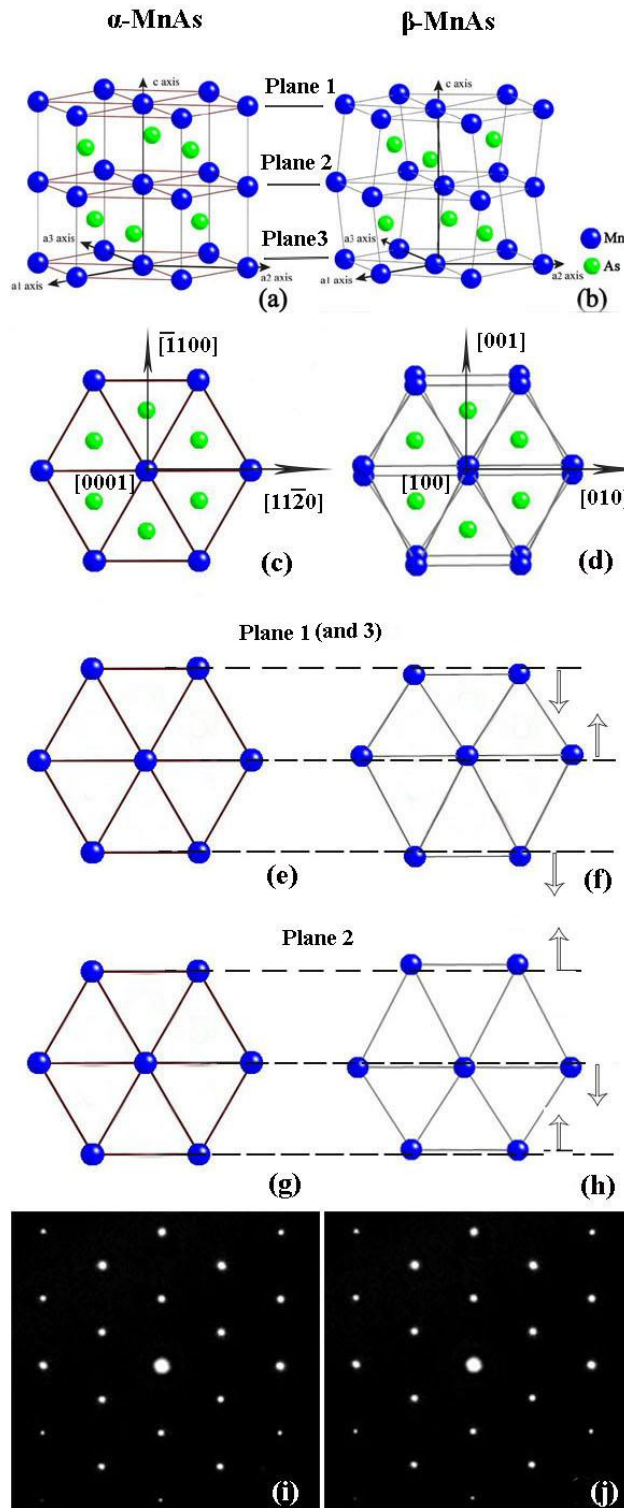


Fig. 4.6. Atomic structures of (a) hexagonal  $\alpha$ -MnAs with its  $c$  axis; (b) orthorhombic  $\beta$ -MnAs with a defined  $c$  axis; (c)  $\alpha$ -MnAs along the  $c$  zone axis; (d)  $\beta$ -MnAs along the  $c$  zone axis. The positions of atoms in plane1 and 3 for (e)  $\alpha$ -MnAs and (f)  $\beta$ -MnAs; the positions of atoms in plane 2 for (g)  $\alpha$ -MnAs and (h)  $\beta$ -MnAs. (i) A simulated diffraction pattern of (i)  $\alpha$ -MnAs and (j)  $\beta$ -MnAs along the  $c$  zone axis, by PDF software.

Fortunately, because of the regular distortions, though small, electron diffraction patterns of  $\beta$ -MnAs at some specific zone axis may differ from the patterns of  $\alpha$ -MnAs. Before precisely illustrating those specific zone axes, I have to clarify the crystal orientations of  $\alpha$ - and  $\beta$ -MnAs with respect to the GaAs substrate, in order to provide unambiguous guidance to distinguish the two phases in the real TEM experiment. Fig. 4.7 shows one possible orientation for  $\alpha$ -MnAs but three possible ones for  $\beta$ -MnAs, from the view of  $c$  axis. The  $\alpha$ -MnAs crystal has an hexagonal symmetry, so there are six lattice axes equivalent to MnAs[11 $\bar{2}$ 0], but we define the one parallel to the GaAs[110] as MnAs[11 $\bar{2}$ 0] and the growth axis of  $\alpha$ -MnAs as MnAs [ $\bar{1}$ 100], as shown in Fig. 4.7(a). However, the  $\beta$ -MnAs crystal is orthorhombic, and there are three possible growth axes, which are  $\beta$ -MnAs[001],  $\beta$ -MnAs[031] and  $\beta$ -MnAs[0 $\bar{3}$ 1] as shown in Fig. 4.7(b-d). I name them  $\beta$ 1,  $\beta$ 2 and  $\beta$ 3 respectively. Fig. 4.6(c-d) just shows the case in Fig. 4.7(a) and (b). One should note that in Fig. 4.7(b-d), only the crystal orientations are different, and there is no any difference at all in the crystal structure. Which one actually corresponds to our sample is not known yet. A question now arises that is it possible to determine the growth axis of  $\beta$ -MnAs from the XRD spectra in Fig. 4.1? The answer is no. The  $2\theta$  angles of the (006), (03 $\bar{3}$ ) and (033) planes corresponding to the three possible orientations of  $\beta$ -MnAs are very close and cannot be discriminated in the X-ray  $\theta - 2\theta$  diagram. So, only one peak for  $\beta$ -MnAs is present as a shoulder of the intense peak of  $\alpha$ -MnAs. The simulation will be done for the four possibilities. For convenience, the same  $a$ ,  $b$  and  $c$  axes are defined for all of them.

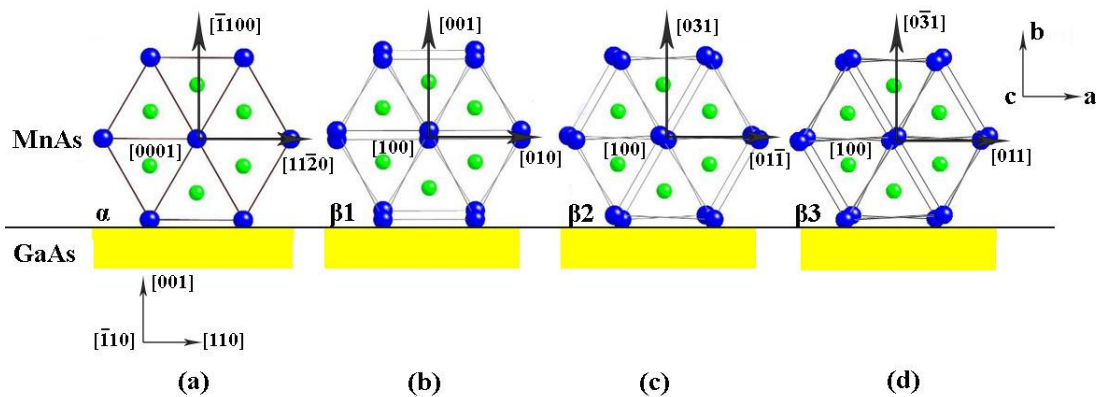


Fig. 4.7. The relative orientations of the GaAs crystal and (a)  $\alpha$ -MnAs, (b)  $\beta$ 1-MnAs, (c)  $\beta$ 2-MnAs and (d)  $\beta$ 3-MnAs crystal. General  $a$ ,  $b$  and  $c$  axes are defined for all the four cases.



I make the  $c$  axis as the initial zone axis for all the four simulated crystals  $\alpha$ -MnAs,  $\beta_1$ -MnAs,  $\beta_2$ -MnAs and  $\beta_3$ -MnAs. Along this initial zone axis, no difference can be seen from their simulated diffraction patterns. But when those crystals are orientated by  $66.10^\circ$  around the  $a$  axis to reach a specific zone axis, some extra spots appear on the diffraction patterns of  $\beta_1$ -MnAs,  $\beta_2$ -MnAs and  $\beta_3$ -MnAs, compared with the pattern of  $\alpha$ -MnAs. Fig. 4.8 (e-h) present those diffraction patterns, and the extra spots are denoted by arrows. Their corresponding atomic structures from the view of this specific zone axis are just put above them. The extra spots originate from a longer-range order that appears due to the displacement of atoms in some lattice plane to opposite directions alternatively. As a conclusion, we can distinguish the two phases by the electron diffraction after tilting the MnAs crystal from the initial  $c$  zone axis by  $66.10^\circ$  around  $a$  axis.

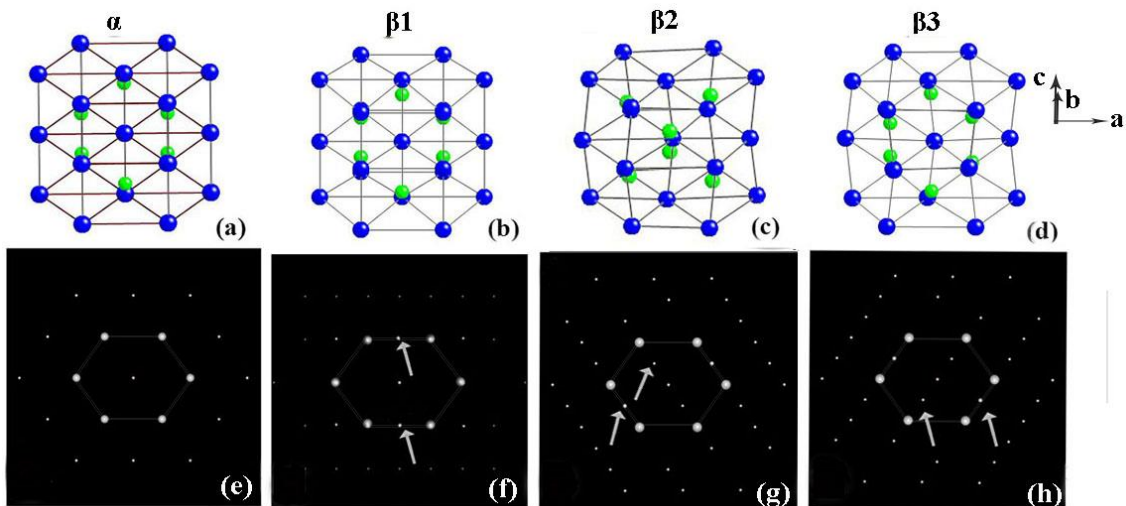


Fig. 4.8. (a) The atomic structure of hexagonal  $\alpha$ -MnAs seen from the  $[\bar{2}201]$  zone axis; (b-d) the atomic structure of orthorhombic  $\beta$ -MnAs seen from (b)[103], (c) [131] and (d)  $[\bar{1}\bar{3}1]$ . The zone axis here is reached by tilting the four crystals in Fig. 4.7 by  $66.10^\circ$  around  $a$  axis from the zone axis  $c$ . The simulated diffraction patterns in (e-h) correspond to the atomic structures in (a-d) respectively.

From a practical point of view, it has to be mentioned that tilting the sample by  $60^\circ$  is not routine in a TEM. For example, the TEM used in my experiment allows only a tilt angle of  $30^\circ$  at most. As described in section 4.1, one plan-view specimen and two cross-section specimens need to be investigated. For the plan-view specimen, the initial zone axis is actually along the  $b$  axis instead of  $c$  axis. That is to say, a tilt angle of  $23.9^\circ$

( $90^\circ-66.10^\circ$ ) around a axis is enough to reach that specific zone axis  $[2\bar{2}01]$ . But for the cross-section specimen in Fig. 4.4, a rotation of  $66.10^\circ$  around a axis is necessary, and for the cross-section specimen in Fig. 4.5, the rotation is more than  $66.10^\circ$  around both a and b axes. Therefore, other zone axes have to be found.

For the cross-section specimen in Fig. 4.4, the initial zone axes for the four crystals are along the defined c axis. When they are orientated by  $12^\circ$  around the b axis, some extra spots appear in the diffraction pattern of  $\beta_1$ -MnAs, but no visible difference can be seen in the patterns of  $\alpha$ ,  $\beta_2$ - and  $\beta_3$ -MnAs, as shown in Fig. 4.9. That is to say, if the extra spots appear, we can confirm the existence of  $\beta$ -MnAs and understand that the orientation of  $\beta$ -MnAs is in the case of  $\beta_1$ . Here the  $\beta_1$ -MnAs is orientated along the zone axis of  $[310]$ . But if there is no any extra spot, it does not necessarily mean  $\alpha$ -MnAs but possibly  $\beta_2$  and  $\beta_3$ . In the case that it is  $\beta_2$  or  $\beta_3$ -MnAs, we can orientate the crystals along the zone axis  $[310]$  and there should be extra spots like Fig. 4.9(f), otherwise it must be  $\alpha$ -MnAs. The  $[310]$  zone axis for  $\beta_2$  can be reached by tilting the crystal from the c axis by  $10^\circ$  counterclockwise around the a axis, and then by  $6^\circ$  clockwise around the b axis. The  $[310]$  zone axis for  $\beta_3$  can be reached by tilting the crystal from the c axis by  $10^\circ$  clockwise around the a axis, and then by  $6^\circ$  clockwise around the b axis. The diffraction patterns are demonstrated in Fig. 4.10. Here the  $\alpha$ - and  $\beta_1$ -MnAs are tilted in the same pace with  $\beta_3$ -MnAs, just for reference. Actually from the practical point of view, if no extra spots appear when the crystals are orientated from the c zone axis by  $\pm 12^\circ$  around b axis, or by  $\pm 10^\circ$  around a axis followed by  $\pm 6^\circ$  around b axis, the  $\alpha$ -MnAs is identified.

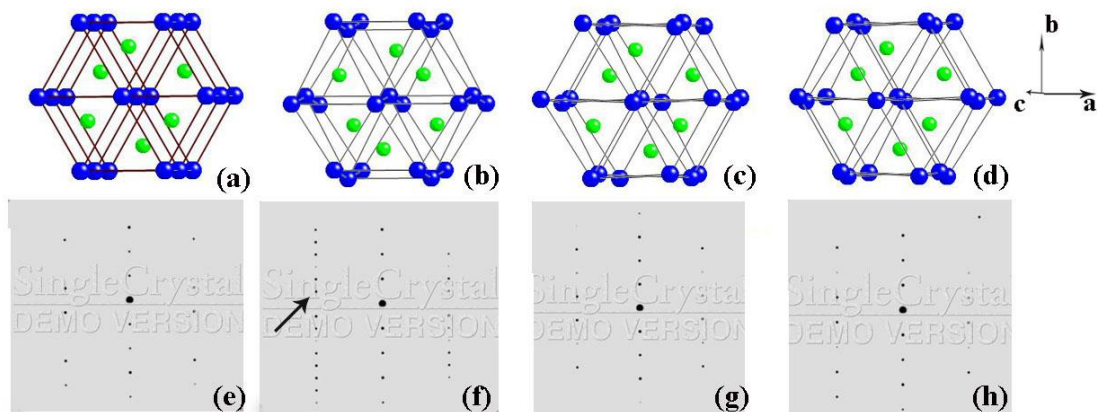


Fig. 4.9. (a) The atomic structure of hexagonal  $\alpha$ -MnAs seen from the  $[11\bar{2}9]$  zone axis; (b-d) the atomic structure of orthorhombic  $\beta$ -MnAs seen from (b) $[310]$ , (c)  $[61\bar{1}]$  and (d)

[611]. The zone axis here is reached by tilting the four crystals in Fig. 4.7 by  $12^\circ$  around  $b$  axis from the zone axis  $c$ . The simulated diffraction patterns in (e-h) correspond to the atomic structures in (a-d) respectively.

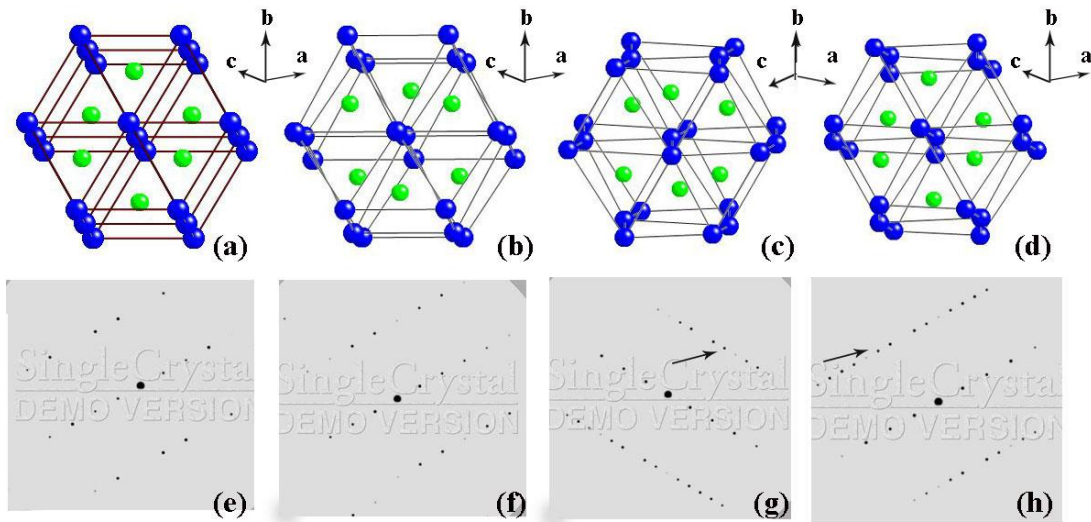


Fig. 4.10. (a) The atomic structure of hexagonal  $\alpha$ -MnAs seen from the  $[2\bar{1}\bar{1}9]$  zone axis; (b-d) the atomic structure of orthorhombic  $\beta$ -MnAs seen from (b)  $[51\bar{1}]$ , (c)  $[310]$  and (d)  $[310]$ . The zone axis here is reached by tilting the crystals in Fig. 4.7 from the zone axis  $c$  by  $10^\circ$  clockwise (except for  $\beta_2$ , it is  $10^\circ$  counterclockwise) around  $a$  axis and then  $6^\circ$  clockwise around  $b$  axis. The simulated diffraction patterns in (e-h) correspond to the atomic structures in (a-d) respectively.

For the cross-section specimen in Fig. 4.5, the initial zone axes for the four crystals are along the defined  $a$  axis. Along the initial zone axes, we can see some extra spots in the diffraction pattern of  $\beta_1$ -MnAs, but no difference among the patterns of  $\alpha$ ,  $\beta_2$ - and  $\beta_3$ -MnAs, as shown in Fig. 4.11. The situation is similar to that in Fig. 4.9. If no extra spots appear along the  $a$  axis, we can tilt the crystals by  $\pm 30^\circ$  around  $c$  axis to figure out it is  $\alpha$ -,  $\beta_2$ - or  $\beta_3$ -MnAs. As a similar conclusion with the one for the other cross-section specimen, from the practical point of view, if no extra spots appear when the crystals are along orientated from the  $a$  zone axis by  $\pm 12^\circ$  around  $b$  axis, or by  $\pm 10^\circ$  around  $a$  axis followed by  $\pm 6^\circ$  around  $b$  axis, the  $\alpha$ -MnAs is identified.

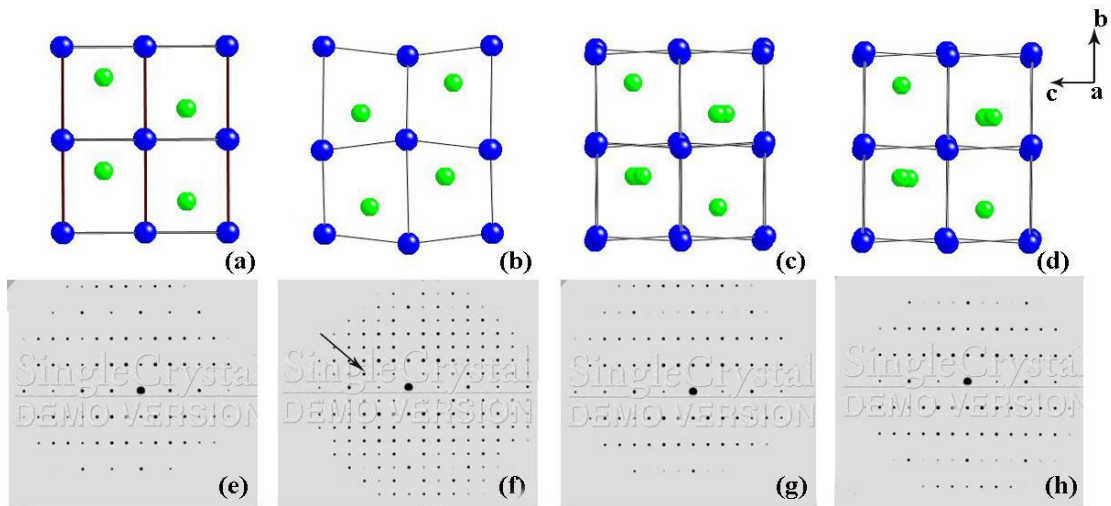


Fig. 4.11. (a) The atomic structure of hexagonal  $\alpha$ -MnAs seen from the  $[11\bar{2}0]$  zone axis; (b-d) the atomic structure of orthorhombic  $\beta$ -MnAs seen from (b)  $[010]$ , (c)  $[01\bar{1}]$  and (d)  $[011]$ . The zone axis here is just along the a axis. The simulated diffraction patterns in (e-h) correspond to the atomic structures in (a-d) respectively.

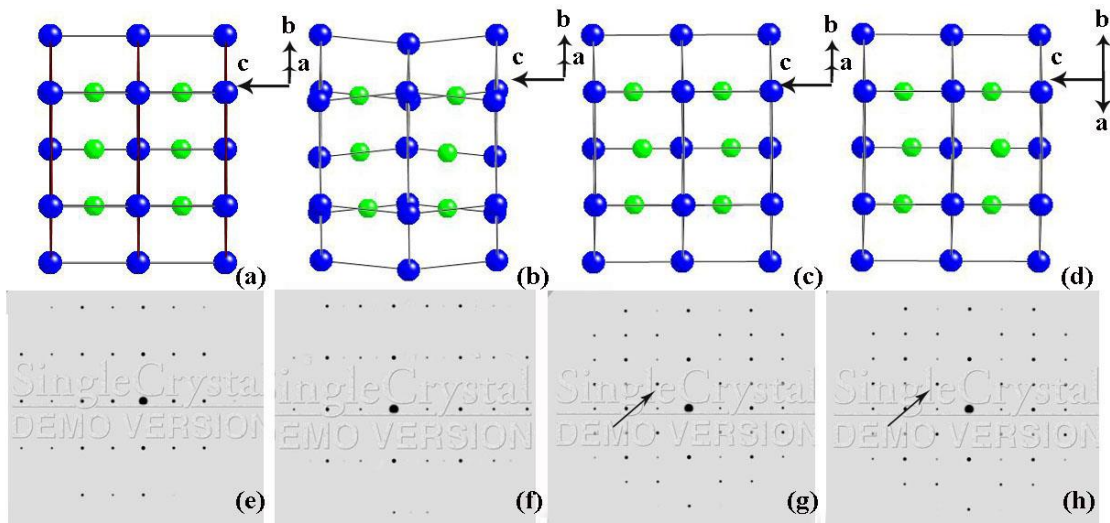


Fig. 4.12. (a) The atomic structure of hexagonal  $\alpha$ -MnAs seen from the  $[10\bar{1}0]$  zone axis; (b-d) the atomic structure of orthorhombic  $\beta$ -MnAs seen from (b)  $[03\bar{1}]$ , (c)  $[00\bar{1}]$  and (d)  $[001]$ . The zone axis here is reached by tilting the crystal from a axis by  $30^\circ$  counterclockwise around c axis (except for  $\beta_3$ , it is tilted by  $30^\circ$  clockwise). The simulated diffraction patterns in (e-h) correspond to the atomic structures in (a-d) respectively.

### 3. EMCD Study of magnetocrystalline anisotropy of $\alpha$ -MnAs

Now, we are able to clearly identify the two phases by TEM and we are firstly going to study the EMCD of the  $\alpha$ -phase.

#### 3.1 EMCD signal of $\alpha$ -MnAs at RT

##### 3.1.1 Acquisition of EMCD signal

The local magnetic information of MnAs epilayer was firstly investigated in the plan-view sample, on an area as the one shown in Fig. 4.13(a). The crystal was orientated along the specific zone axis  $[\bar{2}\bar{2}01]$ , and a diffraction pattern in the inset of Fig. 4.13(a) was acquired using selected area electron diffraction (SAED) technique. The diffraction pattern, as explained above, demonstrates that only the hexagonal  $\alpha$ -MnAs phase is present in this area.

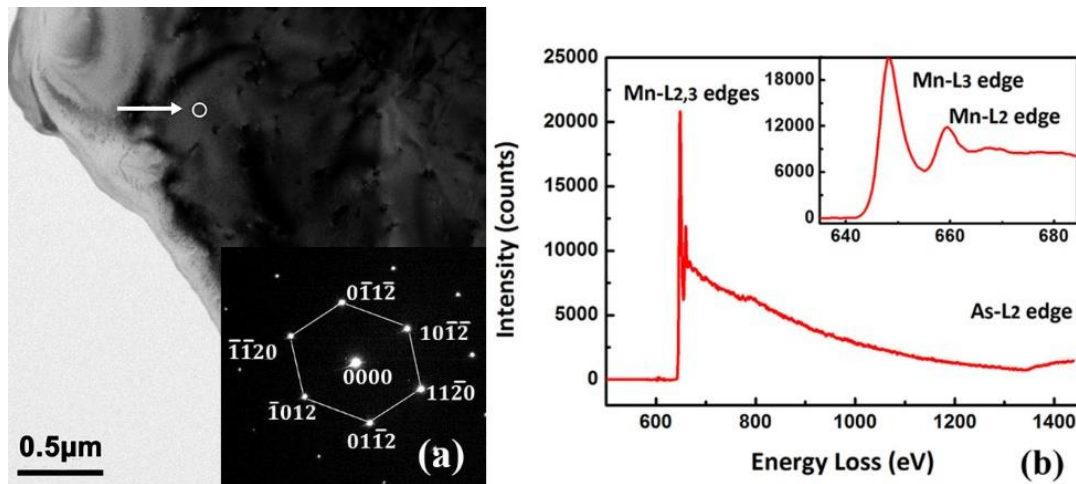


Fig. 4.13. (a) Bright field image of the plan-view sample of MnAs/GaAs(001) at RT and diffraction pattern acquired in the selected area along  $[\bar{2}\bar{2}0\bar{1}]$  zone axis in the inset. (b) Electron energy loss near edge spectrum of this area at RT.

EELS technique was then used to check the thickness and the elemental composition of the selected area. The relative sample thickness  $t/\lambda$ ,  $\lambda$  being the inelastic mean free path, is measured to be 0.41 in the example shown. No carbon and a negligible amount of oxygen, which reveal negligible traces of contaminations, have been detected

by EELS in all the areas analysed. Fig. 4.13(b) shows an EELS spectrum, with energy loss ranging from 500 eV to 1450 eV. Mn-L<sub>2,3</sub> and As-L<sub>2,3</sub> edges, respectively at 640 eV and 1323 eV are shown in the spectrum. No Ga edge has been detected. It means that the GaAs substrate layer in the plan-view sample is totally polished away, and only MnAs layer is preserved in this region. The enlarged near edge fine structures of the Mn-L<sub>2,3</sub> edge is shown in the inset of Fig. 4.13(b).

EMCD technique was then applied on the same area for which the phase, thickness and elemental composition have been previously specified. The MnAs layer was magnetized along the beam axis by the magnetic field as large as 2 T coming from objective lens. The crystal was reorientated from the zone axis  $[\bar{1}100]$  by several degrees to reach a two-beam configuration to minimize the n-beam dynamic interaction, in which only diffraction spot (11 $\bar{2}0$ ) was excited. We used LACDIF experimental setup to obtain a diffraction pattern with two spots in image plane, and applied ESI technique to record a raw data cube over the energy range from 630 eV to 670 eV. The spatial resolution reaches a few tens of nanometers.

The advantages of this ESI method compared to other recording methods are the ability to obtain a map of the dichroic signal and to correct for distortions or aberrations in a post-treatment process<sup>6</sup>. The distortions due to non-isochromaticity and spatial drift have dramatic effect on the EMCD signal. Non-isochromaticity is due to spectrometer aberrations that are adjusted by lenses but never perfectly compensated. It corresponds to the difference in energy from position to position in an EFTEM image. This aberration needs to be corrected to make sure we compare pixels recorded at the same energy inside a single energy window. Spatial drift is the movement of the image with respect to the CCD camera during the acquisition. It comes from the instabilities of the coils current in the microscope. Fig. 4.14 (a) shows a raw data cube with spatial drift and serious non-isochromaticity as an example. Two EELS spectra extracted from position 1 and position 2 are presented in Fig. 4.14(b). A shift of 2 eV between the two Mn-L<sub>3</sub> peaks originates from the non-isochromaticity, and the intensity difference existing in the energy range after Mn-L<sub>2</sub> edge is due to the spatial resolution. These two sources of distortions cannot be corrected by optimizing the experimental setup, while can be corrected in a post-treatment process with a home-made program in Digital Micrograph.

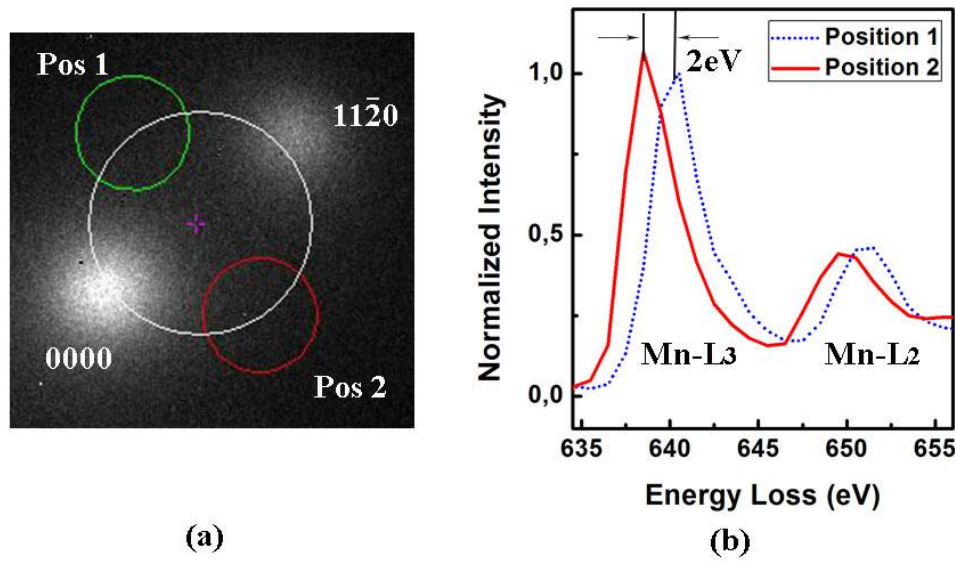


Fig. 4.14 (a) A raw data cube with spatial draft and non-isochromaticity. (b) Two EELS spectra detected from the position 1 and position 2 in (a); a shift of 2 eV between the two peaks is induced by the non-isochromaticity; there is still an intensity difference in the energy range after the Mn-L<sub>2</sub> edge, due to the spatial resolution.

Then two EELS spectra are extracted from a corrected data cube. However, the difference of the two spectra exists over the whole energy range from 630 eV to 670 eV. It is due to that it is hard to tilt the crystal to reach perfect two-beam condition experimentally. So in general, the two EELS spectra are normalized at the post-edge energy regions from 661 eV to 665 eV which is more than 10 eV away from the L<sub>2</sub> peak. The spectra over the energy range from 630 eV to 665 eV presented in Fig. 4.15(b) is cut from the original spectra, in order to emphasize the peaks and show readers the detail of spectra more clearly. The values of the signal difference (displayed in a black bold line in figure 4.15 (b) around the L<sub>2</sub> and L<sub>3</sub> peaks are opposite in sign, confirming magnetism of the detected sample.

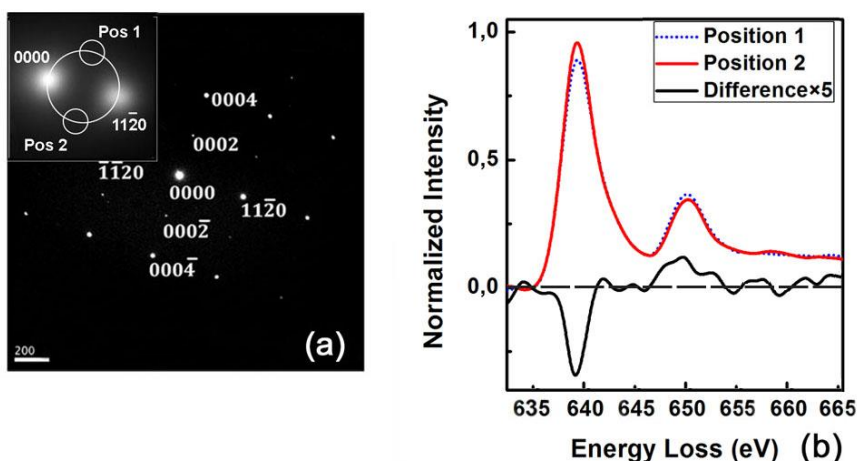


Fig. 4.15. (a) Diffraction pattern along the  $[\bar{1}100]$  zone axis at RT, and the inserts in (a) is the energy filtered diffraction pattern in two-beam condition; (b) EELS spectra acquired at RT from position 1 and 2, and difference spectrum multiplied by 5.

### 3.1.2 Application of EMCD sum rule

We are now going to apply sum rules to EMCD spectra for quantitative analysis. Formula in sum rules are available to calculate orbital and spin moments of magnetic samples from the integrated areas under  $L_2$  and  $L_3$  edge curves in EMCD spectra. For 3d transition metal ions or atoms, the EMCD sum rule has already been introduced and discussed in chapter I (Eq 1.14). Here I only rewrite the sum rule of moment ratio in Eq. (4.1). Several points are clarified here before giving the moment values. First, the validity and accuracy of sum rules are necessary to be considered. The XMCD  $\langle S_z \rangle$  sum rule strictly demands that the core spin-orbit splitting must be sufficiently large compared with other interactions including mainly the core-valence exchange interaction<sup>19</sup>. To be specific, Mn- $L_3$  and  $L_2$  edges have to correspond to pure  $2p_{3/2}$  and  $2p_{1/2}$  respectively. But in the real situation, the mixing between two p states exists due to 2p-3d exchange interaction for  $Mn^{2+}$ . In other words, there is an overlapping region in  $L_3$  and  $L_2$  edges. The effective spin moment of  $Mn^{2+}$  calculated with the  $\langle S_z \rangle$  sum rule is precise within approximately 30%<sup>20</sup>. That is why a correction factor of 1.47 is applied to the calculated value in Ref. 8. In fact, the overlapping region in  $L_3$  and  $L_2$  edges also exists in EELS, while the correction for EMCD spin sum rule is not going to be discussed in detail in this thesis, and all the values of orbital to spin moment ratio shown in the following are directly calculated from the EMCD sum rule without any additional correction. Second,



it is worth noting that an assumption of importance has been made to simplify the derivation of sum rules: all the magnetic moments in the detected sample must be aligned along the z-axis, which is perpendicular to the plane defined by the diffusion vectors  $\mathbf{q}$  and  $\mathbf{q}'$  (cf. Fig. 1.10(b)). In standard TEM operating modes, the sample is under an external magnetic field as large as 2 T, due to the objective lens, so that the magnetic moments should be aligned along the magnetic field. The magnetic field is parallel to the optical axis, which is also the z-axis mentioned above. If the precondition is not met, what is obtained with sum rules is just a projection of magnetic moment on the z-axis.

$$\frac{\int_{L_3} (\sigma_2 - \sigma_1) dE - 2 \int_{L_2} (\sigma_2 - \sigma_1) dE}{\int_{L_2+L_3} (\sigma_2 - \sigma_1) dE} = \frac{4\langle S_z \rangle + 14\langle T_z \rangle}{3\langle L_z \rangle} \approx \frac{2m_s}{3m_l} \quad (4.1)$$

For the ferromagnetic  $\alpha$ -MnAs, it is easy to achieve magnetic saturation in TEM, since the saturation field along easy axis is less than 100 mT. However in practice, the easy axis of the film is not necessarily parallel to the magnetic field in TEM, but always tilted away from it to reach a two-beam condition. So it is of help to understand magnetic anisotropy field of MnAs/GaAs(001) thin film and determine the applied magnetic field required to saturate the sample along any axis.

As mentioned before, the MnAs film on GaAs(001) substrate has a magnetic hard axis along [0001], and an easy axis along [11 $\bar{2}$ 0] in the growth plane ( $\bar{1}$ 100). The magnetocrystalline anisotropy is the major contribution to the in-plane magnetic anisotropy. Thus, the in-plane magnetic anisotropy field  $H_k$  can be described, according to Ref. [7], as  $H_k = -2(K_1 + 2K_2)/\mu_0 M_s$ , where  $K_1$  and  $K_2$  is the first and second order of anisotropy constant respectively,  $\mu_0$  is vacuum permeability, and  $M_s$  is the saturation magnetization. The values of  $K_1 = -7.9 \times 10^5 \text{ J/m}^3$ ,  $K_2 = 1.1 \times 10^5 \text{ J/m}^3$ , and  $M_s = 0.65 \times 10^6 \text{ A/m}$  around RT<sup>8</sup> were used to estimate  $B_k = H_k \mu_0 = 1.75T$ . The reported values of in-plane magnetic anisotropy field of 2 T is consistent with our calculated value. The film also has an out-of-plane magnetic anisotropy, but weaker than the in-plane one, which means the saturation field along the [0001] hard axis is larger than that along the out-of-plane ( $\bar{1}$ 100) intermediate axis. The magnetic field from the objective lens being measured to be 2 T in our experimental conditions, it is high enough to saturate the sample regardless of the sample orientations inside the TEM.

We then apply the sum rule to the signal shown in Fig. 4.15(b). The  $m_l/m_s$  ratio can be extracted straightforwardly when the scattering conditions are properly set. In our case, the spectra were integrated within the energy windows [636 eV-644 eV] for Mn-L<sub>3</sub> edge and [648 eV-656 eV] for Mn-L<sub>2</sub> edge. The two windows were selected to cover the whole ranges of L<sub>2</sub> and L<sub>3</sub> edges respectively. The  $m_l/m_s$  ratio deduced is of  $0.08 \pm 0.04$ . It is known that the signal obtained with EMCD technique depends sensitively on many factors, like sample thickness, detector position, aperture size, etc. But for the ratio of orbital moment to spin moment, the measurement result is not affected by these factors.

There are five main sources of statistical error.

- (1) Not perfectly orientated sample and thus contribution of complex dynamic interaction.
- (2) Position, shape and size of the integration window around the so-called Thales circle position. Here I have used a round aperture on the Thales circle as recommended in particular in the paper from J. Verbeeck et al.<sup>9</sup> I have tested that small variations in its position and size do not qualitatively change the spectra.
- (3) The noise of the spectra themselves. More than 60 data cubes were acquired and 5-10 less noisy data cubes have been chosen for sum rule extraction of the  $m_l/m_s$  ratios. No filter for data smoothing was applied before applying sum rules to the spectra. The smoothed curves in Fig. 4.15 is just for better demonstration. The error on the quantitative determination strongly depends on the quality of the original spectra.
- (4) The post edge energy window for the normalization. Small changes of post-edge energy region selected for normalization also affect the value of the  $m_l/m_s$  ratio. For example, the varying  $m_l/m_s$  values in table 4.1 are obtained from the same data cube but with different post-edge normalization window. An error of  $\pm 0.01$  is estimated. This energy window width of 4 eV is selected because we have the most stable results with it.

Table 4.1. Varying  $m_l/m_s$  values with the post-edge normalization window in different energy regions.

Post-edge normalization window (eV)	<b>661-665</b>	<b>660-664</b>	<b>659-663</b>	<b>658-662</b>
-------------------------------------	----------------	----------------	----------------	----------------

$m_l/m_s$ value	0.07	0.08	0.07	0.09
-----------------	------	------	------	------

(5) Plural scattering. The plural scattering, which may noticeably influence the result<sup>10</sup>, was not removed in our data treatment. It introduces non-negligible error.

The error of  $m_l/m_s$  is finally estimated by calculating the statistic standard deviation  $\sigma = \sqrt{\sum(x - \bar{x})^2/n}$  for selected data cubes. The magnetic moment ratio of Mn atom in MnAs measured by EMCD technique has not been reported before.

### 3.2 Anisotropic EMCD signal

#### 3.2.1 Acquisition of EMCD signal

It has been mentioned for more than one time that  $\alpha$ -MnAs thin layer on GaAs(001) substrate has a large magnetocrystalline anisotropy. The external magnetic field of 2 T is enough to saturate the sample along hard axis [0001] at RT, but only 1 T along intermediate axis  $[\bar{1}100]$ <sup>11</sup> and 100 mT along easy axis  $[11\bar{2}0]$  are needed to saturate the layer. In principle, the spin moments are nearly isotropic and all of them can be aligned when the sample is magnetically saturated along z-axis in the TEM, but there is still charge anisotropy of the valence states involved in the core excitation process through the spin-orbit coupling<sup>12</sup>. In hexagonal MnAs, the orbital angular momentum of  $Mn^{2+}$  is partly frozen due to the crystal field. The projection of orbital momentum  $\langle L_z \rangle$  varies with the sample orientation under the fixed magnetic field along z-axis. As a result, the measured EMCD signal and the obtained moment ratio cannot be free from the sample orientation, but are anisotropic.

Fig. 4.16 shows the result of EMCD experiment performed on the cross-section specimen with the interface parallel to the easy axis  $[11\bar{2}0]$ . The crystal is orientated along the axis near the zone axis [0001]. This direction is perpendicular to the intermediate axis and the spot (1010) is selected in Fig. 4.16(a). Fig. 4.16(b) displays the EMCD signal. We then apply the sum rule to the signal, and the  $m_l/m_s$  ratio is of  $0.06 \pm 0.04$ . When compared with the experimental value of  $0.08 \pm 0.04$  obtained around intermediate axis  $[\bar{1}100]$ , it is found that the ratio along the axis around hard axis is lower. In addition, the experimental value obtained around easy axis  $[11\bar{2}0]$  is measured to be

$0.09 \pm 0.04$ , which is 0.01 larger than the value obtained around intermediate axis. The experimental result is shown in Fig. 4.17.

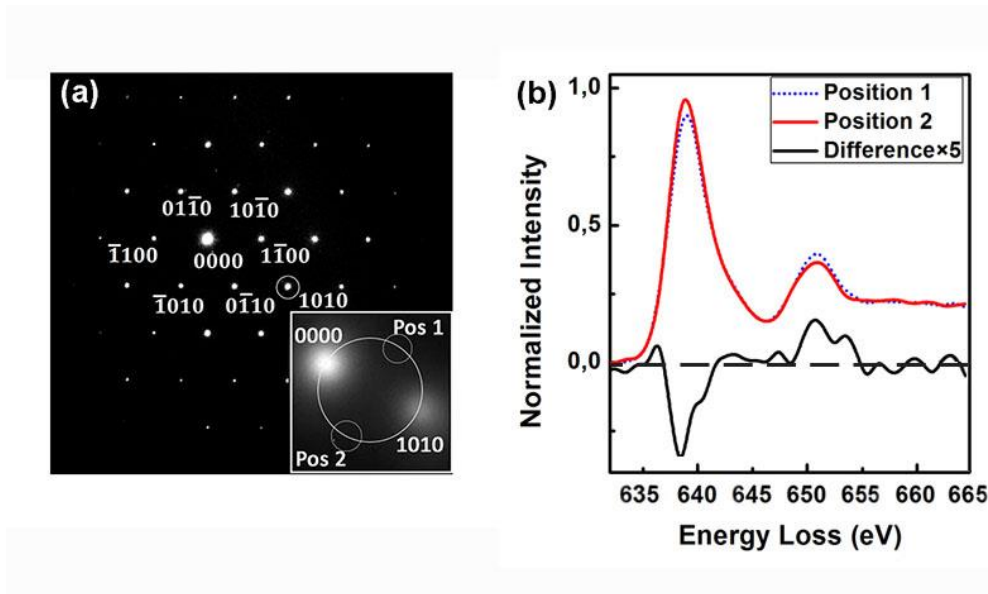


Fig. 4.16. (a) Diffraction pattern along  $[0001]$  zone axis at RT, and the inserts in (a) is the energy filtered diffraction pattern in two-beam condition; (b) EELS spectra acquired at RT from position 1 and 2 as well as the spectra difference multiplied by 5.

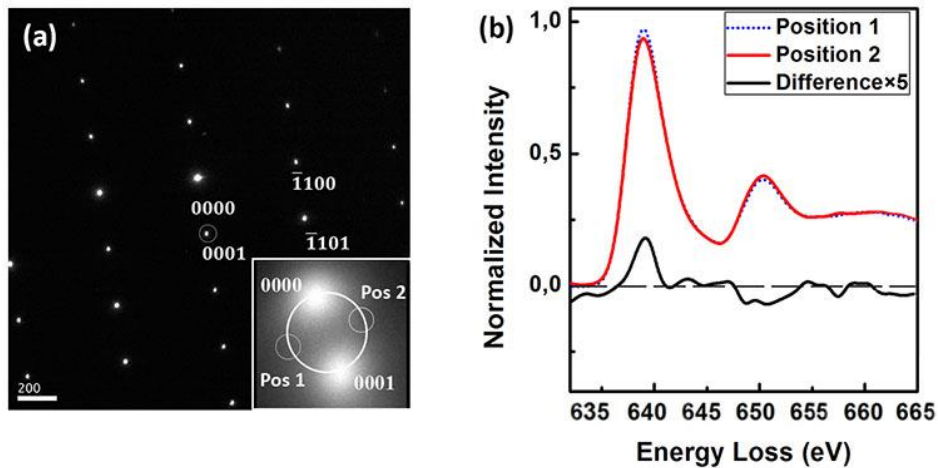


Fig. 4.17. (a) Diffraction pattern along  $[11\bar{2}0]$  zone axis at RT, and the inserts in (a) is the energy filtered diffraction pattern in two-beam condition; (b) EELS spectra acquired at RT from position 1 and 2 as well as the spectra difference multiplied by 5.

### 3.2.2 Comparison of EMCD results with XMCD and theoretical results

Correspondingly, the density functional theory (DFT) calculations (cf. Appendix IV) also give different values in different situations:  $m_l/m_s = 0.008$  when the spin and orbital moments are coupled along easy axis;  $m_l/m_s = 0.005$  when along hard axis;  $m_l/m_s = 0.008$  when along intermediate axis. These information are gathered in table 4.2, where the XMCD experimental value of  $0.03 \pm 0.02$  obtained along easy axis at around RT is extracted from Ref. [8]. From table I, it can be seen that the experimental EMCD value of  $0.09 \pm 0.04$  for easy axis measurement is larger than the XMCD value of  $0.03 \pm 0.02$  obtained along the same axis. Data correction of spin moment with a constant of 1.47 has been proceeded to compensate the effect of the mixing between  $L_2$  and  $L_3$  edges for the XMCD result and not for EMCD ones. The experimental measurements, in particular when compared to the theoretical one, can be considered to be of the same order of magnitude, largely far from the theoretical ones. The discrepancy between the experimental and theoretical results may partly originate from the simplification of theoretical calculation. The theoretical calculations are based on the atomic ground state at  $T=0$  K, and are performed for d-electrons inside atomic spheres only, whereas the experiment was made at RT where other where other excited states can mix into the ground state due to thermal motion. In addition, the sample is orientated a few degrees away from the zone axis to a two-beam condition in EMCD experiment, so the spin-orbit coupling is not exactly the same as set in the theoretical calculation. Taking into account these weaknesses, relative EMCD variations observed were expected from the predicted ones. So we can say that the EMCD technique is an interesting technique to study anisotropy of ferromagnetic material. That is to say, if the diffraction spot in two-beam condition is selected from a different diffraction pattern due to different sample orientation, the measured ratio may change. So making clear the sample orientation or the selected diffraction spot is necessary to understand the measured dichroism signal and the moment information it carries.

*Table 4.2. Comparison of the orbital-to-spin moment ratios deduced from sum rules along easy, hard and intermediate  $\alpha$ -MnAs axis obtained with EMCD and XMCD technique (Ref. 8), and DFT calculations are also provided. EMCD values along hard and easy axis are obtained in TEM cross-section configuration and that obtained along intermediate axis is in plan-view one.*

$m_l/m_s$	Hard axis [0001]	Intermediate axis [ $\bar{1}100$ ]	Easy Axis [ $11\bar{2}0$ ]
EMCD	$0.06 \pm 0.04$	$0.08 \pm 0.04$	$0.09 \pm 0.04$
XMCD	–	–	$0.03 \pm 0.02$ <sup>a</sup>
DFT	0.005	0.008	0.008

<sup>a</sup>Reference 8

#### 4. In-situ observation of phase transition

During the phase transition, the ferromagnetic  $\alpha$ -MnAs gradually transforms into paramagnetic  $\beta$ -MnAs with temperature rising, until the temperature  $T_c$  of about 45°C, where no  $\alpha$ -MnAs is left. In this section, I am going to present an in-situ observation of the breaking of ferromagnetic order during phase transition using EMCD technique. In addition, an in-situ observation of the phase transition using the electron holography technique is also presented in the following, for the interest of investigating if there is significant difference between the phase transition processes during heating and cooling.

##### 4.1 In-situ observation of crystallographic Transition

When the  $\alpha$ -MnAs is transformed into  $\beta$ -MnAs, some extra spots appear at specific positions in the diffraction patterns along some zone axis, demonstrating the crystallographic transition occurred. On the very same area of identified  $\alpha$ -MnAs, the crystallographic change upon temperature rise is monitored by observing the evolution of diffraction pattern along  $[\bar{2}20\bar{1}]$  zone axis, which corresponds to  $[\bar{1}\bar{3}1]$  zone axis in orthorhombic  $\beta$ -MnAs.

Fig. 4.18 demonstrates the evidence of atomic structure evolution during phase transition observed in the plan-view specimen. The left-hand column shows the images recorded at RT, and at the right those recorded at 50°C. The selected area is pointed in Fig. 4.18(a) and (c) by white circles indicated by arrows. No visible extra spots are observed in the diffraction pattern along the  $[\bar{2}20\bar{1}]$  zone axis in Fig. 5(b), identifying that substantially all the MnAs in the selected area is hexagonal  $\alpha$ -MnAs at RT. During the temperature increase, from RT to 50°C, there is a continuous variation of the image

contrast in the low-magnification bright-field image. When the sample reaches 40°C, the previously mentioned extra spots start to be noticeable in the diffraction pattern along  $[\bar{2}20\bar{1}]$ , verifying that the transition to orthorhombic  $\beta$ -MnAs in the selected area has happened. When the temperature approaches 50°C, the intensity of the extra spots is stable, and so for the contrast in low-magnification image. The full duration of the temperature increase up to stabilization is about 5 minutes. The final low-magnification image and diffraction pattern acquired at 50°C are presented in Fig. 4.18(c) and (d). Substantially, all the  $\alpha$ -MnAs in the selected area at 50°C is assumed to be transformed into  $\beta$  phase.

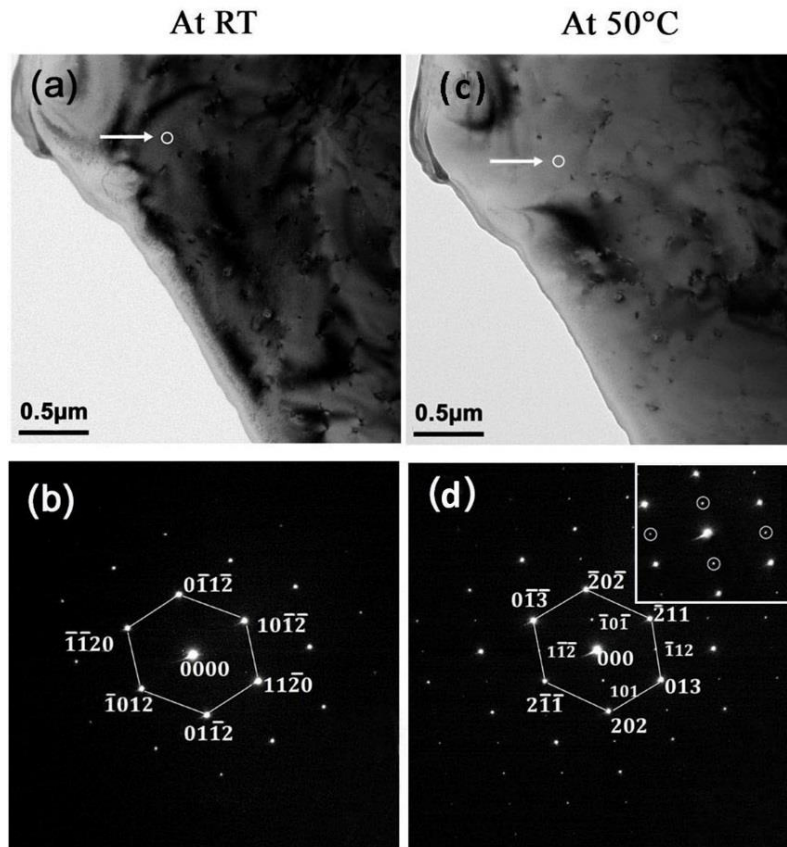


Fig. 4.18. Low magnification bright-field image of MnAs thin film, (a) at RT, and (c) at 50 °C. (b) Diffraction pattern at RT along the  $[\bar{2}20\bar{1}]$  zone axis; (d) Diffraction pattern at 50°C along the  $[\bar{1}\bar{3}1]$  zone axis.

## 4.2 Temperature dependent EMCD

On the same area, the EMCD signals were acquired at RT and 50°C. In the EMCD experiment, the  $\alpha$ -MnAs crystal at RT was orientated along the zone axis of  $[\bar{1}100]$  (Fig. 4.19(a)), and then tilted several degrees to reach two-beam configuration where only diffraction spot (11 $\bar{2}0$ ) was excited. At 50°C, the transformed  $\beta$ -MnAs crystal was orientated along  $[0\bar{3}1]$  zone axis (Fig. 4.19(c)), which was parallel to the  $\alpha$ -MnAs  $[\bar{1}100]$  direction, and then reached the same two-beam condition where only diffraction spot (013) was excited. The similarity of the two diffraction patterns is obviously seen in Fig. 4.19(a) and (c). Thus, the similar diffraction spot is selected as shown in the insets. The dynamic interaction of the electron beam in the two cases are very analogous, thus it can be excluded as an influence factor when comparing dichroism signals obtained at RT and 50°C. Fig. 4.19(b) shows an obvious dichroism signal at RT, while the dichroism signal disappears after the phase transition. Sum rules have then been applied to quantitatively analyze the change in the magnetic moment with phase transition.

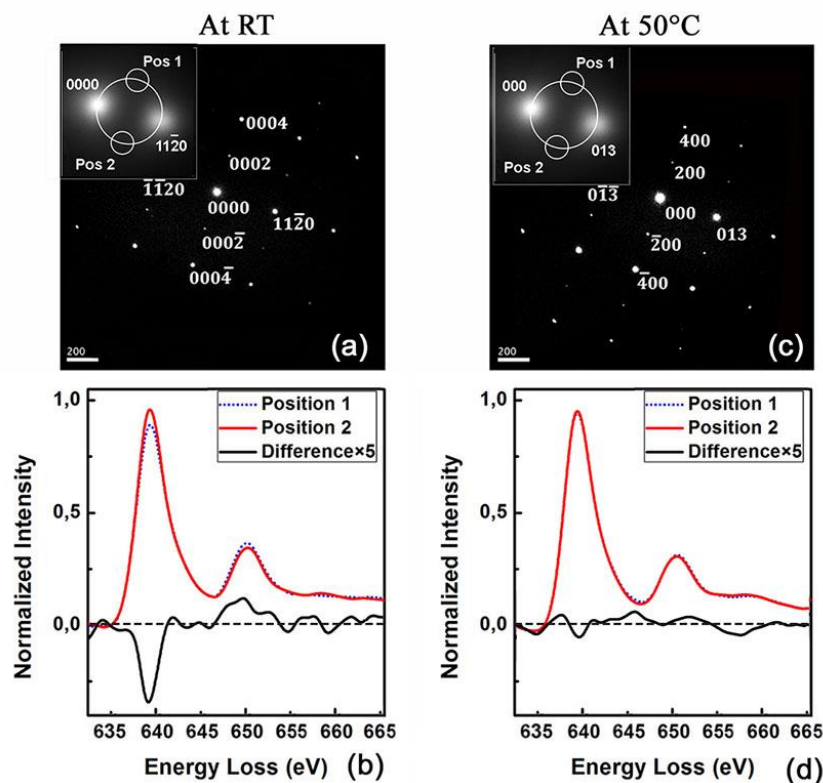


Fig. 4.19. Diffraction pattern along (a)  $[\bar{1}100]$  at RT and (c)  $[0\bar{3}1]$  at 50°C. The insets in (a) and (c) are the energy filtered (energy loss from 635-660eV around Mn- $L_{2,3}$  edges) diffraction patterns in two-beam condition. EELS spectra are acquired at position 1 and 2 as well as the spectra difference multiplied by 5 (b) at RT, and (d) at 50 °C.



The experimental EMCD result of  $\alpha$ -MnAs acquired along  $[\bar{1}100]$  zone axis at RT has been discussed in section 3. In the case of  $\beta$ -MnAs, it is more complicated. There is even no consensus on its magnetic nature yet. Theoretical and experimental evidences can be found to support both paramagnetism and antiferromagnetism<sup>13</sup>. If it is paramagnetic, under the magnetic field of 2 T in TEM, the disorderly arranged magnetic moments have the tendency to align long  $z$  axis. Note that there is intrinsic net magnetic moment of Mn atom, and the magnetization projected along the  $z$ -axis is not zero under magnetic field, therefore the dichroism signal  $\sigma_2 - \sigma_1$  should theoretically appear, according to Eq. 4.2, where  $N_h$  is the number of holes in the  $d$  bands and  $K$  contains all the information related to the dynamical diffraction effects. But no dichroism signal appearing in Fig. 4.19(b) is not a sufficient evidence to reject its paramagnetism, because the magnetization of  $\beta$ -MnAs under applied magnetic field of 2 T is much smaller than the one of  $\alpha$ -MnAs. In Ref. [14], the magnetization of  $\alpha$ -MnAs around RT is almost 10 times smaller than that of  $\alpha$ -MnAs under 2 T. Thus, the dichroism signal of paramagnetic  $\beta$ -MnAs may be too weak to be detected by EMCD technique, due to the insufficient signal-to-noise ratio. On the other side, if  $\beta$ -MnAs is antiferromagnetic, the magnetization is even smaller, and the dichroism signal is still more difficult to obtain. Another possible explanation for antiferromagnetic behavior is that the dichroism signal from the parallel moments will be in opposite sign with the signal from antiparallel moments. If the total moments are zero, their contribution to the dichroism signal will cancel each other out. With the disappearance or largely weakening of the dichroism signal, the ferromagnetic order is seen to be broken following the crystallography transition.

$$\langle S_z \rangle = \frac{3N_h \int_{L_3} (\sigma_2 - \sigma_1) dE - 2 \int_{L_2} (\sigma_2 - \sigma_1) dE}{2K \int_{L_2+L_3} (\sigma_2 + \sigma_1) dE} \quad (4.2)$$

### 4.3 Temperature dependent holography

Electron holography (EH) is a technique which allows to record local magnetization map in a TEM<sup>15,16</sup>. It is interesting to investigate if there is significant difference between the phase transitions during heating and cooling processes, by mapping the temperature-dependent magnetic configuration of the MnAs thin film with the EH technique. Our EH experiment was done on a cross-section specimen with a zone

axis of [0001]. This specimen is a little different from the one previously described in section 4.1 and 4.2. First, this specimen was thinned by the focused ion beam (FIB) technique. Ink and Pt layers were deposited on the MnAs layer to protect it from the possible damage during FIB thinning. Second, the thickness of the MnAs thin film for this FIB specimen is 180nm instead of 150nm for the previous one. Moreover, Even so, the EH experiment results presented in this section are still believed to be of high value, in terms of corroborating the EMCD results and offering a local magnetization map, as the growth condition and epitaxial orientation of the MnAs/GaAs(001) heterostructures are always the same. Before the holography experiment, the MnAs layer in the FIB specimen was at first saturated by the magnetic field from the objective lens. Then the objective lens was switched off and the Lorenz mode was on. In the very same area, holograms were recorded every 1°C between 23°C and 50°C during cooling and heating process.

From each hologram, images of phase and amplitude can be obtained. From the phase image, it is possible to extract the local magnetic induction. However, the total phase shift is generally due to both electrostatic contributions  $\Phi_{MIP}$  and magnetic contribution  $\Phi_{MAG}$ , given  $\Phi = \Phi_{MIP} + \Phi_{MAG} = C_e \int V dz - \frac{e}{\hbar} \int B dz$ . Fortunately the sign of  $\Phi_{MAG}$  value will change if the sample magnetization is reversed, but  $\Phi_{MIP}$  will remain the same<sup>17</sup>. Therefore the commonly used method is that two holograms are recorded under opposite magnetization directions and then subtracted from each other to remove the electrostatic contribution  $\Phi_{MIP}$ <sup>18</sup>. For our sample, the method to extract  $\Phi_{MAG}$  is a little different. The reference phase image obtained at 50°C carries only electrostatic information, so the magnetic contribution  $\Phi_{MAG}$  in other phase images can be extracted by subtracting each phase image from the reference one.

A phase image with only magnetic contribution, extracted from a hologram acquired at room temperature, is shown in Fig. 4.20. Fringes within the MnAs layer along x direction indicate a non-zero x component of magnetization. The continuous fringes in this image indicate that only the  $\alpha$ -MnAs, which is ferromagnetic, exists in the selected area at room temperature. Another phase image acquired at 43°C is given in Fig. 4.21 as a comparison to Fig. 4.20. Few fringes are presented in Fig. 4.21 and in some areas there is even no color variation along the y direction. It indicates that the non-ferromagnetic  $\beta$ -MnAs coexists with the ferromagnetic  $\alpha$ -MnAs, and the magnetization of the  $\alpha$ -MnAs is smaller at 43°C.

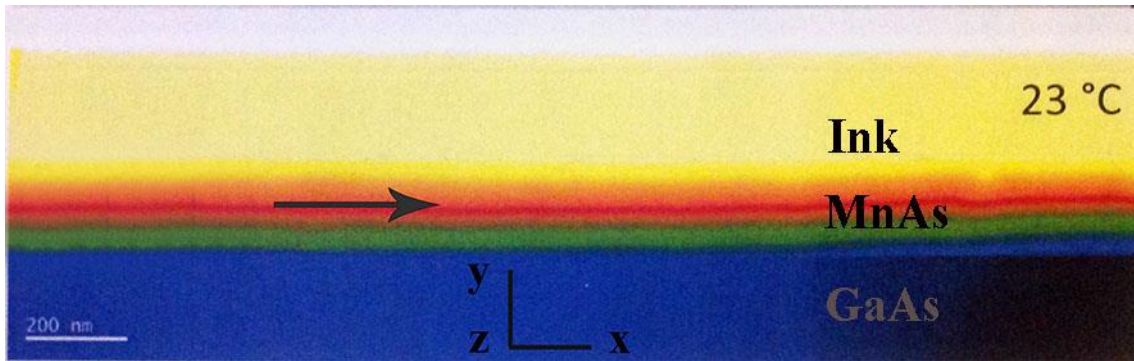


Fig. 4.20. A phase image extracted from a hologram which was acquired at room temperature. The arrow represents the magnetization direction.

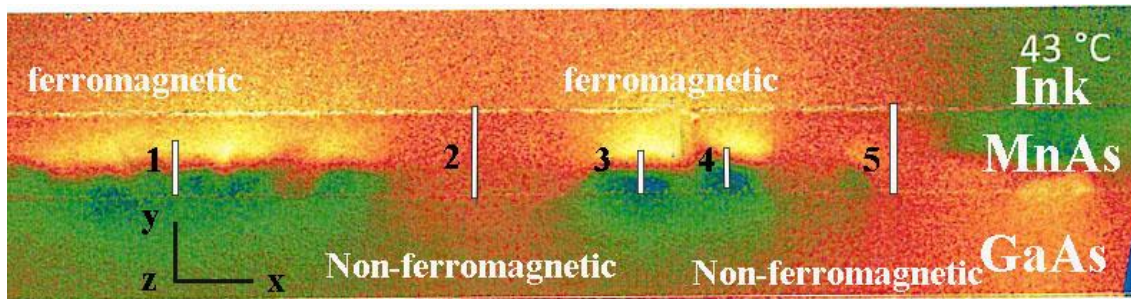


Fig. 4.21. A phase image extracted from a hologram acquired at 43°C. The color variation along the y direction can be seen in area 1, 3, 4, but not in area 2 and 5, indicating the non-ferromagnetic  $\beta$ -MnAs coexists with the ferromagnetic  $\alpha$ -MnAs.

Fig. 4.22 displays a series of phase images acquired in both the heating and cooling processes. We can compare the images acquired at the same temperature in different processes. From Fig. 4.22, we can see that the magnetic configurations in the left and right columns are very similar. As a conclusion, difference during the phase transitions in the heating and cooling processes, no significant difference is visible in the magnetization configuration maps acquired using EH technique.

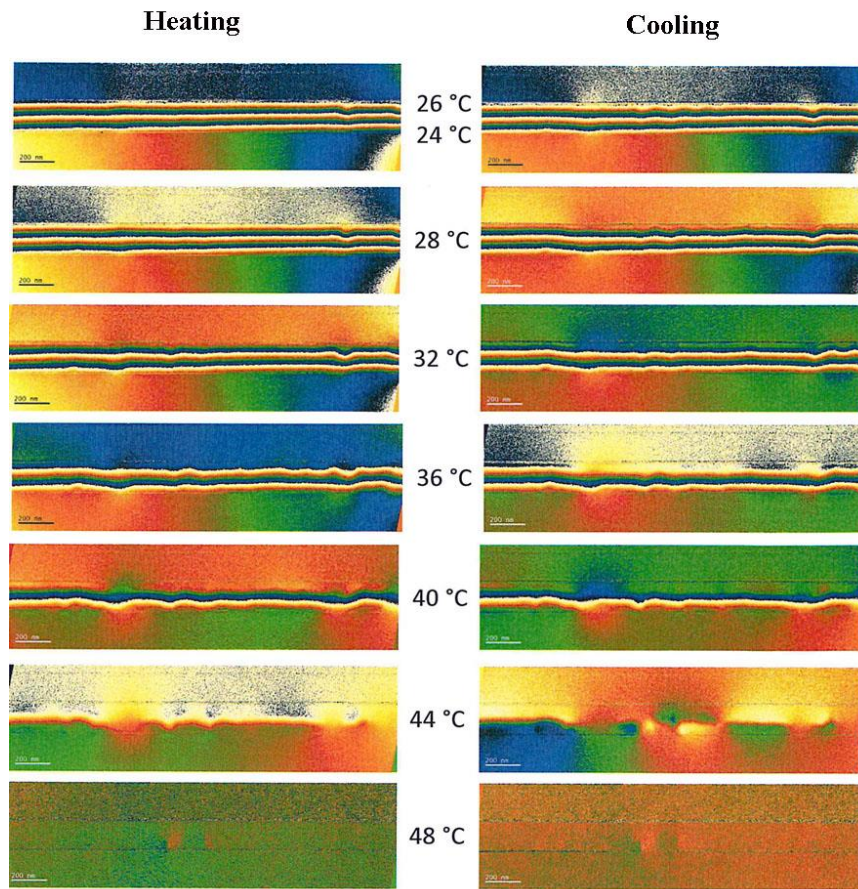


Fig. 4.22. Phase images extracted from holograms acquired at different temperatures in the heating and cooling processes. The images corresponding to the same temperature is put together for better comparison.

Actually more interesting things are found in this temperature-dependent EH experiment. For example, in the heating process, the phase transition from the ferromagnetic MnAs to non-ferromagnetic MnAs always happens initially in the area close to the interfaces between the MnAs layer and the GaAs substrate and Ink layers, and then happens in the middle area. The same thing occurs in the cooling process. By temperature-dependent electron diffraction, we make sure that the non-ferromagnetic MnAs initially appearing in the area near to the interfaces is  $\beta$ -MnAs. We can say that the phase transition between  $\alpha$ - and  $\beta$ -MnAs is inhomogeneous within the whole MnAs layer. Then a question arises: why the inhomogeneous transition happens in the cross-section specimen of MnAs/GaAs(001)? The surface effect and the interface effect close to the substrate or dislocations may be the explanation. We are still working on the EH experimental results, and more interesting phenomena will be revealed and explained.

## 5. Conclusion

In conclusion, the structural and magnetic properties of MnAs/GaAs(001) are studied mainly with TEM techniques in this chapter IV. At first, techniques such as XRD, MFM, HRTEM are used to give a general idea about the sample growth, crystal orientation, topography, etc. By electron diffraction, the  $\alpha$ - and  $\beta$ -MnAs can be distinguished. The local magnetic moment information of both the two phases is obtained with EMCD technique. The application of EMCD sum rules to the dichroism signal obtained from the identified hexagonal ferromagnetic  $\alpha$ -MnAs is discussed, and it is verified that the EMCD signal and the measured magnetic moment ratio are anisotropic for the magnetic anisotropic materials. In-situ observation of the phase transition in MnAs thin film is also presented in this chapter when the film is heated from RT to 50°C in TEM. The phase transition from  $\alpha$ -MnAs to  $\beta$ -MnAs is verified by the crystallographic transition from hexagonal structure to orthorhombic one, and the EMCD signal acquired before and after crystallographic transition shows the breaking of the ferromagnetic order during phase transition. Additionally, an EH experiment provides the temperature-dependent magnetization configuration of the MnAs film in both heating and cooling processes. From the magnetization configuration with in a high spatial resolution down to 2 nm, some interesting phenomena, for instance the inhomogeneous phase transition, are revealed. This work is still in progress.

## Bibliography

1. Breitwieser, R. *et al.* Phase transition and surface morphology of MnAs/GaAs(001) studied with in situ variable-temperature scanning tunneling microscopy. *Phys. Rev. B* **80**, 045403 (2009).
2. Arai, T., Suzuki, M., Ueno, Y., Okabayashi, J. & Yoshino, J. Structure transition between two GaAs(0 0 1)-c(4×4) surface reconstructions in As<sub>4</sub> flux. *J. Cryst. Growth* **301–302**, 22–25 (2007).
3. Mohanty, J. *et al.* Variable-temperature micromagnetic study of epitaxially grown MnAs films on GaAs(001). *Appl. Phys. A* **77**, 739–742 (2003).
4. Rungger, I. & Sanvito, S. Ab initio study of the magnetostructural properties of MnAs. *Phys. Rev. B* **74**, 024429 (2006).
5. Däweritz, L. Interplay of stress and magnetic properties in epitaxial MnAs films. *Rep. Prog. Phys.* **69**, 2581 (2006).
6. Gatel, C., Warot-Fonrose, B. & Schattschneider, P. Distortion corrections of ESI data cubes for magnetic studies. *Ultramicroscopy* **109**, 1465–1471 (2009).
7. Physics of Magnetism and Magnetic Materials | K.H.J Buschow | Springer. Available at: <http://www.springer.com/us/book/9780306474217>. (Accessed: 1st November 2015)
8. Wikberg, J. M. *et al.* Magnetocrystalline anisotropy and uniaxiality of MnAs/GaAs(100) films. *Phys. Rev. B* **83**, 024417 (2011).
9. Verbeeck, J. *et al.* Optimal aperture sizes and positions for EMCD experiments. *Ultramicroscopy* **108**, 865–872 (2008).
10. Ruzs, J. *et al.* Influence of plural scattering on the quantitative determination of spin and orbital moments in electron magnetic chiral dichroism measurements. *Phys. Rev. B* **83**, 132402 (2011).
11. Manago, T., Kuramochi, H. & Akinaga, H. Thickness dependence of magnetic domains of MnAs films. *Surf. Sci.* **600**, 4155–4159 (2006).
12. Aken, P. A. van & Lauterbach, S. Strong magnetic linear dichroism in Fe L 23 and O K electron energy-loss near-edge spectra of antiferromagnetic hematite  $\alpha$ -Fe<sub>2</sub>O<sub>3</sub>. *Phys. Chem. Miner.* **30**, 469–477 (2003).
13. Yamaguchi, H. *et al.* From ferro- to antiferromagnetism via exchange-striction of MnAs/GaAs(001). *EPL Europhys. Lett.* **72**, 479 (2005).
14. Ney, A. *et al.* Magnetic out-of-plane component in MnAs/GaAs(001). *Appl. Phys. Lett.* **83**, 2850–2852 (2003).

15. Javon, E., Gatel, C., Masseboeuf, A. & Snoeck, E. Electron holography study of the local magnetic switching process in magnetic tunnel junctions. *J. Appl. Phys.* **107**, 09D310 (2010).
16. Biziere, N. *et al.* Imaging the Fine Structure of a Magnetic Domain Wall in a Ni Nanocylinder. *Nano Lett.* **13**, 2053–2057 (2013).
17. Tonomura, A., Matsuda, T., Endo, J., Arii, T. & Mihama, K. Holographic interference electron microscopy for determining specimen magnetic structure and thickness distribution. *Phys. Rev. B* **34**, 3397–3402 (1986).
18. Dunin-Borkowski, R. E., McCartney, M. R., Kardynal, B. & Smith, D. J. Magnetic interactions within patterned cobalt nanostructures using off-axis electron holography. *J. Appl. Phys.* **84**, 374–378 (1998).
19. Teramura, Y., Tanaka, A. & Jo, T. Effect of Coulomb Interaction on the X-Ray magnetic Circular Dichroism Spin Sum Rule in 3 d Transition Elements. *J. Phys. Soc. Jpn.* **65**, 1053–1055 (1996).
20. Piamonteze, C., Miedema, P. & de Groot, F. M. F. Accuracy of the spin sum rule in XMCD for the transition-metal L edges from manganese to copper. *Phys. Rev. B* **80**, 184410 (2009).

## Chapter V

### Experimental Results of Epitaxial DyFe<sub>2</sub>/YFe<sub>2</sub> Superlattices

---

As mentioned in chapter III, the alloys, compounds or other systems consisting of rare earth (RE) and 3d transition metal (TM) are of high interest for their current and potential applications in permanent magnets and magnetic recording media<sup>1-2</sup>. In recent decades, X-ray Magnetic Circular Dichroism (XMCD) technique has been commonly applied to these materials to separately probe TM 3d moment and RE 4f moment, so as to reveal the coupling behavior and the origin of some properties<sup>3,4,5</sup>. As a counterpart of synchrotron-based XMCD, Energy-loss Magnetic Chiral Dichroism (EMCD) based on transmission electron microscopy (TEM) is also a technique used to locally characterize the element-specific orbital and spin moments with applying sum rules<sup>6,7</sup>. Complementary to XMCD, EMCD uniquely achieves spatial resolution down to 1nm or even less in an ultimate case of tailored beams<sup>8,9</sup>, and is capable of simultaneously obtaining local atomic structure, chemical component and magnetic moment information in a TEM<sup>10</sup>. With promising prospects, EMCD is still on its way to be a routine magnetic characterization technique. During the last ten years, EMCD experiments have been extensively performed on L<sub>2,3</sub> ( $2p_{1/2, 3/2} \rightarrow 3d_{3/2, 5/2}$ ) edges of 3d TM atoms or ions to improve EMCD experimental setups, data processing methods, and application of sum rules<sup>7,9,11,12,13,14</sup>. Other edges such as M<sub>4,5</sub> ( $3d_{3/2, 5/2} \rightarrow 4f_{5/2, 7/2}$ ) edges of 4f RE atoms or ions are rarely investigated. Moreover, the amplitude of EMCD signal is modulated by more factors than XMCD, e.g. the choice of reciprocal lattice vectors, specimen thickness, etc. due to dynamical effects<sup>7,14,15</sup>. EMCD signal carries richer information than XMCD and is more complex to interpret in real case. In this chapter, we apply EMCD technique to DyFe<sub>2</sub>/YFe<sub>2</sub> superlattices. A brief introduction of the sample preparation and the investigation of its crystallographic structure are at first presented. Then we probe both 4f moment by studying Dy-M<sub>4,5</sub> edges and 3d moment by Fe-L<sub>2,3</sub> edges in exactly the same area of DyFe<sub>2</sub>/YFe<sub>2</sub> superlattice, using EMCD technique. EMCD sum rules for M<sub>4,5</sub> edges are specially derived and applied to Dy-M<sub>4,5</sub> edges. In addition, the EMCD signal



and measured magnetic moments of Dy and Fe are compared to understand the coupling behavior, taking into account the dynamical effect.

## 1. Sample Preparation

The DyFe<sub>2</sub>/YFe<sub>2</sub> superlattices were grown using a molecular beam epitaxy (MBE) chamber<sup>16</sup> (cf. Appendix III). At first, a (1120)-orientated sapphire (Al<sub>2</sub>O<sub>3</sub>) substrate was covered at 700°C by a buffer layer of 50-nm (110) niobium, and then followed by a 2 nm iron seed layer at 600°C. A surface alloy with a two dimensional rectangular lattice was thus created, enabling the epitaxial growth of the DyFe<sub>2</sub>/YFe<sub>2</sub> superlattice. The superlattice was alternately grown by co-deposition of Fe and Dy or Y. The growth temperature was 500°C for the first YFe<sub>2</sub> layer and then reduced to 400°C for the following layers. Finally, a 100 nm Nb protection layer was deposited to prevent the superlattice from further oxidation by air. The whole growth process was monitored in-situ by RHEED diffraction. A cross-sectional TEM specimen was prepared (cf. Appendix II) for investigating the crystallographic structure and the local magnetic properties.

## 2. Structure and Composition Information

From the low-magnification bright-field image shown in Fig. 5.1, it can be seen that two different layers, exhibiting grey contrast appear alternatively to form a superlattice on the substrate and the buffer layer. The first two or three layers are curved, since the layers are initially grown from islands in the process of film deposition. There are also some very small areas where the interface is still curved after more than ten layers deposited. It may be due to local defects, which will not be studied here. However in most areas, the interfaces of those layers are rather flat and clean, indicating the good quality of the superlattice. The structure and composition information of the investigated specimen is described in the following.

### 2.1. Composition information

EELS technique in TEM mode was at first applied to the specimen for composition analysis. The spatial resolution was around 50 nm. EELS spectra were detected from the areas in the substrate, buffer layer, protection layer and superlattice layers respectively. The chemical compositions were determined. Fig. 5.2 displays the Fe-L<sub>2,3</sub>, Dy-M<sub>4,5</sub>, Y-L<sub>2,3</sub> detected from the superlattice layer (the area is marked as 1 in Fig. 5.1), and Nb-L<sub>2,3</sub> edges from the buffer layer (the area is marked as 2 in Fig. 5.1).

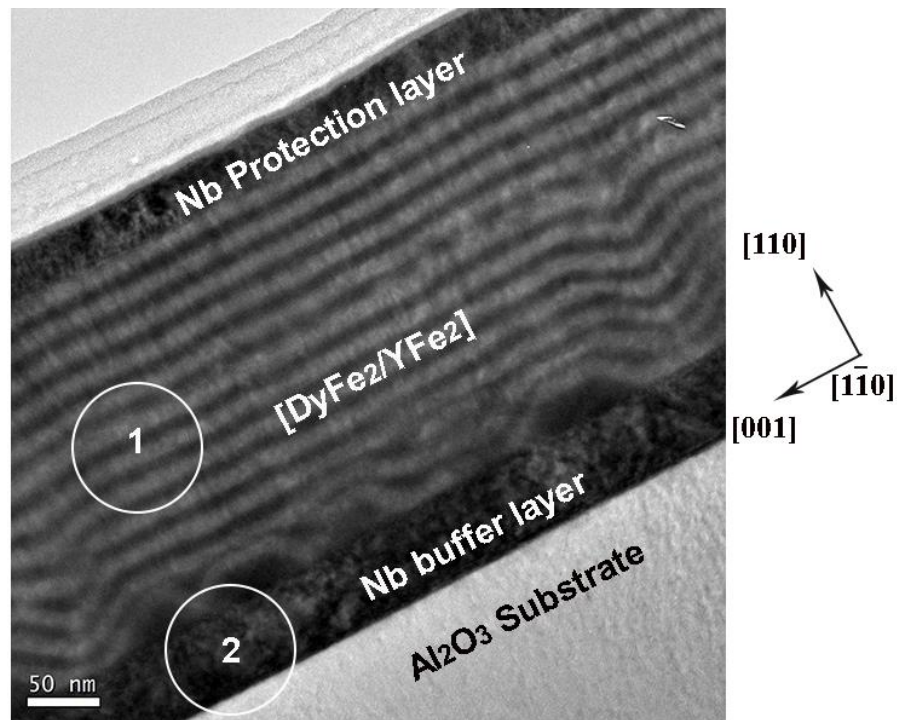


Fig. 5.1. Low-magnification bright-field image of epitaxial  $DyFe_2/YFe_2$  superlattice.

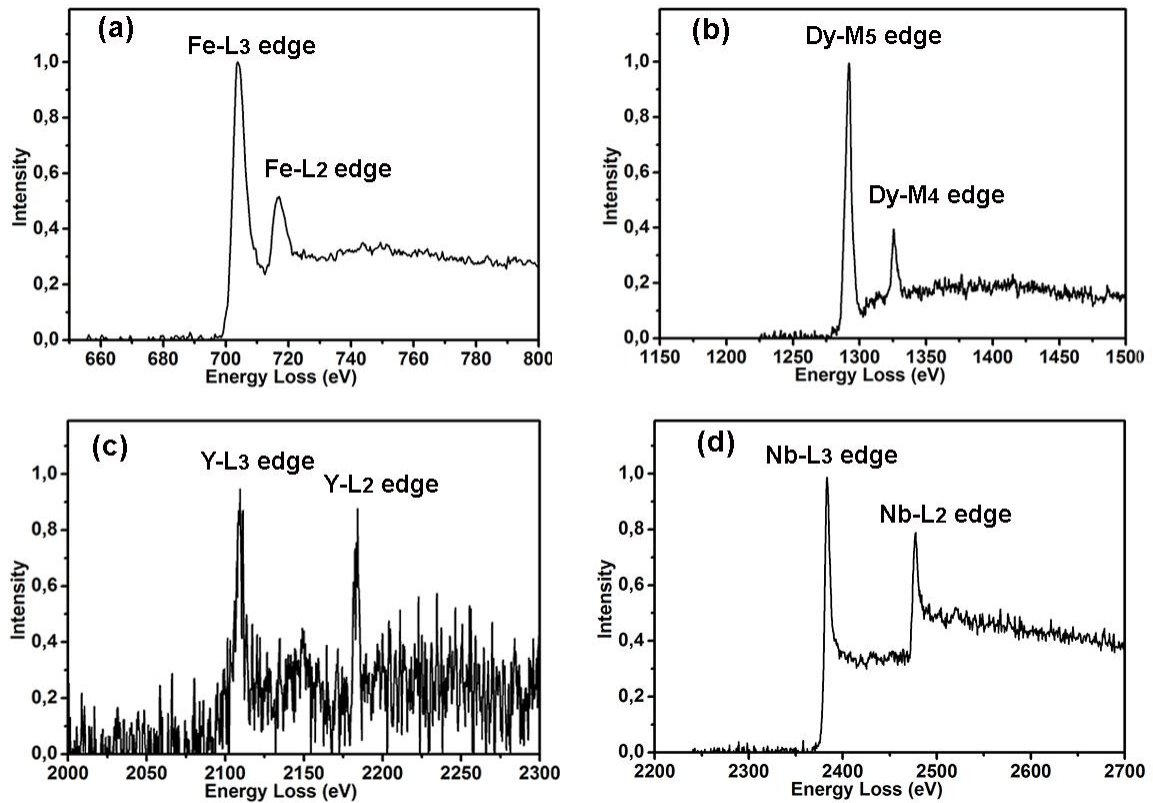


Fig. 5.2. EELS spectra of (a) Fe-L<sub>2,3</sub>, (b) Dy-M<sub>4,5</sub>, (c) Y-L<sub>2,3</sub> and (d) Nb-L<sub>2,3</sub> edges. Spectra in (a-c) were acquired in the area marked as No.1 in Fig. 5.1, and the spectrum in (d) was acquired in the area marked as n°2. The Y edges were obtained using a short acquisition time.

Moreover, EELS could be operated in STEM mode to achieve higher spatial resolution. Fig. 5.3(a) is a high angle annular dark field (HAADF) image, acquired using STEM-HAADF technique in the SACTEM of Toulouse. It has expected inverse brightness compared to the bright-field image. Scanning along the green line in Fig. 5.3(a), the corresponding image intensity as well as EELS spectra can be acquired. The image intensity along the line is shown in Fig. 5.3(b) and two typical EELS spectra shown in Fig. 5.3(c-d). It is found that the Dy-M<sub>4,5</sub> edges at the energy loss of around 1295 eV always appear when scanning each bright layer, but are not detectable when scanning each dark layer. Therefore, the bright layers in Fig. 5.3 (a) correspond to DyFe<sub>2</sub> and dark layers YFe<sub>2</sub>. Accordingly, we now recognize the bright and dark layers of Fig. 5.1. It is consistent with the published results presented in Fig. 3.3 in chapter III.

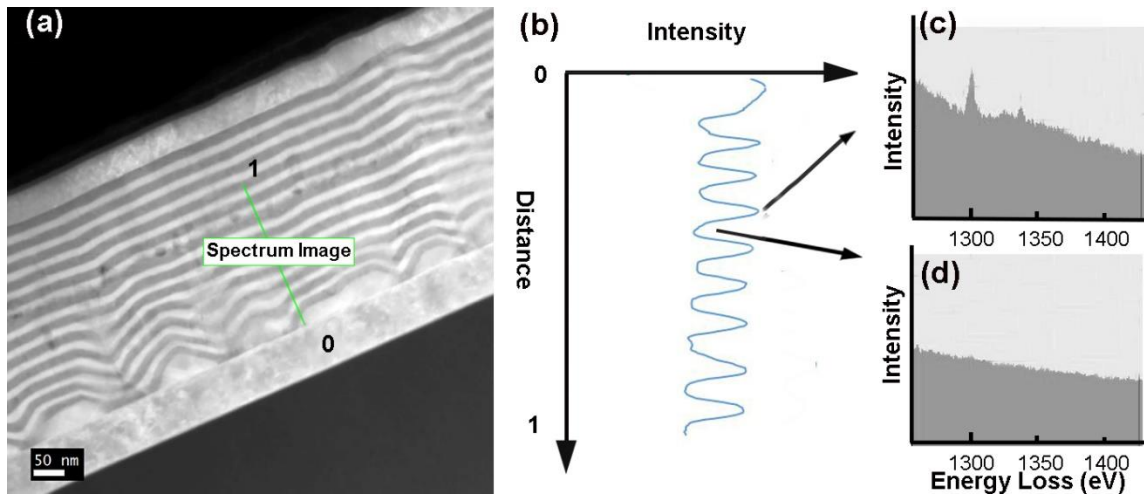


Fig. 5.3 (a) Low-magnification STEM-HAADF image of epitaxial DyFe<sub>2</sub>/YFe<sub>2</sub> superlattice; (b) intensity profile of the STEM-HAADF image along the green line in (a); higher intensity refers to brighter contrast in (a). Spectra in (c) and (d) are two typical EELS spectra obtained in the positions of bright and dark layers respectively. The Dy- $M_{4,5}$  edges at energy loss of around 1295 eV in (c) confirm the Dy component. No edges around 1300 eV is seen in (d).

## 2.2. Crystallographic structure information

It is mentioned in chapter III that DyFe<sub>2</sub> and YFe<sub>2</sub> crystals have very similar lattice constants at RT, making the DyFe<sub>2</sub>/YFe<sub>2</sub> superlattice a single crystal. High resolution TEM (HRTEM) and electron diffraction (ED) are two general techniques to study the crystallographic structure. A high resolution TEM (HRTEM) image acquired along the  $[1\bar{1}0]$  zone axis is presented in Fig. 5.4(b). It is across two DyFe<sub>2</sub> layers and three YFe<sub>2</sub> layers, and their interfaces are rather abrupt. The indexed fast fourier transform (FFT) of this HRTEM image illustrates the growth orientation which is DyFe<sub>2</sub>[110]//YFe<sub>2</sub>[110].

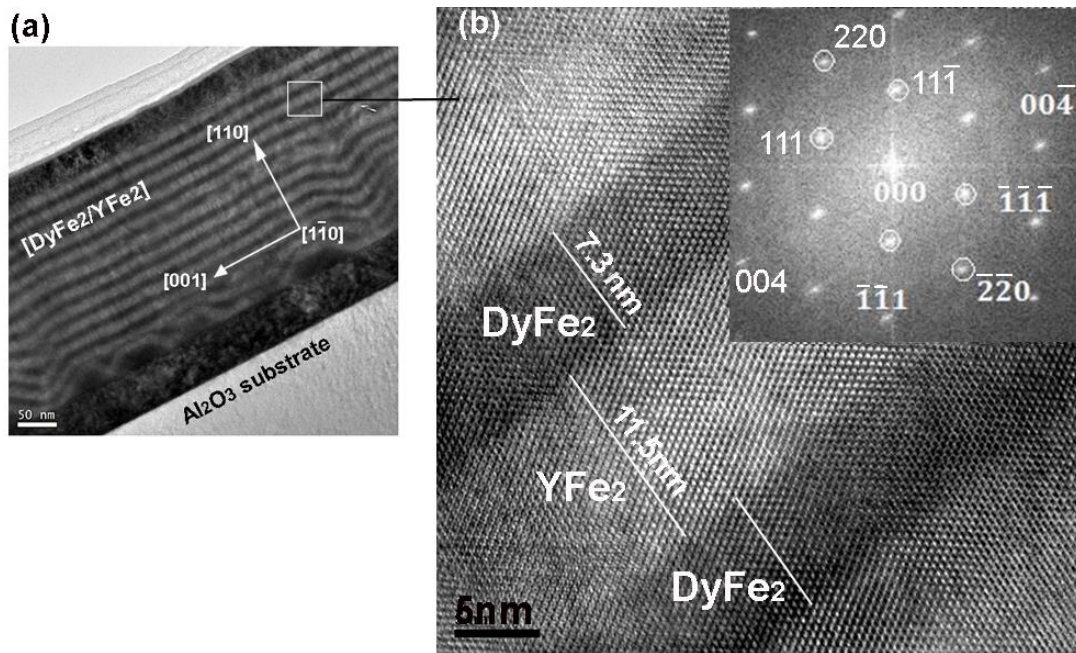


Fig. 5.4. (a) Low-magnification image of DyFe<sub>2</sub>/YFe<sub>2</sub> superlattice with indexation of crystal axes; (b) HRTEM image acquired along the zone axis of  $[1\bar{1}0]$ ; the inset in (b) is a fast fourier transform (FFT) of the HRTEM image.

In addition, a diffraction pattern was acquired using selected area electron diffraction (SAED) technique. The aperture size was 200nm, so that more than five DyFe<sub>2</sub> layers and five YFe<sub>2</sub> layers were selected. The diffraction pattern is shown in Fig. 5.5. It can be easily seen that the diffraction spots in green circles are much brighter than those in red circles. Provided that the DyFe<sub>2</sub> and YFe<sub>2</sub> have very similar lattice parameters and hence form a single crystal, their diffraction patterns must coincide, and each diffraction spot in Fig. 5.5 is the superposition of diffraction spots of DyFe<sub>2</sub> and YFe<sub>2</sub> crystals.

For the diffraction pattern, more information should be extracted. It is known that EMCD is a diffraction-based technique. The dynamical diffraction condition for high-energy electrons can modulate the weights of EMCD signals from different atoms, which is the key difference from XMCD. The choice of the diffraction spots used to achieve a three-beam condition needs therefore to be considered before real EMCD experiment. The selected diffraction spot must fulfill the following requirement: the corresponding diffracted beams must be diffracted from both Dy atomic planes and Fe atomic planes, if

both Dy and Fe dichroic signals need to be detected from the diffraction pattern. Calculations of the structure factor may provide useful information. The calculation is presented in detail as follow, taking DyFe<sub>2</sub> crystal as an example. The discussion on the dynamic diffraction effect will not be presented here but in the next section.

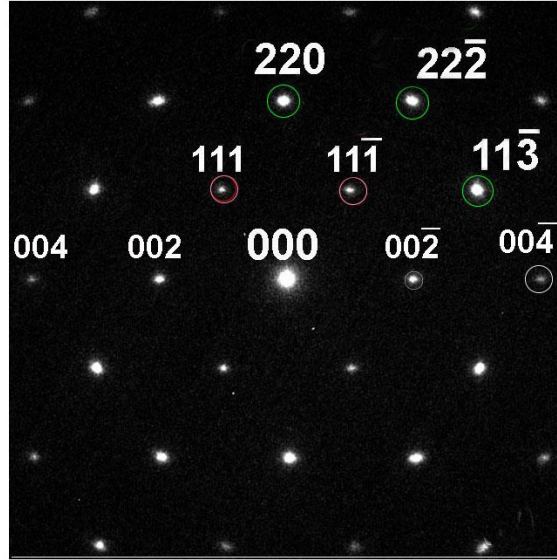


Fig. 5.5. The diffraction pattern acquired on the DyFe<sub>2</sub>/YFe<sub>2</sub> superlattice along the [1 $\bar{1}$ 0] zone axis.

The locations of Dy atoms are very similar to those of C atoms in diamond C<sub>12</sub>. For the diamond structure, there are 8 atoms in a unit cell. The atomic coordinates are: (000), ( $\frac{1}{2}, \frac{1}{2}, 0$ ), ( $\frac{1}{2}, 0, \frac{1}{2}$ ), ( $0, \frac{1}{2}, \frac{1}{2}$ ), ( $\frac{1}{4}, \frac{1}{4}, \frac{1}{4}$ ), ( $\frac{3}{4}, \frac{1}{4}, \frac{3}{4}$ ), ( $\frac{1}{4}, \frac{3}{4}, \frac{3}{4}$ ), ( $\frac{3}{4}, \frac{3}{4}, \frac{1}{4}$ ). Given the formula of structure factor  $F_{hkl} = \sum_i f_i e^{2\pi i(h+k+l)}$ , we have the structure factor of Dy atoms in Eq. 5.1.

$$\begin{aligned}
 F_{hkl(Dy)} &= \sum_i f_{i(Dy)} e^{2\pi i(h+k+l)} \\
 &= f_{hkl(Dy)} \left\{ e^{\pi i \times 0} + e^{\frac{\pi i}{2}(h+k+l)} + e^{\pi i(h+k+l)} + e^{\frac{\pi i}{2}(3h+k+3l)} + e^{\pi i(h+0+l)} \right. \\
 &\quad \left. + e^{\frac{\pi i}{2}(h+3k+3l)} + e^{\pi i(0+k+l)} + e^{\frac{\pi i}{2}(3h+3k+l)} \right\} \\
 &= f_{hkl(Dy)} \left[ 1 + e^{\frac{\pi i}{2}(h+k+l)} \right] \left[ 1 + e^{\pi i(h+k)} + e^{\pi i(h+l)} + e^{\pi i(k+l)} \right] \quad (5.1)
 \end{aligned}$$

16 Fe atoms are located in the unit cell of diamond structure of Dy atoms. The atomic coordinates are:  $(\frac{3}{8}, \frac{1}{8}, \frac{7}{8})$ ,  $(\frac{1}{8}, \frac{3}{8}, \frac{7}{8})$ ,  $(\frac{7}{8}, \frac{5}{8}, \frac{7}{8})$ ,  $(\frac{5}{8}, \frac{7}{8}, \frac{7}{8})$ ,  $(\frac{1}{8}, \frac{1}{8}, \frac{5}{8})$ ,  $(\frac{3}{8}, \frac{3}{8}, \frac{5}{8})$ ,  $(\frac{5}{8}, \frac{5}{8}, \frac{5}{8})$ ,  $(\frac{7}{8}, \frac{7}{8}, \frac{5}{8})$ ,  $(\frac{7}{8}, \frac{1}{8}, \frac{3}{8})$ ,  $(\frac{5}{8}, \frac{3}{8}, \frac{3}{8})$ ,  $(\frac{3}{8}, \frac{5}{8}, \frac{3}{8})$ ,  $(\frac{1}{8}, \frac{7}{8}, \frac{3}{8})$ ,  $(\frac{5}{8}, \frac{1}{8}, \frac{1}{8})$ ,  $(\frac{7}{8}, \frac{3}{8}, \frac{1}{8})$ ,  $(\frac{1}{8}, \frac{5}{8}, \frac{1}{8})$ ,  $(\frac{3}{8}, \frac{7}{8}, \frac{1}{8})$ . We have the structure factor of Fe atoms in Eq. 5.2.

$$F_{hkl(Fe)} = \sum_i f_{i(Fe)} e^{2\pi i(h+k+l)} \\ = f_{hkl(Fe)} e^{\frac{\pi i}{4}(h+k+l)} \left[ e^{\pi i(h+k+l)} + e^{\pi i h} + e^{\pi i k} + e^{\pi i l} \right] \left[ 1 + e^{\frac{\pi i}{2}(h+k)} + e^{\frac{\pi i}{2}(h+l)} + e^{\frac{\pi i}{2}(k+l)} \right] \quad (5.2)$$

The structure factors of Dy and Fe atoms for specific diffraction spots can then be calculated according to Eq. 5.1 and 5.2.  $f_{(Fe)}$  and  $f_{(Dy)}$  are the atomic scattering factor of Fe and Dy, respectively. Some calculated results are listed in Table 1. From the table 5.1, we know that the spot (002) must be absent, because the F factor of both Dy and Fe are 0. For spot (2 $\bar{2}$ 0), the Fe atomic plane has no contribution. For spot (2 $\bar{2}$ 2), the Dy atomic plane has no contribution. For spots (11 $\bar{3}$ ) and (1 $\bar{1}$ 1), the F factors have non-zero values for Dy and Fe, thus those spots can be selected for EMCD experiment, in order to detect both Dy and Fe dichroic signals in the same two- or three-beam condition.

Table 5.1. Structure factors of Dy and Fe in DyFe<sub>2</sub> lattice for specific diffraction spots

$F_{hkl}$	(002)	(2 $\bar{2}$ 0)	(2 $\bar{2}$ 2)	(11 $\bar{3}$ )	(1 $\bar{1}$ 1)
<b>Dy</b>	0	$8f_{2\bar{2}0(Dy)}$	0	$4(1-i)f_{1\bar{1}3(Dy)}$	$4(1+i)f_{1\bar{1}1(Dy)}$
<b>Fe</b>	0	0	$16if_{2\bar{2}2(Fe)}$	$4\sqrt{2}(1-i)f_{1\bar{1}3(Fe)}$	$-4\sqrt{2}(1+i)f_{1\bar{1}1(Fe)}$

Fig. 5.6 is a simulated diffraction pattern along the zone axis of [1 $\bar{1}$ 0] of DyFe<sub>2</sub>. The spot (002) in the simulated pattern is absent as expected in table 5.1, but appear in the experimental diffraction pattern in Fig. 5.5. It is due to the multiple diffraction in the real experiment. Moreover, in Fig. 5.6, the spots of the <111> family are several times weaker than <113> ones, so <113> family spots are preferable for EMCD experiment. The  $\pm(11\bar{3})$  diffraction spot are actually excited to achieve the three beam condition in our EMCD experiment.

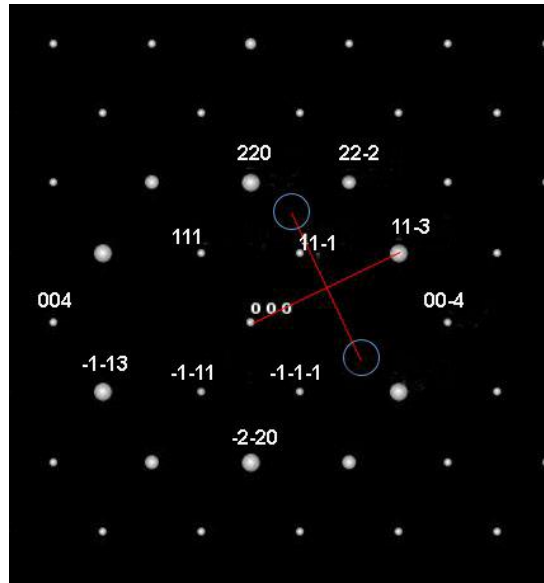


Fig. 5.6. A simulated diffraction pattern along the  $[1\bar{1}0]$  zone axis of DyFe<sub>2</sub> crystal.

### 3. EMCD Study of Epitaxial DyFe<sub>2</sub>/YFe<sub>2</sub> superlattices

In this section, the EMCD study of Fe and Dy elements in the DyFe<sub>2</sub>/YFe<sub>2</sub> superlattice is presented. Two issues are addressed in particular. First, EMCD sum rules which are especially aimed at M<sub>4,5</sub> edges are derived and applied to Dy-M<sub>4,5</sub> edges. Second, the influence of dynamic diffraction effect on the detected dichroic signal is discussed in detail. It supports the statement that opposite signs of Fe-L<sub>3</sub> peak and Dy-M<sub>5</sub> peak indicate the antiparallel coupling of Fe and Dy moments.

#### 3.1 Acquisition of EMCD signals on L<sub>2,3</sub> and M<sub>4,5</sub> edges

EMCD signals of Fe-L<sub>2,3</sub> and Dy-M<sub>4,5</sub> edges were acquired in the same three-beam condition, where only  $(1\bar{1}3)$  diffraction spots were excited. The method we used to acquire EMCD signal is illustrated in Fig. 5.7. The crystal was orientated in the TEM to achieve a  $(1\bar{1}3)$  three-beam condition. The magnetic field as large as 2 T was applied on the crystal along the electron beam axis. LACDIF setup was performed to obtain a diffraction pattern with three spots in image plane. ESI technique was applied to record



two data cubes<sup>11</sup> successively. The two data cubes essentially contained a series of energy-filtered diffraction patterns with energy windows of typically 1 eV running over investigated edges. One was recorded in the energy range from 690 to 735 eV, which covered Fe-L<sub>2,3</sub> edges. The exposure time was 10s/eV. The other one was from 1275 to 1345 eV, which covered Dy-M<sub>4,5</sub> edges. The exposure time was 30s/eV. Longer exposure time was set for Dy-M<sub>4,5</sub> edges because the Dy-M<sub>4,5</sub> edges has much lower intensity than the Fe-L<sub>2,3</sub> edges. Post-corrections, including corrections of non-isochromaticity and spatial drift, on data cubes were made in Digital Micrograph software. Two virtual entrance apertures were then accurately positioned in position 1 and 2 on each post-corrected data cube, and two EELS spectra were reconstructed. The spectra difference between the two is the dichroic signal, from which the magnetic moment information can be extracted. It is worth stressing that the aperture positions were exactly the same for the two data cubes, as seen in Fig. 5.8.

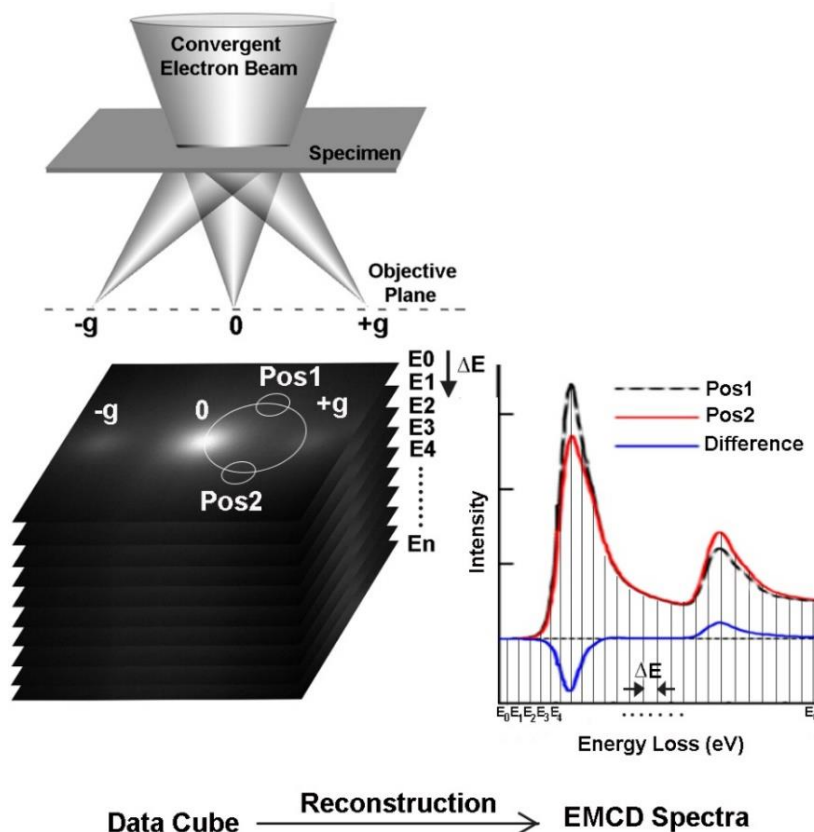


Fig. 5.7. Schematic diagram of EMCD experimental configuration using ESI technique. The acquisition of a data cube and the reconstruction of an EELS spectrum are displayed.

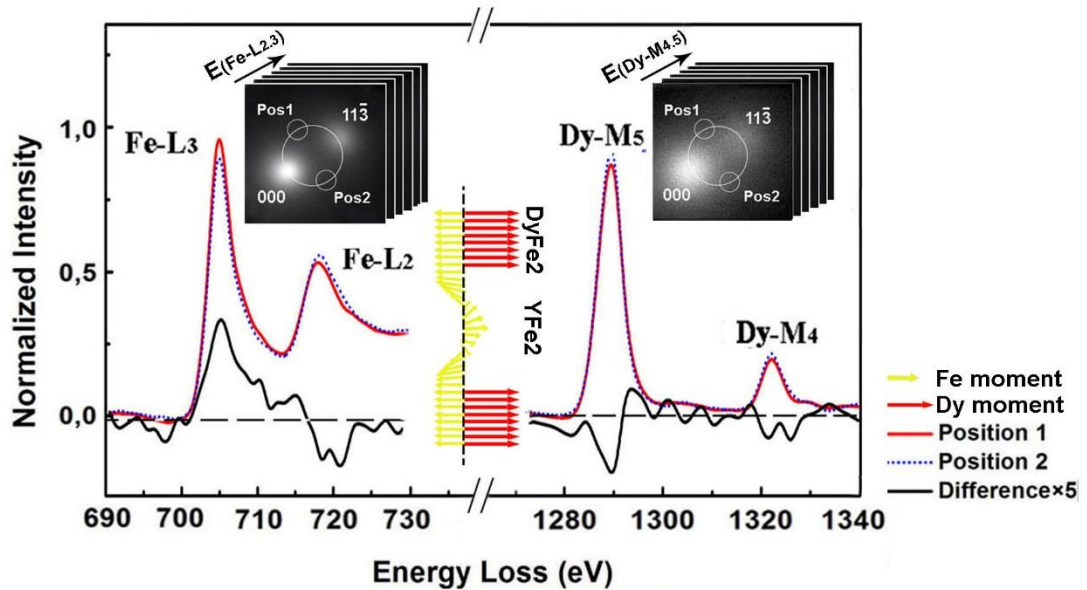


Fig. 5.8. EELS and EMCD signals of Fe-L<sub>2,3</sub> edges and Dy-M<sub>4,5</sub> edges. In the insert are post-corrected data cubes containing a series of energy filtered diffraction patterns in the three-beam condition over Fe-L<sub>2,3</sub> and Dy-M<sub>4,5</sub> edges respectively. Only a transmission spot and a diffraction spot are shown. The sketch in the middle represents the possible magnetic configuration of Dy and Fe moments in the DyFe<sub>2</sub>/YFe<sub>2</sub> stack in our experiment condition.

Fig. 5.8 are EELS and EMCD spectra of Fe-L<sub>2,3</sub> and Dy-M<sub>4,5</sub> edges respectively. Both the EMCD spectra of Fe-L<sub>2,3</sub> and Dy-M<sub>4,5</sub> edges are obtained by subtracting the EELS spectra recorded in position 1 from the ones in position 2. It is found that the Fe dichroic signal has a negative sign at the L<sub>3</sub> peak and a positive sign at the L<sub>2</sub> peak. On the contrary, the Dy dichroic signal has a positive sign at the M<sub>5</sub> peak and, different from the case in transition metal, has the same sign at the M<sub>4</sub> peak. What does the sign of peaks indicate will be discussed in section 3.3 and 3.4. The quantitative analysis of the dichroic signal is presented in the next section.

### 3.2 EMCD Sum rules for M<sub>4,5</sub> edges

Quantitative information can be extracted by applying sum rules to the EMCD spectra. The EMCD sum rules specified for L<sub>2,3</sub> edges of 3d transition metal have already been derived by Calmels. *et al.* and shown in Eq. (1.12-1.14) in chapter I. They are presented here again in Eq. (5.1-5.3).

$$\frac{\int_{L_3} (\sigma_2 - \sigma_1) dE - 2 \int_{L_2} (\sigma_2 - \sigma_1) dE}{\int_{L_2+L_3} (\sigma_2 + \sigma_1) dE} = K \left( \frac{2\langle S_z \rangle}{3N_h} + \frac{7\langle T_z \rangle}{3N_h} \right) \quad (5.1)$$

$$\frac{\int_{L_2+L_3} (\sigma_2 - \sigma_1) dE}{\int_{L_2+L_3} (\sigma_2 + \sigma_1) dE} = K \frac{\langle L_z \rangle}{2N_h} \quad (5.2)$$

$$\frac{\int_{L_3} (\sigma_2 - \sigma_1) dE - 2 \int_{L_2} (\sigma_2 - \sigma_1) dE}{\int_{L_2+L_3} (\sigma_2 - \sigma_1) dE} = \frac{4\langle S_z \rangle + 14\langle T_z \rangle}{3\langle L_z \rangle} \quad (5.3)$$

However, these sum rules cannot be directly applied to other edges, since different edges originate from different electron transition processes, and those coefficients in Eq. (5.1-5.3) are actually not constant. Specific EMCD sum rules for M<sub>4,5</sub> edges of 4f rare earth have to be derived to interpret our Dy dichroic signal. As the EMCD sum rules are originally derived from the XMCD sum rules, it is necessary to discuss the XMCD sum rules for various edges at first. The derivation process is also necessary to explain in detail here, in order to clearly demonstrate the following derivation of EMCD sum rules for M<sub>4,5</sub> edges and the discussion of dynamic diffraction effect in section 3.3 and 3.4.

### 3.2.1 General XMCD sum rules

Paolo Carra *et al.*<sup>17</sup> in 1993 derived two general sum rules yielding the ground-state expectation value of the orbital angular momentum per hole  $\langle L_z \rangle$  and the spin angular momentum  $\langle S_z \rangle$  per hole, as shown in Eq. (5.4-5.5).

$$\frac{\int_{j_++j_-} dw(u^+ - u^-)}{\int_{j_++j_-} dw(u^+ + u + u^0)} = \frac{1}{2} \frac{l(l+1) + 2 - c(c+1)}{l(l+1)(4l+2-n)} \langle L_z \rangle \quad (5.4)$$

$$\frac{\int_{j_+} dw(u^+ - u^-) - [(c+1)/c] \int_{j_-} dw(u^+ - u^-)}{\int_{j_+ + j_-} dw(u^+ + u^- + u^0)} = \frac{l(l+1) - 2 - c(c+1)}{3c(4l+2-n)} \langle S_z \rangle$$

$$+ \frac{l(l+1)[l(l+1) + 2c(c+1) + 4] - 3(c-1)^2(c+2)^2}{6lc(l+1)(4l+2-n)} \langle T_z \rangle$$
(5.5)

where  $c$  and  $l$  denote the orbital quantum number of the core and the valence shell involved in the  $c \rightarrow l$  dipole electron transition. For instance, L<sub>2,3</sub> absorption edges of 3d transition metal correspond to the transition from the 2p core shell to the 3d valence shell, thus  $c=1, l=2$ . For the 4f rare earth, L<sub>2,3</sub> edges are due to the transition from 2p core shell to 5d shell, but similarly giving  $c=1, l=2$ . M<sub>4,5</sub> edges of 4f rare earth correspond to the transition from the 3d core shell to the 4f valence shell, giving different values  $c=2, l=3$ .  $n$  denotes the number of electrons in the valence shell, and  $4l+2-n$  is the number of electron holes (named N<sub>h</sub>).  $j_{\pm} = c \pm 1/2$  denote two absorption processes from two different sub-states in the core shell  $c$ .  $\int_{j_{\pm}} dw(u^+ - u^-)$  is the integral over an edge, corresponding to the transition from  $c+1/2$  substate, in an XAS spectrum.  $u^+$  and  $u^-$  are XAS spectra obtained with right-polarized and left-polarized X ray respectively, and  $u^0$  is the spectrum obtained with non-polarized beam. Moreover,  $u^+, u^-$  and  $u^0$  denote the XAS spectra for incident photons with right circular polarizations, left circular polarizations and linearly polarizations parallel to the vector direction respectively. As an often used approximation, we have  $u^+ + u^- + u^0 = 3/2(u^+ + u^-)$ .

### 3.2.2. Derivation of general EMCD sum rules from XMCD ones

For XAS, the absorption intensity at a specific edge is proportional to the transition probability, whereas the EELS spectrum intensity described as DDSCS is influenced by more factors such as the dynamic electron diffraction effect. Fortunately, the contribution of the dynamic effect and the electron transition can be separated<sup>18</sup>, so that it is possible to build the connection between the EELS spectrum intensity and magnetic momentums in the way presented in Eq. (5.4-5.5). What follows is how the connection is built.

According to the chapter 8 in ref [22], the DDSCS can be written as

$$\frac{\partial^2 \sigma}{\partial \Omega \partial E} = \sum_{\mathbf{q}} \frac{A_{\mathbf{q}, \mathbf{q}}}{q^4} S(\mathbf{q}, \mathbf{q}, E) + \sum_{\mathbf{q}} \sum_{\mathbf{q}' \neq \mathbf{q}} 2 \text{Re} \left[ \frac{A_{\mathbf{q}, \mathbf{q}'}}{q^2 q'^2} S(\mathbf{q}, \mathbf{q}', E) \right]$$
(5.6)

where  $S(\mathbf{q}, \mathbf{q}', E)$  is the MDFFF factor; the vector  $\mathbf{q} = (q_x \mathbf{e}_x + q_y \mathbf{e}_y + q_z \mathbf{e}_z)$  is the momentum-transferred vector; the xy plane is parallel to the diffraction plane; the coefficients  $A_{\mathbf{q}, \mathbf{q}'}$  are products of Bloch wave coefficients of the incident and scattered electrons.

We have  $S(\mathbf{q}, \mathbf{q}', E)$  expressed in Eq. (5.7), in terms of the functions  $\mu_+(E)$ ,  $\mu_-(E)$  and  $\mu_0(E)$ :

$$S(\mathbf{q}, \mathbf{q}', E) = \frac{q_x q'_x + q_y q'_y}{2} [\mu_+(E) + \mu_-(E)] + q_z^2 \mu_0(E) + i \frac{q_x q'_y - q_y q'_x}{2} [\mu_+(E) - \mu_-(E)] \quad (5.7)$$

where

$$\mu_+(E) = \sum_f \left| \left\langle f \left| \frac{x+iy}{\sqrt{2}} \right| i \right\rangle \right|^2 \delta(E_f - E_i - E) \quad (5.8)$$

$$\mu_-(E) = \sum_f \left| \left\langle f \left| \frac{x-iy}{\sqrt{2}} \right| i \right\rangle \right|^2 \delta(E_f - E_i - E) \quad (5.9)$$

and

$$\mu_0(E) = \sum_f \left| \langle f | z | i \rangle \right|^2 \delta(E_f - E_i - E) \quad (5.10)$$

It has to be mentioned that  $\mu_+(E)$ ,  $\mu_-(E)$  and  $\mu_0(E)$  have the same meaning as the  $r_+$ ,  $r_-$  and  $r_0$  in Eq. (1.10) in chapter I. Don't confuse the  $r_+$ ,  $r_-$  and  $r_0$  in Eq. (1.10) with the ones in Ref. [7]. Using an additional approximation  $\mu_0(E) \approx \frac{1}{2}[\mu_+(E) + \mu_-(E)]$ , which is similar to the approximation  $u^0 = \frac{1}{2}(u^+ + u^-)$  for XMCD, the expression of  $S(\mathbf{q}, \mathbf{q}', E)$  is given in Eq. (5.11):

$$S(\mathbf{q}, \mathbf{q}', E) = \frac{2}{3} \cdot \frac{q_x q'_x + q_y q'_y + q_z^2}{2} [\mu_+(E) + \mu_-(E) + \mu_0(E)] + i \frac{q_x q'_y - q_y q'_x}{2} [\mu_+(E) - \mu_-(E)] \quad (5.11)$$

Insert Eq. (5.11) into Eq. (5.6), then we obtain the DDSCS in terms of the functions  $\mu_+(E)$ ,  $\mu_-(E)$  and  $\mu_0(E)$ , as shown in Eq. (5.12).

$$\begin{aligned} \frac{\partial^2 \sigma}{\partial \Omega \partial E} &= \frac{2}{3} [\mu_+(E) + \mu_-(E) + \mu_0(E)] \\ &\left[ \sum_{\mathbf{q}} \frac{q_x^2 + q_y^2 + q_z^2}{2q^4} A_{\mathbf{q},\mathbf{q}} + \sum_{\mathbf{q}} \sum_{\mathbf{q}' \neq \mathbf{q}} \frac{q_x q_x' + q_y q_y' + q_z^2}{q^2 q'^2} \text{Re}(A_{\mathbf{q},\mathbf{q}'} ) \right] \\ &- [\mu_+(E) - \mu_-(E)] \sum_{\mathbf{q}} \sum_{\mathbf{q}' \neq \mathbf{q}} \frac{q_x q_y' - q_y q_x'}{q^2 q'^2} \text{Im}(A_{\mathbf{q},\mathbf{q}'} ) \end{aligned} \quad (5.12)$$

As described in chapter I, EMCD corresponds to the difference between two EELS spectra, which are detected from two symmetric positions labelled as position 1 and position 2. On the two positions,  $(q_x q_y' - q_y q_x')$  are equivalent but opposite in sign, and  $q_x q_x' + q_y q_y'$  and  $A_{\mathbf{q},\mathbf{q}'}$  are equivalent in both absolute value and sign. These preconditions will be verified in section 3.3. As a consequence, the difference and the sum of two EELS spectra can be expressed as Eq. (5.13) and (5.14).

$$\left. \frac{\partial^2 \sigma}{\partial \Omega \partial E} \right|_{\text{position2}} - \left. \frac{\partial^2 \sigma}{\partial \Omega \partial E} \right|_{\text{position1}} = 2[\mu_+(E) - \mu_-(E)] \sum_{\mathbf{q}} \sum_{\mathbf{q}' \neq \mathbf{q}} \frac{q_x q_y' - q_y q_x'}{q^2 q'^2} \text{Im}(A_{\mathbf{q},\mathbf{q}'} ) \quad (5.13)$$

$$\begin{aligned} \left. \frac{\partial^2 \sigma}{\partial \Omega \partial E} \right|_{\text{position2}} + \left. \frac{\partial^2 \sigma}{\partial \Omega \partial E} \right|_{\text{position1}} &= \frac{2}{3} [\mu_+(E) + \mu_-(E) + \mu_0(E)] \\ &\left[ \sum_{\mathbf{q}} \frac{1}{q^2} A_{\mathbf{q},\mathbf{q}} + 2 \sum_{\mathbf{q}} \sum_{\mathbf{q}' \neq \mathbf{q}} \frac{q_x q_x' + q_y q_y' + q_z^2}{q^2 q'^2} \text{Re}(A_{\mathbf{q},\mathbf{q}'} ) \right] \end{aligned} \quad (5.14)$$

Now we can see that the difference and the sum of two EELS spectra are related to  $[\mu_+(E) - \mu_-(E)]$  and  $[\mu_+(E) + \mu_-(E) + \mu_0(E)]$  respectively. Their coefficients contain all the information related to the dynamic electron diffraction effect. In this section, we focus on the derivation of sum rules, so it is better to make the Eq. (5.13-5.14) simpler, by replacing the coefficients and DDSCS with letters as shown in Eq. (5.15-5.16).

$$\sigma_2 - \sigma_1 = a[\mu_+(E) - \mu_-(E)] \quad (5.15)$$

$$\sigma_2 + \sigma_1 = b[\mu_+(E) + \mu_-(E) + \mu_0(E)] \quad (5.16)$$

Provided the relationship among  $u_+ + u_- + u_0$ ,  $u_+ - u_-$  and magnetic momentums in the XMCD sum rules, general EMCD sum rules can be finally given as Eq. (5.17-5.18), thanks to Eq. (5.4-5.5).

$$\frac{\int_{j_+j_-} (\sigma_2 - \sigma_1)}{\int_{j_+j_-} (\sigma_2 + \sigma_1)} = \frac{a}{b} \cdot \frac{1}{2} \frac{l(l+1) + 2 - c(c+1)}{l(l+1)(4l+2-n)} \langle L_z \rangle \quad (5.17)$$

$$\frac{\int_{j_+} (\sigma_2 - \sigma_1) - [(c+1)/c] \int_{j_-} (\sigma_2 - \sigma_1)}{\int_{j_+j_-} (\sigma_2 + \sigma_1)} = \frac{a}{b} \cdot \left[ \frac{l(l+1) - 2 - c(c+1)}{3c(4l+2-n)} \langle S_z \rangle \right. \\ \left. + \frac{l(l+1)[l(l+1) + 2c(c+1) + 4] - 3(c-1)^2(c+2)^2}{6lc(l+1)(4l+2-n)} \langle T_z \rangle \right] \quad (5.18)$$

### 3.2.3. Sum rules for M<sub>4,5</sub> edges of 4f rare earth and its application

We now write the three EMCD sum rules for M<sub>4,5</sub> edges in Eq. (5.19-5.21), provided that  $c=2$  and  $l=3$ .  $N_h=4l+2-n$  is the number of 4f holes.

$$\frac{2 \int_{M_5} (\sigma_2 - \sigma_1) dE - 3 \int_{M_4} (\sigma_2 - \sigma_1) dE}{\int_{M_5+M_4} (\sigma_2 + \sigma_1) dE} = \frac{a}{b} \left( \frac{4}{3} \frac{\langle S_z \rangle}{N_h} + 4 \frac{\langle T_z \rangle}{N_h} \right) \quad (5.19)$$

$$\frac{\int_{M_5+M_4} (\sigma_2 - \sigma_1) dE}{\int_{M_5+M_4} (\sigma_2 + \sigma_1) dE} = \frac{a}{b} \cdot \frac{1}{3} \frac{\langle L_z \rangle}{N_h} \quad (5.20)$$

$$\frac{2 \int_{M_5} (\sigma_2 - \sigma_1) dE - 3 \int_{M_4} (\sigma_2 - \sigma_1) dE}{\int_{M_5+M_4} (\sigma_2 - \sigma_1) dE} = \frac{4 \langle S_z \rangle + 12 \langle T_z \rangle}{\langle L_z \rangle} \quad (5.21)$$

For Dy ion in DyFe<sub>2</sub>,  $N_h=5$ . Before applying the sum rules to Dy<sup>3+</sup> ion, several points must be made clear. First, to perfectly meet the validity condition of these sum rules, the M<sub>5</sub> and M<sub>4</sub> edges have to correspond to pure 3d<sub>5/2</sub> and 3d<sub>3/2</sub> states respectively<sup>19</sup>, but in real situation the mixing between the two states may exist due to 3d-4f interaction. That means correction must be made to obtain more accurate values if there is overlapping region in M<sub>5</sub> and M<sub>4</sub> edges. Fortunately this derivation from sum rule has been proved to be negligible for heavy 4f moments like Dy, which has sufficient energy gap between M<sub>5</sub> and M<sub>4</sub> edges thanks to the strong spin-orbit coupling<sup>19</sup>.

Second, another assumption of importance has been made to simplify the derivation of EMCD sum rules<sup>7,18</sup>. To obtain the orbital and spin moments of an element, all the magnetic moments in the observed area must be aligned along the z axis, which is the optical axis of TEM; if not, the measured value is just the projection of a magnetic moment along the z direction. In our experiment, the sample is orientated along the [1 $\bar{1}$ 0] zone axis and the TEM objective lens exerts a magnetic field as large as 2 T along the z

direction on the specimen. How the magnetic moments will rotate with the applied field? In chapter III, three different magnetization reversal processes are introduced. Our sample [7.3nmDyFe<sub>2</sub>/11.5nmYFe<sub>2</sub>] must follow the “soft first” (SF) process as it is a DyFe<sub>2</sub>-magnetization-dominating sample. In theory, Fe moments in both DyFe<sub>2</sub> and YFe<sub>2</sub> layers are parallel but have an antiparallel coupling with Dy moments if no magnetic field is exerted on it. When a magnetic field is applied, a part of Fe moments in YFe<sub>2</sub> layers rotate towards the applied field, thus an exchange spring is formed. If the applied field is high enough, the Fe moments in YFe<sub>2</sub> layers will have an antiparallel alignment with the Fe moments in DyFe<sub>2</sub> layers and parallel with Dy moments. Few experimental results of [7.3nmDyFe<sub>2</sub>/11.5nmYFe<sub>2</sub>] can be seen in literature, but a sample [10nmDyFe<sub>2</sub>/13nmYFe<sub>2</sub>] with similar ratio of DyFe<sub>2</sub> and YFe<sub>2</sub> layers has been studied in Ref. [16] by SQUID. It is believed that our sample is not saturated under the magnetic field of 2 T, but in a form of exchange spring (cf. Fig. 3.1 and Fig. 3.5 in chapter III). Therefore, we have to emphasize that Fe and Dy moments measured from the EMCD spectra in Fig. 5.8 are net moments projected on the optical axis. It will be interesting to study the element-specific reversal magnetization in exchange spring systems using EMCD technique, in the future experiments. But in this chapter, we only focus on the magnetization at 2 T.

Third, different from the negligible  $\langle T_z \rangle$  of Mn ions, the strong orbit-spin coupling in 4f electrons makes  $\langle T_z \rangle$  in Eq. (5.19) and (5.21) non-negligible. The spin-to-orbital moment ratio can therefore hardly be obtained by applying Eq. (5.21) to the dichroic spectrum. Actually  $\langle T_z \rangle$  can be calculated using Eqs. 8 and 9 in Ref [17], since RE-M<sub>4,5</sub> edges are characterized by a pure LSJ coupling Hund's-rule ground state with well-localized 4f electrons. Even so, we estimate the ratio of orbital moment  $\langle L_z \rangle$  to effective spin moment  $\langle S_{eff} \rangle = \langle S_z + 3\langle T_z \rangle \rangle$  instead of the ratio of orbital and spin moment.

Now we apply the sum rule in Eq. (5.21) without doubt to the dichroic spectra of Fe and Dy. As shown in Table 5.2, the  $\langle L_z \rangle / \langle S_z \rangle$  value of Fe element is measured to be  $0.20 \pm 0.05$  and  $\langle L_z \rangle / \langle S_{eff} \rangle$  of Dy element is measured to be  $5.13 \pm 0.8$ . The statistical error mainly originates from relatively low signal-to-noise ratio. In addition, the exactly same three-beam condition is hard to obtain all the time, and small tilt from that condition can influence the result. A theoretical  $\langle L_z \rangle / \langle S_{eff} \rangle$  value of Dy<sup>3+</sup> was given to be 1.82<sup>19</sup>. Recently a  $\langle L_z \rangle / \langle S_z \rangle$  value of Dy<sup>3+</sup> in DyCo<sub>3</sub> was reported to be 2.57 measured by XMCD



technique. Our  $\langle L_z \rangle / \langle S_{eff} \rangle$  value is larger than theoretical values due to that the theoretical calculation is based on the atomic ground state at T=0K. But at RT, other states can mix into the ground state in the same order. The  $\langle L_z \rangle / \langle S_z \rangle$  value of Fe cannot be directly compared to any theoretical value or XMCD one, as our value for Fe is obtained from the Fe moments far away from being aligned. To my knowledge, it is the first time that quantitative EMCD experiment has been applied to the RE element. This opens a promising field of study.

Table 5.2. EMCD results of the orbital-to-spin momentum ratios of Fe and Dy elements in DyFe<sub>2</sub>/YFe<sub>2</sub> superlattice.

	Fe in DyFe <sub>2</sub> /YFe <sub>2</sub>	Dy in DyFe <sub>2</sub> /YFe <sub>2</sub>
EMCD results of $\langle L_z \rangle / \langle S_{eff} \rangle$	0.20±0.05	5.13±0.8

### 3.3 Coupling Behavior of Fe and Dy moments

Previously in section 3.1, there arised a question: what do the opposite signs of dichroic signals at the Fe-L<sub>3</sub> peak and Dy-M<sub>5</sub> peak mean. If in the case of XMCD, it generally indicates that the two magnetic moments have an antiparallel coupling<sup>3,4,5,20</sup>. However, in spite of the similar principle of EMCD and XMCD, further discussion is necessary before unambiguously interpreting the opposite signs in the case of EMCD.

For the sake of clarity, we have to understand if the dynamical diffraction effect has the possibility to introduce different interpretation. In the previous section, contributions of the dynamic effect and electron transition to the EELS and EMCD spectra are separated, and a factor of  $a/b$  appearing in both orbital and spin sum rules contains all the information related to dynamic effect. If we confirm a same sign in the  $a/b$  factor for the detected Fe and Dy spectra in our experiment, we can unambiguously determine the antiparallel coupling between Fe-3d moments and Dy-4f moments. The coefficient  $a/b$  is written as follow<sup>22</sup>:

$$\frac{a}{b} = \frac{3 \sum_{\mathbf{q}} \sum_{\mathbf{q}' \neq \mathbf{q}} \frac{q_x q'_y - q_y q'_x}{q^2 q'^2} \text{Im}(A_{\mathbf{q}, \mathbf{q}'})}{\sum_{\mathbf{q}} \frac{1}{q^2} A_{\mathbf{q}, \mathbf{q}} + 2 \sum_{\mathbf{q}} \sum_{\mathbf{q}' \neq \mathbf{q}} \frac{q_x q'_x + q_y q'_y + q_z^2}{q^2 q'^2} \text{Re}(A_{\mathbf{q}, \mathbf{q}'})} \quad (5.22)$$

One should note that some assumptions are made when deriving the  $a/b$  factor in section 3.2. It is that  $(q_x q'_y - q_y q'_x)$  of position 1 and position 2 have the same absolute value but opposite signs, and  $(q_x q'_x + q_y q'_y)$  and  $A_{\mathbf{q}, \mathbf{q}'}$  are the same in both absolute value and sign, for position 1 and position 2. Here after we are going to verify these assumptions.

Fig. 5.9 shows a sketch of diffraction pattern in a three-beam condition. A line passing through transmission spot and the two diffraction spot is along the x direction. A line passing through position 1 and 2 is along y direction. x and y components of the transfer vectors  $\mathbf{q}$  and  $\mathbf{q}'$  for position 1 are displayed in this figure. It is easy to imagine that the signs of  $q_y$  and  $q'_y$  for position 1 are opposite to those for position 2. Moreover, the absolute values of  $q_x$ ,  $q'_x$ ,  $q_y$  and  $q'_y$  for both positions are equal to each other. Therefore, we confirm that  $(q_x q'_y - q_y q'_x)$  of position 1 and position 2 have equivalent absolute value but opposite signs.

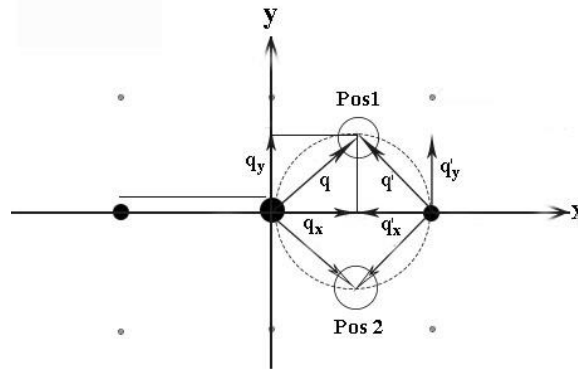


Fig. 5.9. A sketch of diffraction pattern with transfer vectors in two positions.

Another coefficient  $A_{\mathbf{q}, \mathbf{q}'}$ , as defined in Eq. (5.23), is a product of Bloch wave coefficients of the incident and scattered electrons obtained by solving the Schrodinger equation in a lattice periodic static potential within the frame work of the dynamic diffraction theory<sup>22,7</sup>.

$$A_{q,q'} = Y_{ghg'h'}^{j'j'l'} T_{j'j'l'} = C_0^{(j)*} C_g^{(j)} D_0^{(l)} D_h^{(l)*} \times C_0^{(j')} C_g^{(j')*} D_0^{(l')*} D_h^{(l')} T_{j'j'l'}(t) \quad (5.23)$$

At this step, we don't know how to determine the value of  $A_{q,q'}$  precisely. We are going to temporarily consider that the coefficient  $A_{q,q'}$  is the same in position 1 and position 2, and has the same sign for Dy atomic planes and Fe atomic planes.

In our experiment, the Fe-L<sub>2,3</sub> and Dy-M<sub>4,5</sub> edges are obtained in the same sample area and in the same (11 $\bar{3}$ ) three-beam condition. Both the same detector position and aperture size are precisely determined in the post data treatment process. That happens to be one of the most outstanding advantages of ESI recording method for EMCD experiment. Therefore, their values of  $\frac{q_x q_y' - q_y q_x'}{q^2 q'^2}$ ,  $\frac{1}{q^2} A_{q,q'}$  and  $\frac{q_x q_x' + q_y q_y' + q_z^2}{q^2 q'^2}$  must be the same. What makes the  $a/b$  factors in Eq. (5.22) for Fe and Dy signals different is the coefficient  $A_{q,q'}$ . The locations of Fe and Dy atoms are not the same in a DyFe<sub>2</sub> lattice, but it has been mentioned above that the signs of the coefficients  $A_{q,q'}^{det}$  for Fe and Dy are the same. That is to say, the dynamical diffraction effect in the Fe and Dy cases can be excluded as a possible influential factor to change the sign of the dichroic signal, so that the sign difference between Fe and Dy dichroic signals unambiguously indicates antiparallel alignment of net Fe 3d and Dy 4f moments in the investigated area. Now the EMCD technique has been proved to be able to determine the coupling behavior of magnetic moments, parallel or antiparallel. It provides a method to study the exchange coupling in magnetic materials in a high spatial resolution.

#### 4. Conclusion

In conclusion, the work in this chapter explores the application of EMCD technique to both 4f moment and 3d moment by investigating Dy-M<sub>4,5</sub> edge and Fe-L<sub>2,3</sub> edge respectively in DyFe<sub>2</sub>/YFe<sub>2</sub> superlattice. At first, the structure factors of Dy and Fe were separately calculated, providing necessary information to determine a specific three-beam condition. In the EMCD experiment, (11 $\bar{3}$ ) three-beam condition was settled in the TEM to detect signals at both Fe-L<sub>2,3</sub> and Dy-M<sub>4,5</sub> edges. EMCD sum rules specified for M<sub>4,5</sub> edges were derived and their application conditions to Dy-M<sub>4,5</sub> edges was be discussed in

detail. In addition, signs of the Dy-M<sub>5</sub> and Fe-L<sub>3</sub> peak in the dichroism spectra are opposite. The influence of dynamic diffraction effect on Fe-L<sub>3</sub> and Dy-M<sub>5</sub> EMCD signal amplitudes was then precisely analyzed, and it came that the opposite signs of these two peaks is suggesting that the antiparallel alignment of net Fe 3*d* and Dy 4*f* moments. This work evidences that the EMCD technique is an effective tool to probe 4*f* moment and to study magnetic moment coupling in magnetic materials.

## Bibliography

1. Wallace, W. E. Rare Earth-Transition metal permanent magnet materials. *Prog. Solid State Chem.* **16**, 127–162 (1985).
2. Stanciu, C. D. *et al.* All-Optical Magnetic Recording with Circularly Polarized Light. *Phys. Rev. Lett.* **99**, 047601 (2007).
3. Chen, K. *et al.* Temperature-dependent magnetic properties of ferrimagnetic DyCo<sub>3</sub> alloy films. *Phys. Rev. B* **91**, 024409 (2015).
4. Sanyal, B. *et al.* Forcing Ferromagnetic Coupling Between Rare-Earth-Metal and 3d Ferromagnetic Films. *Phys. Rev. Lett.* **104**, 156402 (2010).
5. Mizumaki, M. *et al.* Verification of Ni magnetic moment in GdNi<sub>2</sub> Laves phase by magnetic circular dichroism measurement. *Phys. Rev. B* **67**, 132404 (2003).
6. Schattschneider, P. *et al.* Detection of magnetic circular dichroism using a transmission electron microscope. *Nature* **441**, 486–488 (2006).
7. Calmels, L. *et al.* Experimental application of sum rules for electron energy loss magnetic chiral dichroism. *Phys. Rev. B* **76**, 060409 (2007).
8. Pohl, D., Schneider, S., Ruzs, J. & Rellinghaus, B. Electron vortex beams prepared by a spiral aperture with the goal to measure EMCD on ferromagnetic films via STEM. *Ultramicroscopy* **150**, 16–22 (2015).
9. Schattschneider, P. *et al.* Detection of magnetic circular dichroism on the two-nanometer scale. *Phys. Rev. B* **78**, 104413 (2008).
10. Fu, X. *et al.* Energy-loss magnetic chiral dichroism study of epitaxial MnAs film on GaAs(001). *Appl. Phys. Lett.* **107**, 062402 (2015).
11. Warot-Fonrose, B. *et al.* Mapping inelastic intensities in diffraction patterns of magnetic samples using the energy spectrum imaging technique. *Ultramicroscopy* **108**, 393–398 (2008).
12. Gatel, C., Warot-Fonrose, B. & Schattschneider, P. Distortion corrections of ESI data cubes for magnetic studies. *Ultramicroscopy* **109**, 1465–1471 (2009).
13. Muto, S. *et al.* Quantitative characterization of nanoscale polycrystalline magnets with electron magnetic circular dichroism. *Nat. Commun.* **5**, 1-7 (2014).
14. Wang, Z. Q., Zhong, X. Y., Yu, R., Cheng, Z. Y. & Zhu, J. Quantitative experimental determination of site-specific magnetic structures by transmitted electrons. *Nat. Commun.* **4**, 1395 (2013).

15. Thersleff, T. *et al.* Quantitative analysis of magnetic spin and orbital moments from an oxidized iron (1 1 0) surface using electron magnetic circular dichroism. *Sci. Rep.* **5**, 13012 (2015).
16. Dumesnil, K. *et al.* Temperature and thickness dependence of the magnetization reversal in DyFe<sub>2</sub>/YFe<sub>2</sub> exchange-coupled superlattices. *Eur. Phys. J. B* **72**, 159–171 (2009).
17. Carra, P., Thole, B. T., Altarelli, M. & Wang, X. X-ray circular dichroism and local magnetic fields. *Phys. Rev. Lett.* **70**, 694–697 (1993).
18. Rusz, J., Eriksson, O., Novák, P. & Oppeneer, P. M. Sum rules for electron energy loss near edge spectra. *Phys. Rev. B* **76**, 060408 (2007).
19. Teramura, Y., Tanaka, A. & Jo, T. Effect of Coulomb Interaction on the X-Ray Magnetic Circular Dichroism Spin Sum Rule in 3 d Transition Elements. *J. Phys. Soc. Jpn.* **65**, 1053–1055 (1996).
20. Wikberg, J. M. *et al.* Magnetocrystalline anisotropy and uniaxiality of MnAs/GaAs(100) films. *Phys. Rev. B* **83**, 024417 (2011).
21. Holm, A. P. *et al.* XMCD Characterization of the Ferromagnetic State of Yb<sub>14</sub>MnSb<sub>11</sub>. *J. Am. Chem. Soc.* **124**, 9894–9898 (2002).
22. Schattschneider, P. *Linear and Chiral Dichroism in the Electron Microscope*. (CRC Press, 2012).
23. Rusz, J., Rubino, S. & Schattschneider, P. First-principles theory of chiral dichroism in electron microscopy applied to 3d ferromagnets. *Phys. Rev. B* **75**, 214425 (2007).



## Conclusion

In my thesis, local magnetic properties of epitaxial thin films are examined by TEM techniques. The work performed using EMCD provides answers to the four main questions proposed in the introduction.

(i) Could EMCD be successfully applied to crystals, with an hexagonal structure and high magnetocrystalline anisotropy? The investigation reported in chapter IV illustrates for the first time the feasibility of EMCD technique for quantitative study of magnetocrystalline anisotropy of hexagonal phases. Three TEM specimens of MnAs/GaAs(001) with zone axes along the easy, hard and intermediate magnetic axes are prepared and inspected. By electron diffraction, the hexagonal  $\alpha$ -MnAs and very similar quasi-hexagonal  $\beta$ -MnAs are distinguished along some specific zone axes. EMCD experiments are performed on the three specimens at RT, and dichroic signals are obtained from the identified hexagonal ferromagnetic  $\alpha$ -MnAs. The application of EMCD sum rules to these dichroic signals is discussed. One conclusion at this step is that the application of sum rules requires a preliminary analysis. Then, the EMCD results of orbital-to-spin moment ratio are compared to the XMCD and DFT ones. It is locally demonstrated that the EMCD signal and the measured magnetic moment ratio are anisotropic for the anisotropic magnetic materials. This opens new field applications of this promising technique.

Further experiments could be done to study the sensitivity of EMCD technique for quantitative study of magnetocrystalline anisotropy, by acquiring a series of EMCD signals in the same crystal tilted in different angles. If we can take into account the dynamic effects contribution on those dichroic signals in a post-treatment process, their intensities can be directly compared one to the other, thus it is possible to quantify the relative value of the magnetocrystalline anisotropy.

(ii) Can we take EMCD one step towards a dynamic measurement method? An in-situ study of the MnAs/GaAs(001) in chapter IV gives a positive answer. When modifying the temperature of the specimen inside the electron microscope from RT to 50°C, a breaking of the ferromagnetic order in the MnAs thin film, together with the crystallographic transition from  $\alpha$ -MnAs to  $\beta$ -MnAs, is observed and measured from the



evolution of the EMCD signal. An obvious dichroic signal is detected at RT while it disappears at 50°C. This also enlarges the field of interest of EMCD for *in situ* study of materials containing locally multiple phases. The temperature range covers by *in situ* temperature-dependent EMCD is in practical from He to 1000 ° C, so allowing to explore a huge number of materials dedicated to spintronic.

An additional temperature-dependent experiment performed using electron holography (EH) on a cross-section specimen, associated to bright field experiments (not shown in this manuscript) fully confirm the disappearance of local ferromagnetism at the temperature of 50°C. Surprisingly, the temperature-dependent magnetic configuration acquired by EH provides a new sight into the local magnetic properties. Some interesting phenomena, such as the inhomogeneous phase transition and the creation of magnetic domain vortices in the position of defects, attract our attention. The causes of these phenomena are under exploration.

(iii) The third question concerns the panel of edges which can be reached by EMCD. How far can we go?  $M_{4,5}$  edges of rare earth, the magnetism of which is related to the unbalanced filling of up and down spin in the 4 f levels, have never been studied by EMCD before. In chapter V, EMCD is settled to probe both 4f moment and 3d moment by investigating Dy- $M_{4,5}$  edges, which stands at higher energy, nearly 1300 eV, and Fe- $L_{2,3}$  edges under the same beam condition and in exactly the same area in DyFe<sub>2</sub>/YFe<sub>2</sub> superlattice. Dichroism signal is observed in both Dy- $M_{4,5}$  and Fe- $L_{2,3}$  edges. EMCD sum rules which are specified for  $M_{4,5}$  edges are derived and their application conditions to Dy- $M_{4,5}$  edges are discussed in detail. This work evidences that the EMCD technique is an effective tool to probe 4f moment of a rare earth element. The general formula of EMCD sum rules are also written in Chapter V.

(iv) Last, but not least: the acquisition of EMCD dichroic signal from two different edges and the study of the magnetic coupling. Section 3.3 in chapter V has a discussion on it. This dichroic signals of Dy- $M_{4,5}$  edges and Fe- $L_{2,3}$  edges are obtained in the experimental condition that a magnetic field of 2 T is exerted on the DyFe<sub>2</sub>/YFe<sub>2</sub> superlattice sample. Under such a magnetic field, an exchange spring is formed. In order to have a deeper understanding of the magnetic mechanism in the exchange spring, it is of importance to investigate how the moments of different elements in the superlattice are coupled with each other. It is found that signs of the Dy- $M_5$  and Fe- $L_3$  peak in the EMCD spectra are opposite. The influence of dynamic diffraction effect on Fe- $L_3$  and

Dy- $M_5$  EMCD signal amplitudes is taken into consideration, and it comes that opposite signs of these two peaks are suggesting the antiparallel alignment of net Fe 3d and Dy 4f moments in the DyFe<sub>2</sub>/YFe<sub>2</sub> superlattice. We are also interested in probing the Y 4f moment by EMCD in the later work. EMCD is promising to study the magnetic coupling behavior in magnetic materials.



## **Appendix I. Transmission Electron Microscopy**

### **1. Components of a transmission electron microscope**

A transmission electron microscope (TEM) is a large scientific equipment that can be used to investigate an extremely small area of objects in nanometer scale. A beam of fast electrons travel through and interact with an ultra-thin specimen (the specimen preparation is presented in appendix II). The transmitted electrons pass through electron lenses, which are analog to the glass lenses in a visible light microscope, and finally form an image of a small area in the investigated specimen.

Since the first TEM built in 1931, the TEM have been developed a lot. Fig. 1 demonstrates a schematic of TEM optics, taking a Tecnai TEM as the example<sup>1</sup>. Generally a TEM consists of many components such as a gun, lenses, apertures, screen, detectors, sample stage, etc.

There are different types of emission guns<sup>2</sup>. One is the thermionic gun. The electrons commonly generate from the lanthanum hexaboride (LaB<sub>6</sub>) crystal when the crystal is heated. The other one is the field emission gun, including cold field emission gun and thermal field emission gun. In the cold field emission gun, the electrons are extracted from the fine tungsten needle by a high voltage field. In the thermal field emission one, the needle is under both high voltage field and high temperature. The Tecnai TEM has a thermal field emission gun operating in Schottky mode<sup>1</sup>.

Lenses in TEM are in fact coils around soft-iron cores<sup>2</sup>. When the current passes through the coil, a magnetic field can be generated to change the path of electrons according to Lorenz effect, thus to realize the spread or focus of the electron beam. Apertures in TEM work as selectors to select a portion of electron beam to pass through or select an interesting area of the specimen.

The components of a Tecnai in Fig. 1 can be divided into three parts: the illumination system, the objective lens/stage, and the imaging system<sup>2</sup>. The illumination system takes the electrons from the gun source and transfer them to the specimen. The beam on the specimen can be convergent or parallel using different settings. The objective lens/stage system is where the beam-specimen interaction takes place, and the

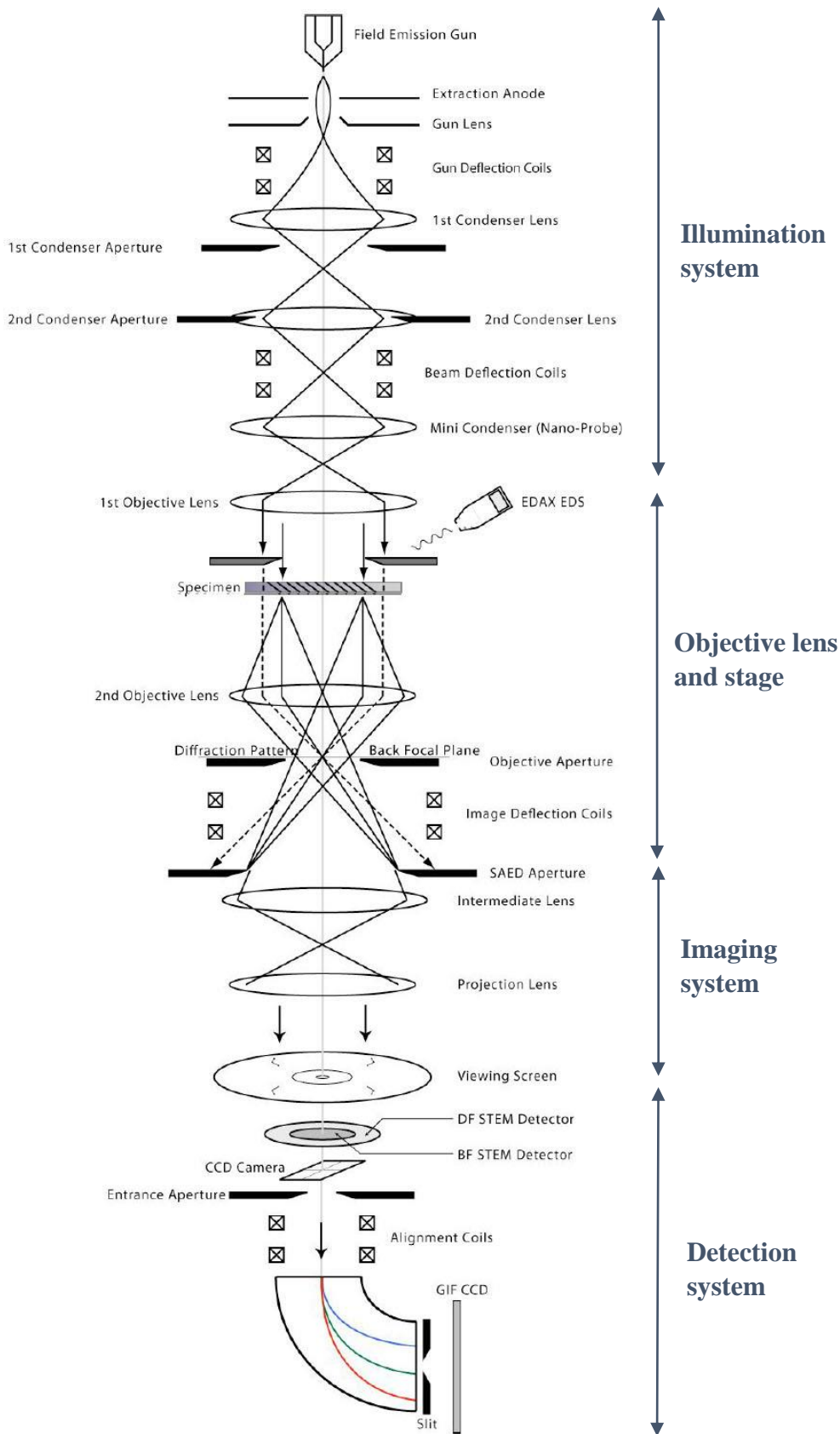


Fig. 1. A schematic of Tecnai optics<sup>1</sup>.

creation of images and diffraction patterns occurs. The imaging system magnifies the images or diffraction patterns produced from objective lens system, and project them on the viewing screen, detector or camera. Based on different settings in the three systems, with the addition of an aberration corrector and some attached detection and analysis system such as an energy-filtered spectrometer, the TEM is a powerful equipment for imaging and analysis of materials in high spatial resolution.

## **2. Forming of diffraction patterns and images**

Various TEM techniques are developed to obtain different information from the materials, e. g. bright-field (BF) and dark-field (DF) imaging, high-angle annular dark-field imaging (HAADF), selected area electron diffraction (SAED), convergent beam electron diffraction (CBED), electron holography (EH), electron energy loss spectroscopy (EELS), energy filtered transmission electron microscopy (EFTEM), electron energy-loss magnetic chiral dichroism (EMCD), etc. Fundamentally, these techniques are based on the formation of diffraction patterns and images<sup>2</sup>.

Seen From Fig. 1, after the electrons emerge from the exit surface of the specimen, they are dispersed by the objective lens to form a diffraction pattern in the back focal plane, and then recombined to form an image in the image plane where the SAED aperture is placed. To see the diffraction pattern or the image on the view screen or the camera, the imaging-system lenses should be set in different conditions. We say that the TEM works in diffraction mode or image mode. In the diffraction mode, the objective plane of the intermediate lens is adjusted to the back focal plane of the objective lens, so that the diffraction pattern can be projected on the screen or the camera. While in the image mode, the objective plane of the intermediate lens is adjusted to the image plane of the objective lens instead. Simplified optics for the diffraction and image modes is shown in section 2.3.1 in chapter I.

As stated above, there are various TEM techniques developed from the diffraction and imaging, and some of them have been applied in this thesis. For example, if an aperture, named SAED aperture, is inserted in the image plane, a virtual aperture will be created in the plane of the specimen to select an area on the specimen as displayed in Fig. 2. Only electrons passing through this selected area will be allowed to enter the imaging system and form a diffraction pattern. This technique is the so-called

selected area electron diffraction (SAED). The SAED pattern only carries the information from a small selected area in the specimen.

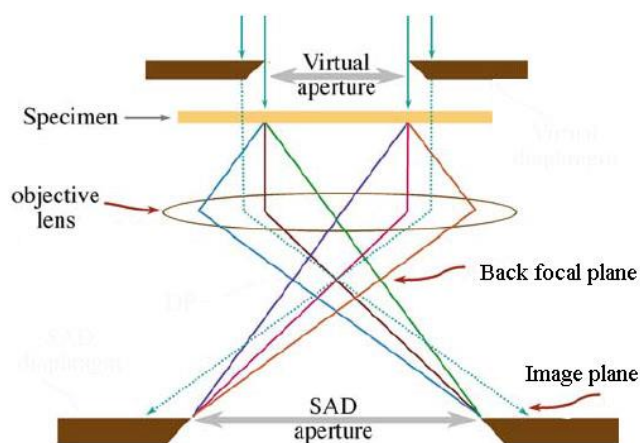
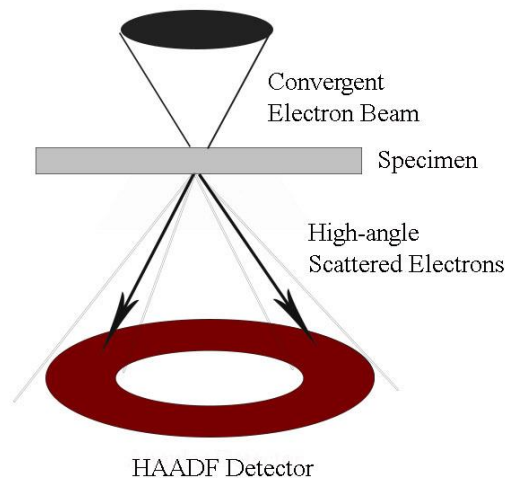


Fig. 2. <sup>2</sup>Optics of the selected area diffraction (SAD) pattern formation: a SAD aperture in the image plane results in a virtual aperture in the plane of the specimen. Only electrons passing through the specimen selected by the virtual aperture will be allowed through into the imaging system to form a SAD pattern.

When the SAED pattern is projected on the screen or the camera, we can use this diffraction pattern to operate two most basic imaging technique: bright-field (BF) and dark field (DF) imaging<sup>2</sup>. A typical diffraction pattern contains a bright direct spot in the center and some diffraction spots around. If an objective aperture is inserted in the back focal plane to only select the direct spot, we can see what we call bright-field (BF) image on the screen or the camera. The contrast in the bright-field image is due to the absorption of electrons to different degrees by different regions in the specimen. In the BF image, thinner regions of the specimen, or regions with a lower atomic number, will appear brighter. The vacuum is of course in the highest brightness. If an objective aperture is inserted in the back focal plane to only select a diffraction spot which corresponds to the diffracted beam from specific atomic planes, a dark-field (DF) image is formed on the screen or the camera. It means that only the diffracted beam forming the selected diffraction spot has contribution to the image, so that only the region which has the specific atomic planes is bright in a DF image. One should notice that a technique named high-angle annular dark-field (HAADF) imaging is different from the traditional DF imaging. It is operated in the scanning TEM mode instead of the conventional TEM

mode. In principle, incident electrons will be scattered to a higher deviation angle by the atoms with higher atomic number  $Z$ . If an annular detector is positioned, as shown in Fig. 3, to detect the electrons which are scattered to a higher deviation angle, the regions with higher atomic number  $Z$  must be brighter. That is why the contrasts of HAADF and BF images are generally inverse.



*Fig. 3. Principle of the HAADF detection.*

In addition, high resolution transmission electron microscopy (HRTEM) is also a conventional imaging technique that allows for direct imaging of the atomic structure of the specimen. HRTEM image is an interference pattern between the forward-scattered and diffracted electron waves from the specimen. This technique demands good performance of the lens in TEM, in particular the objective lens, so an aberration corrector attached to the TEM is of necessity. The magnification value in HRTEM is usually above  $4 \times 10^5$ . A wiener filter can be applied to remove contributions from amorphous phases to HRTEM images.

## **Bibliography**

1. Aaron I. Besser et al. FEI Tecnai F-20 Operations Manual, Portland State University, 2010.
2. David B. Williams, C. Barry Carter, Transmission Electron Microscope, A Textbook for Materials Science, Springer, 2009.



## **Appendix II. TEM Specimen Preparation**

There are many ways to prepare a TEM specimen<sup>1</sup>. The methods we choose depend on what we want to study and what is the characteristics of the material. No matter which method is used, the primary requirement is that the specimen must be ultra-thin such that it allows electrons to travel through and form an interpretable image on the screen or camera. The required thickness is dependent of the electron energy and the specimen itself. Generally the specimen thinner than 100 nm is necessary for 100kV electrons. For some techniques such as high resolution TEM, thickness smaller than 50nm is better.

In general, we divide the TEM specimens into two groups by the ways of handling the thin specimen<sup>1</sup>. They are specimens supported on a Cu grid or washer and self-supporting specimens. The former method is to support the particles or an electron-transparent portion of the material with a thin film (usually carbon film) on a Cu grid or washer. The latter method is to cut a disk of the material and then only thin a small area in the center until it is electron transparent, such that the thicker area around the center can support the specimen by itself. Cross-section specimen and plan-view specimen are two important types of self-support disks. In what follows, we focus on the preparation process of the two types.

The cross-section specimen is usually prepared when we wish to study interfaces. Any samples with double or multiple layers are candidates for this type of preparation. Fig. 1 (a-d) demonstrates its preparation principle. At first, the bulk sample is cut and the two halves are glued together as shown in Fig. 1(a-b), resembling a sandwich. A thin slide, which is around 100  $\mu\text{m}$  to 200  $\mu\text{m}$  thick, is cut from the sandwich and then polished from one side or both sides to a thickness of several micrometers, as seen in Fig. 1(c). We can call this step “pre-thinning”. Usually the polished sandwich is then attached on a Cu grid with a small hole or slot in the center for stabilizing the fragile thin sample. In the final step, the polished sandwich is thinned again until the required thickness is achieved. Ion milling is a commonly used method for the final thinning. Ion milling<sup>2</sup> is a sputtering process in which energetic neutral atoms and ions from a cathode impinge on the specimen center at an angle, and the atoms of the specimen are knocked off, resulting an electron transparent region in the specimen center, as shown in Fig. 1(d). In practice, a

hole will appear in the central thinned area. The ultra-thin area which is to be investigated is just around the hole. In Fig. 1(e), we can see that as a result, the electron beam is parallel to the interface in a TEM, so specimen is suitable to do interface investigation.

The plan-view specimen is prepared with less steps. The process is demonstrated in Fig. 1(f-i). The bulk sample is pre-thinned to a thickness of several micrometers from the substrate side by mechanical polishing or other methods, and then ion milled. Similar to the cross-section specimen, a hole will also appear in the thinned area and the ultra-thin area is around the hole. The electron beam in TEM will only travel through the sample layer without interaction with the substrate.

Precision ion polishing system (PIPS) is an ion milling system. In PIPS, the pre-thinned specimen is loaded in a holder and then milled by energetic ions. Important parameters are gun angles, voltage and rotation speed. For cross-section specimen, one gun angle is positive and the other is negative, which means the specimen is milled from double side, while for plan-view specimen the gun angle is only positive to avoid milling the film layer. Here we give the milling conditions that we applied to MnAs/GaAs(001) sample: (a) gun angles:  $\pm 7^\circ$ , (b) voltage: 5kV initially and 2kV at a lower angle for 5 minutes. (c) holder rotation at 3r.p.m during milling. A real TEM image in Fig. 2 obtained with a plan-view specimen of MnAs/GaAs(001) heterostructure may help understanding the specimen preparation.

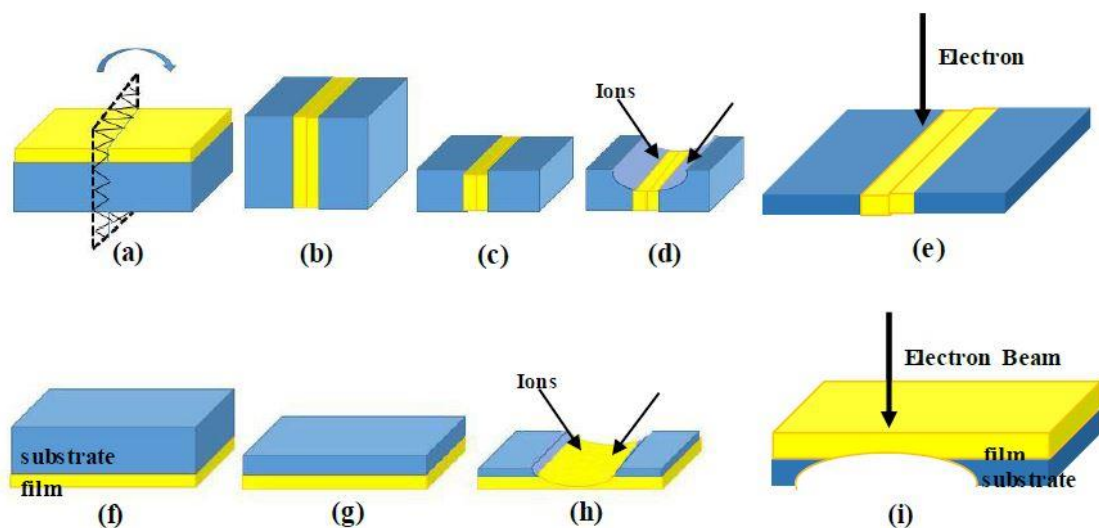


Fig. 1. (a-d) is the preparation principle of cross-section specimen. (a) cut the bulk sample; (b) glue the two halves; (c) pre-thinning; (d) final-thinning. (f-h) is the preparation principle of plan-view specimen. (f) a bulk sample; (g) pre-thinning from the

substrate side; (h) final-thinning. (e) and (f) are the schemes to illustrate the direction of electron beam with respect to the specimen.

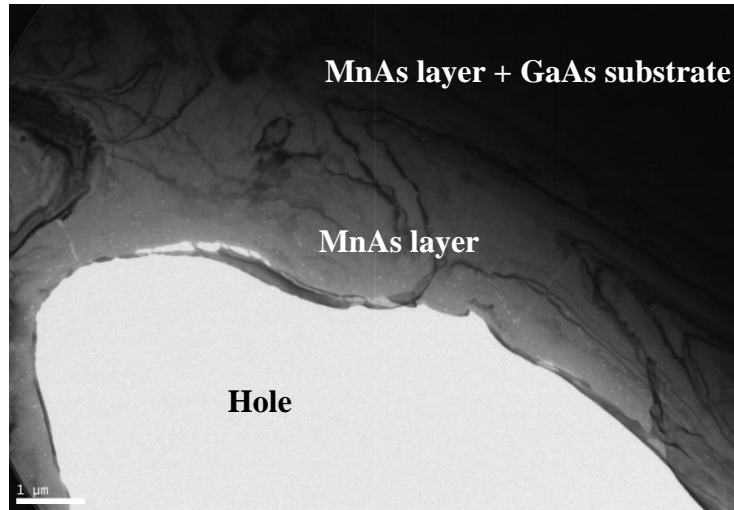


Fig. 2. A TEM image of low magnification obtained with MnAs/GaAs(001) plan-view specimen.

## Bibliography

1. David B. Williams, C. Barry Carter, Transmission Electron Microscope, A Textbook for Materials Science, Springer, 2009.
2. D. V. Sridhara Rao, et al. TEM specimen preparation techniques, Microscopy: Science, Technology, Applications and Education, 2010.

## **Appendix III. Molecular Beam Epitaxy**

There are a lot of thin film synthesis techniques for depositing a thin film of some material onto a surface<sup>1</sup>. The deposition methods fall mainly into two categories, sorted by whether they are based on physical or chemical process. Chemical vapor deposition (CVD) is one of the most important and widely used chemical deposition technologies, while the films are usually deposited at elevated temperatures with CVD, resulting in some restrictions on the substrates. Physical vapor deposition (PVD), the physical deposition technology, is free from the restrictions on both substrate and film material. In general, there are three fundamental steps to develop a thin film with PVD technologies. (1) The generation of particles from the source material of thin film; (2) the transfer of source material particles to the substrate; (3) deposition and film growth on the substrate. Thermal evaporation and sputtering are two commonly used methods to achieve the generation of source material particles. In the thermal evaporation deposition technique, the solid source material is heated until evaporating, and then the material vapor gradually condenses on the substrate surface, building a solid thin film on the substrate. Sputtering uses high-energy particles to knock material atoms from a "target" instead of heating.

Molecular Beam Epitaxy (MBE), a thin film synthesis technique invented in the late 1960s, is essentially a sophisticated form of thermal evaporation deposition technique. The main difference from the traditional thermal evaporation method is that the MBE system requires high vacuum or ultra-high vacuum ( $10^{-8}$  Pa) to keep the growth surface clean, and it allows real-time and in-situ monitoring analysis of the growth surface as well as its environment, making it a superior technique to grow single crystal thin films of high quality, especially semiconductor thin films.

### **1. The principle of MBE**

The name of MBE explains itself to some extent. The term "epitaxy" refers to the deposition of a crystalline film that has a well-defined orientation with respect to the underlying substrate crystal structure. "Molecular beam" means that the source of

constituents is provided as beams of molecules or atoms to the substrate surface. In an ultra-high vacuum (UHV) environment, the source material evaporates by being heated, or with other methods, to form beams of molecules or atoms. The beams of molecules or atoms impinge on the substrate surface, and gradually develop to be a thin film through a series process, e. g. surface absorption, atoms migration, nucleation and growth<sup>2</sup>. In the process, important parameters such as the growth rate, film thickness and substrate temperature are monitored in situ by reflection high-energy electron diffraction (RHEED) technique and the surface morphology can also be analyzed in real time by scanning tunneling microscopy (STM) technique. Under such precise control, a uniform epitaxial layer with little defect is achievable.

Before the deposition of epi-layer, the reconstruction of substrate surface should not be neglected, as the surface structure plays an important role in the growth of epitaxial layer<sup>3</sup>. The substrate surface is initially contaminated by oxygen, hydrogen or carbon and it will reconstruct after it is cleaned by heating process. It is because the atoms on the clean surface are usually not ordered as they are in the bulk, but reconstructed in another pattern. In Fig. 1, the reconstructed Si(001)2×1 surface is given as an example to compare with the ideal non-reconstructed Si (001) surface<sup>4</sup>. Thanks to the RHEED and STM technique, the substrate surface reconstruction can actually be monitored and it can even be controlled by setting different experimental conditions. In addition, a buffer layer is usually grown on the substrate surface to achieve a smoothed reconstructed surface.

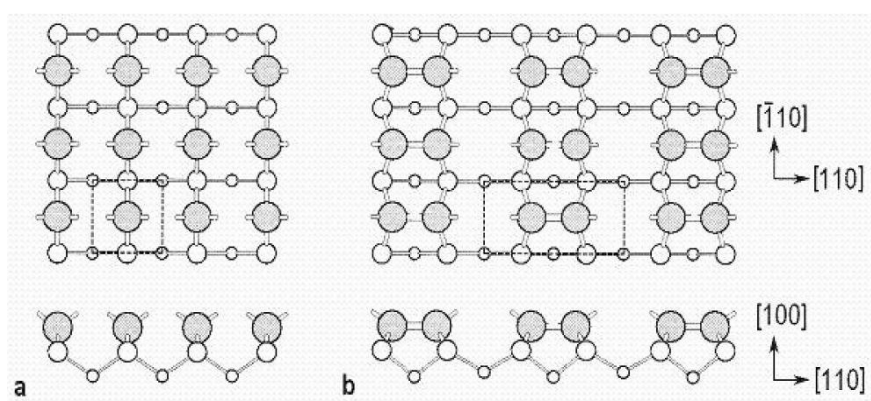


Fig. 1. (a) Ideal non-reconstructed Si(001)1x1 surface. (b) Reconstructed Si(001)2x1 surface.<sup>4</sup>

In the next step, the atoms arriving at the substrate surface can behave in different ways to form a thin film, depending on different growth temperatures or different kinds of atoms and substrate involved. For heteroepitaxy, which means the lattice of the epitaxial layer and substrate is mismatched, there are basically three growth modes, which are Franck-van der Merve (FV), Volmer-Weber (VW) and Stranski-Krastanov (SK)<sup>4</sup>. Fig. 2 gives the schematic of the three modes. In VW, the atoms tend to build as isolated islands, so it has another name of island growth. The epilayer grown in this mode usually has big lattice mismatch with the substrate, thus is easier for the incident atoms to attach to each other than to the substrate surface. In FV mode, also called layer-by-layer growth, the atoms tend to spread over the substrate surface to form one flat atomic layer after another, when the mismatch is very small. The SK mode consists of both the FV and VW process, owing it a name of layer-plus-island mode. A layer is formed at first in layer-by-layer mode until a certain thickness, and then the isolated islands grow. This mode is followed when there is a moderate lattice mismatch. For homoepitaxy, which means the epilayer has the same lattice with the substrate, there are also three growth modes. They are step-flow, multi-layer and the layer-by-layer mode. The whole growth process is monitored and analyzed by RHEED and STM.

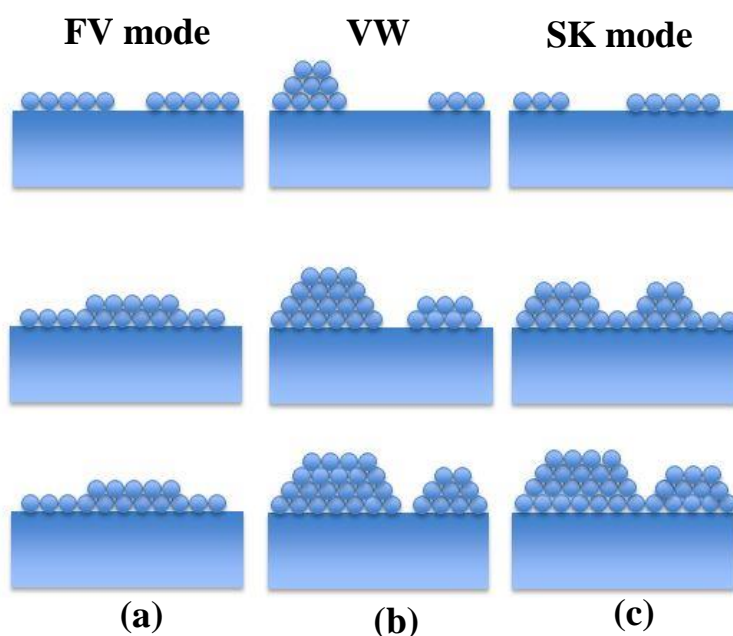


Fig. 2. Schematic of three growth modes. (a) Frank-van der Merve mode, (b) Volmer-Weber mode, (c) Stranski-Krastanov mode. The square represents substrate and the circles represent incident atoms.

## **2. MBE equipment**

A typical commercial MBE system generally consists of several chambers, e. g. vacuum chambers, growth chamber, analysis chamber, etc.<sup>2</sup> The growth chamber, the most essential part in the MBE system, is the space where the thin film is deposited. Fig. 3 is a schematic front view of a basic MBE growth chamber. The substrate is sent into the growth chamber with the transfer rod and attached on the heated substrate holder. The substrate is positioned to face the effusion cells. The evaporated beams of atoms and molecules are emitted from the effusion cells and impinge on the substrate. From different cells come the different kinds of constituent atoms. The mechanical shutters can be controlled to switch the beams on and off. The RHEED system is an important in-situ real-time tool to monitor the surface quality during film growth. High-energy electrons are emitted from the RHEED gun and accelerated towards the substrate at a glancing angle, then the electrons are reflected from the surface to form a diffraction pattern on the RHEED screen on the opposite side of the chamber from the RHEED gun. The pattern will be recorded by a charge-coupled device (CCD) camera and analyzed in the post process. From the changes in the pattern, including the shape and intensity, some surface information such as growth rate, surface morphology can be known, thus the growth process is under observation and control. Fig. 4 gives some examples of RHEED diffraction patterns. The pattern with strike shape of spots is from real smooth surface as shown in Fig. 4(b). If the surface is rough, the pattern is spottier due to transmission through the particles on the surface. The spot intensity is generally dependent of growth rate and deposition coverage. Another example is that the substrate surface reconstruction can be detected using RHEED in real time, so the surface reconstruction can be controlled by adjusting the growth condition.

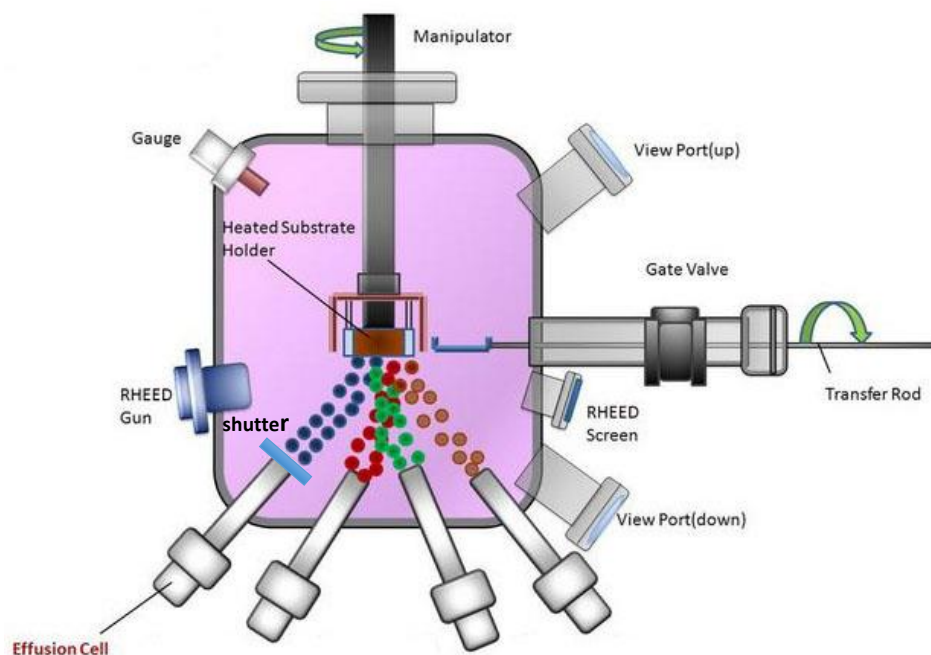


Fig. 3. Schematic front view of a basic MBE growth chamber.

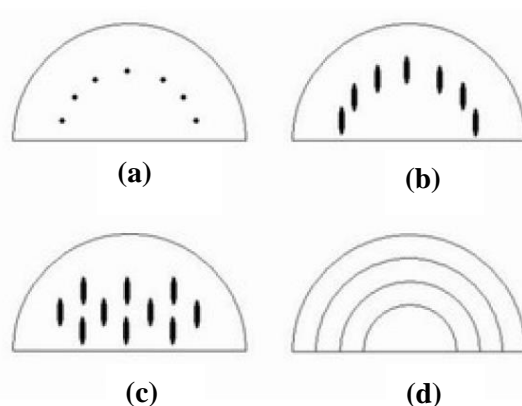


Fig. 4. RHEED Diffraction patterns. In (a) ideal smooth surface, (b) real smooth surface, (c) transmission diffraction through 3D structure (d) randomly oriented crystal sections.

## Bibliography

1. D. M. Mattox, The foundations of vacuum coating technology, William Andrew Publishing, 2003.
2. John R. Arthur, Molecular beam epitaxy, Surface science 500, 189-217, 2001.
3. H. J. Gossmann et al., Initial stages of silicon molecular beam epitaxy: effect of surface reconstruction, Physical Review B 32, 6-11, 1985.
4. Leif Ericsson, Silicon/Germanium molecular beam epitaxy, Karlstads University, 2006.



## Appendix IV. Density Functional Theory

The density functional theory (DFT) was firstly introduced in the 60's<sup>1,2</sup>. It is a popular computational quantum mechanical modeling method to investigate the electronic structure of matters, ranging from atoms, molecules and solids to nuclei and quantum and classical fluids.

The classical theory to calculate electronic structure is based on the wave functions for multi-electron atoms, while the DFT uses the density of electrons as the base quantity. According to the Hohenberg-Kohn theorems (H-K)<sup>1</sup>, the ground state properties of a many-electron system can be uniquely determined by the electron density of the fundamental state, and fortunately the electron density depends on only 3 spatial coordinates using functionals of the electron density. Compared to the multi-electron wave function with  $3N$  ( $N$  is the number of electrons) spatial coordinates, this method using the electron density is a great simplification of the problem. The DFT is commonly used within the framework of Kohn-Sham DFT<sup>2</sup>. In Kohn-Sham DFT, electrons do not interact with each other and move in an effective potential which includes the external potential due to the atom nuclei, the Coulomb interaction between pairs of electrons (called Hartree term), and a last contribution to take into account of the electronic exchange and correlations. All the complexity of this method lies in this last term which is unknown: Some approximation has to be used to model the exchange and correlation interactions, and the most commonly used are the local (spin) density approximation (L(S)DA) and the generalized gradient approximation (GGA). For the LDA, the exchange-correlation functional is defined as a function of the (spin) electron density, while for the GGA, the gradient of this density is also used.

Theoretical DFT calculations in chapter IV of this thesis were performed with the full-potential linearized augmented plane waves (FP LAPW) code Wien2k<sup>3</sup> by our collaborator Rémi Arras. We used the generalized gradient approximation (GGA) for the exchange-correlation functional, with the formulation proposed by Perdew, Burke and Ernzerhof<sup>4</sup>. The atomic sphere radii were chosen to 2.0 atomic units for both Mn and As and we made the calculations with the following experimental parameters  $a=3.7253\text{\AA}$ ,

$c=5.7031\text{\AA}$ . The irreducible part of the first Brillouin zone was sampled with 1464 k-points and the convergence parameter RKmax was set to 7.0.

We calculated the properties of MnAs by considering it ferromagnetically ordered (we considered that the magnetization was always saturated by the applied magnetic field, in the experiment), and the direction of the magnetization was fixed by adding the spin-orbit interaction.

## Bibliography

1. Hohenberg, P. & Kohn, W. Inhomogeneous Electron Gas. *Phys. Rev.* **136**, B864–B871 (1964).
2. Kohn, W. & Sham, L. J. Self-Consistent Equations Including Exchange and Correlation Effects. *Phys. Rev.* **140**, A1133–A1138 (1965).
3. P. Blaha, K. Schwarz, G. K. H. Madsen, D. Kvasnicka, & J. Luitz, WIEN2K, Vienna University of Technology, Vienna, 2001.
4. Perdew, J. P., Burke, K. & Ernzerhof, M. Generalized Gradient Approximation Made Simple. *Phys. Rev. Lett.* **77**, 3865–3868 (1996).

## **List of Publications**

1. X.Fu, B. Warot-Fonrose, R. Arras, D. Demaille, M. Eddrief, V. Etgens and V. Serin. Energy-loss magnetic chiral dichroism study of epitaxial MnAs film on GaAs(001), Appl. Phys. Lett. 107, 062402 (2015).
2. X.Fu, B. Warot-Fonrose, R. Arras, G. Seine, D. Demaille, M. Eddrief, V. Etgens and V. Serin. In-situ observation of ferromagnetic order breaking in MnAs/GaAs(001), and magnetocrystalline anisotropy of  $\alpha$ -MnAs by energy-loss magnetic chiral dichroism technique. Phys. Rev. B. 93, 104410 (2016).
3. X.Fu, B. Warot-Fonrose, K. Dumesnil, R. Arras and V. Serin. Magnetic coupling of 4f and 3d moments by EMCD: application to DyFe<sub>2</sub>-based superlattices. (In preparation)
4. X.Fu, B. Warot-Fonrose, V. Serin and C. Gatel. Investigation in inhomogeneous phase transition in epitaxial MnAs thin layers on GaAs substrate by electron holography. (In preparation)

## Curriculum Vitae

### Xiaoxiao Fu

Address :CEMES-CNRS, 29 rue Jeanne Marvig  
BP 94347, 31055 Toulouse, France  
Birth Date: September 22<sup>th</sup>,1988  
Cell Phone: (+33)781698583  
Email: [xiaoxiao.fu@cemes.fr](mailto:xiaoxiao.fu@cemes.fr)

---

### Education

- 2013.9 – now** Ph. D candidate, Nanomaterial Group, CEMES-CNRS and Toulouse University, France. Supervisors: Bénédicte Warot-Fonrose and Virginie Serin.
- 2011.9 – 2013.6** Ph. D candidate of Successive Postgraduate and Doctoral Programs, Instrument Science and Technology, College of Optoelectronic Engineering, Chongqing University, China.
- 2007.9 – 2011.6** Bachelor of Engineering, Optoelectronics and Information Engineering, College of Optoelectronic Engineering, Chongqing University, China.

---

### Characterization Skills



Energy-loss Magnetic Chiral Dichroism (EMCD), EELS, EFTEM, ED,



STEM-HAADF



AFM/MFM, XRD, Holography

---

### Academic Activities

- 2016.6** One-month stay to Department of Materials Science and Metallurgy at the University of Cambridge, in the group of Paul Midgley.
- 2015.6** Oral presentation “In-situ TEM study of temperature-dependent magnetic chiral dichroism: application to epitaxial MnAs/GaAs(001)” in the 20th international conference on magnetism (ICM2015) held in Barcelona of Spain.
- 2014.9** Oral presentation “probing the temperature dependent magnetism in electron microscopy” for “Présente ta thèse en 3 minutes” in Next days 2014 held in Luchon of France.
- 2014.6** Poster presentation “EMCD, review of methods and applications” in “Journées de l'EELS” conference (JEELS2014) held in Roscoff of France.

- 2014.7** Summer school “Advanced Topic in Aberration-Corrected STEM” (superSTEM 2014) held at the SuperSTEM Laboratory in Daresbury UK.
- 2012.8** China (International) Sensor Innovation Competition, with the second prize.
- 2011.5** Defence of 3th China National University students innovative experiment project.

---

### Scholarship and Awards

- 2016.3** Awarded a scholarship for one-month stay in the group of Paul Midgley in Cambridge University from the Lab of Excellence (NEXT).
- 2014.4** Awarded a scholarship to superSTEM summer school funded by the ESTEEM2 project.
- 2013.5** Awarded a scholarship to pursue the Ph.D study in France, selected through a rigid academic evaluation process organized by China Scholarship Council.
- 2012.7** Second prize in 2012 China (International) Sensor Innovation Competition;
- 2011** Awarded a first-class national scholarship for excellent undergraduate student by Chinese Ministry of Education.

---

### Language Skills

- Chinese** Native language
- English** Fluent. TOFEL 105/120
- French** Daily communication. Level A2.

## Abstract

EMCD (Energy-Loss Magnetic Chiral Dichroism) is an emerging technique based on energy-loss spectroscopy (EELS) in a transmission electron microscopy (TEM). It aims at measuring the element-specific local magnetic moment of solids at a nanometer scale, and hence improving our understanding of magnetic local magnetic phenomena. This thesis presents the exploring work on developing the EMCD technique and its applications.

We have applied EMCD to epitaxial MnAs thin films grown on a GaAs(001) substrate, extending the application of this technique to hexagonal structure with high magnetocrystalline anisotropy. The 3d orbital-to-spin moment ratio of Mn in hexagonal ferromagnetic MnAs along easy, hard and intermediate magnetic axes has been respectively estimated and then compared to DFT calculations. Moreover, a breaking of the ferromagnetic order in MnAs thin film, together with the crystallographic transition from hexagonal  $\alpha$ -MnAs to quasi-hexagonal  $\beta$ -MnAs, has been locally studied *in-situ* by modifying the temperature of the crystal inside the electron microscope.

EMCD has also been settled to probe 4f moment in rare earth compounds, by investigating Dy- $M_{4,5}$  edges in DyFe<sub>2</sub>/YFe<sub>2</sub> superlattices. We have derived sum rules which are specified for 4f moment and applied them to the obtained dichroic signal over Dy- $M_{4,5}$  edges. In addition, antiparallel coupling of Dy and Fe moments has been confirmed by comparing their dichroic signals, taking into account the dynamic diffraction effect.

The work in this thesis illustrates for the first time the feasibility of EMCD technique for quantitative study of magnetocrystalline anisotropy and magnetic transition, and also proves its potential as a tool to investigate 4f moment as well as moment coupling in magnetic materials.

## Résumé

L'EMCD, Energy Loss Magnetic Chiral Dichroism, est une technique récente, mise en œuvre dans le microscope électronique à transmission (TEM), qui utilise la spectroscopie de pertes d'énergie d'électrons (EELS). Elle a pour objectif la mesure du moment magnétique local d'un élément chimique donné. Son utilisation contribue à progresser dans la compréhension des phénomènes magnétiques à l'échelle nanométrique. Cette thèse propose d'élargir les domaines d'applications de l'EMCD.

Nous avons exploité l'EMCD pour l'étude de films minces de MnAs épitaxiés sur un substrat de GaAs(001). Ce travail montre l'utilité de cette technique dans le cas de structures hexagonales présentant une anisotropie magnéto-cristalline élevée. Le rapport des moments orbital et de spin du Mn dans les films de MnAs ferromagnétique de structure hexagonale a été mesuré par EMCD et comparé à des calculs DFT, ceci le long des axes magnétiques facile, difficile et intermédiaire. Une rupture de l'ordre ferromagnétique a par ailleurs été observée et mesurée *in situ* dans le microscope grâce à un porte-objet chauffant, lors de la transition cristallographique de  $\alpha$ -MnAs hexagonal à  $\beta$ -MnAs quasi-hexagonal.

La technique EMCD a également été mise en œuvre pour sonder le moment 4f de composés de terres rares à base de dysprosium. Il s'agissait d'étudier des super-réseaux DyFe<sub>2</sub>/YFe<sub>2</sub>. Les règles de somme ont été établies pour le seuil  $M_{4,5}$  du Dy. En outre, le couplage antiparallèle des moments Dy et Fe a été confirmé en comparant leurs signaux dichroïques et en prenant en compte la théorie dynamique de la diffraction.

Ce travail de thèse illustre pour la première fois d'une part la faisabilité de la technique EMCD pour l'étude quantitative de l'anisotropie et des transitions magnétiques, et d'autre part son potentiel pour étudier les terres rares et leur moment 4f, ainsi que le couplage avec des éléments de transition.